

UNIVERSITY OF CALIFORNIA
SANTA CRUZ

**SEARCH FOR WW AND WZ RESONANCES IN $\ell\nu qq$ FINAL
STATES IN pp COLLISIONS AT $\sqrt{s} = 13$ TEV WITH THE ATLAS
DETECTOR**

A dissertation submitted in partial satisfaction of the
requirements for the degree of

DOCTOR OF PHILOSOPHY

in

PHYSICS

by

Natasha Woods

December 2019

The Dissertation of Natasha Woods
is approved:

Abraham Seiden, Chair

Mike Hance

Bruce Schumm

Quentin Williams
Vice Provost and Dean of Graduate Studies

Copyright © by

Natasha Woods

2019

Table of Contents

List of Figures	vi
List of Tables	xvi
Abstract	xviii
Dedication	xix
Acknowledgments	xx
I Introduction	1
1 Introduction	2
II Theoretical Motivation	6
2 The Standard Model of Particle Physics	7
2.1 Introduction	7
2.2 Quantum Field Theory	7
2.3 $U(1)_{EM}$ Local Gauge Invariance	8
2.4 Yang-Mills Gauge Theories	11
2.5 Particles in the Standard Model	12
2.6 Higgs Mechanism	17
2.7 Electroweak Theory	18
2.8 Quantum ChromoDynamics	19
3 Standard Model Successes and Limitations	24
4 New Physics Models with Diboson Resonances	27
4.1 Randall Sundrum Bulk Model	27
4.2 Simple Standard Model Extensions	29

III Experimental Setup	31
5 LHC	32
5.1 LHC Layout and Design	34
6 The ATLAS Detector	39
6.1 Coordinate System	41
6.2 Inner Detector	42
6.2.1 Pixel Detector	45
6.2.2 Semiconductor Tracker	45
6.2.3 Transition Radiation Tracker	45
6.3 Calorimeters	47
6.4 Muon Spectrometer	51
6.5 Magnet System	55
6.6 Trigger System	56
IV Method	58
7 Dataset and Simulated Samples	59
7.1 Dataset	59
7.2 Simulated Samples	62
8 Objects	63
8.1 Electrons	63
8.2 Muons	64
8.3 Jets	65
8.3.1 Small-R jets	68
8.3.2 Large-R jets	68
8.3.3 Variable Radius jets	71
8.3.4 Jet Flavor Tagging	72
8.4 MET/Neutrinos	72
8.5 Overlap Removal	72
9 Event Selection and Categorization	74
9.1 Pre-selection	74
9.2 Trigger	74
9.3 non-VBF/VBF RNN	76
9.4 Signal Region Definitions	83
9.5 Selection Acceptance times efficiency for Signal Events	93
9.6 Background Estimate	94
9.6.1 Control Regions	94
9.6.2 Fake Lepton Backgrounds	95

10 Systematic Uncertainties	109
10.1 Experimental Systematics	109
10.2 Theory Systematics	111
11 Statistical Analysis	119
11.1 Likelihood Function Definition	119
11.2 Fit Configuration	120
11.3 Best Fit μ	122
11.4 Discovery Test	123
11.5 Exclusion Limits	124
V Results	126
12 Statistical Interpretation	127
12.1 Discovery Tests	127
12.2 Systematic Profiling and Correlations	133
12.3 Expected and Measured Yields	134
12.4 Limits	148
VI Quark and Gluon Tagging	150
13 Prospects	151
14 n_{trk} Calibration	158
15 Application	164
VII Conclusion	169
16 Conclusions	170
Bibliography	171

List of Figures

2.1	The particles of the Standard Model.	14
2.2	Summary of how Standard Model particles interact with other Standard Model particles.	15
2.3	This figure shows the three dominant QCD interactions. From Ref. [17]	21
2.4	Strength of the U(1), SU(2), and SU(3) gauge couplings as a function of the energy scale of the interaction (Q). From Ref. [11]	22
3.1	A comparison of cross section measurements at $\sqrt{s} = 7, 8, 13$ TeV from ATLAS compared to theoretical measurements. From Ref. [5]	26
4.1	Cartoon of RS Bulk Model	28
5.1	Scaling of cross sections with \sqrt{s} . Natasha: write more here	33
5.2	LHC Layout. Natasha write more	35
5.3	LHC Accelerator. Natasha write more	37
6.1	Big picture layout of ATLAS detector. Natasha: write more	40
6.2	Big picture layout of ATLAS detector. Natasha: write more	40
6.3	A simplified schematic of how different particles interact and are detected within ATLAS.	41
6.4	Layout of ATLAS Inner Detector	43
6.5	Layout of ATLAS ID Barrel System.	44
6.6	Overview of ATLAS electromagnetic and hadronic calorimeters.	48

6.7	Schematic of ECAL	49
6.8	Schematic of HCAL	50
6.9	Schematic of Muon Spectrometer [cite G35]	53
6.10	Schematic of MDT chamber. [cite G35]	54
6.11	Schematic of RPC chamber, which is used for triggering in the central region of the detector [cite G35].	54
6.12	Schematic of TGC chamber, which is used for triggering in the muon end-cap region. [cite G35]	55
6.13	Layout of ATLAS magnet systems.	56
7.1	Integrated luminosity for data collected from ATLAS from 2011 - 2018	60
7.2	Mean number of interactions per crossing for data collected from ATLAS from 2011 - 2018	61
8.1	This figure shows the breakdown of the muon reconstruction efficiency scale factor measured in $Z \rightarrow \mu\mu$ as a function of p_T [4].	65
8.2	[7] This diagram shows the calibration stages for EM jets.	67
8.3	The upper cut on D_2 (a) and jet mass window cut i.e. the upper and lower boundary of the mass (b) of the W -tagger as a function of jet p_T . Corresponding values for Z -tagger are shown in (c) and (d). The optimal cut values for maximum significance are shown as solid markers and the fitted function as solid lines. Working points from $VV \rightarrow JJ$ [ATLAS-HDBS-2018-31-002] is also shown as dashed lines as a reference. Natasha reword?	70
8.4	Natasha write caption	71
9.1	RNN architecture. Natasha add caption	78
9.2	This figure shows the embedded logic in LSTM cells. This image was taken from [22], where a more in depth discussion about LSTMs may be found.	79

9.3	RNN Score distribution for ggF and VBF signals and backgrounds.	80
9.4	ROC curve using k-fold validation for RNN.	81
9.5	Comparison of GGF Z' limits for different RNN score selections. The bottom panel shows the ratio of the upper limits set for different RNN cuts to the cut-based analysis. In this panel smaller numbers, indicate that the expected upper limit is smaller than the cut-based analysis, which is desired.	82
9.6	Event Categorization. Natasha write more.	85
9.7	Data MC comparison for the merged WW HP TCR. The bottom panel shows the ratio of the difference between data and simulation to simulation. The red bands include the all systematic and statistical uncertainties on the background.	87
9.8	Data MC comparison for the merged WW LP TCR. The bottom panel shows the ratio of the difference between data and simulation to simulation. The red bands include the all systematic and statistical uncertainties on the background.	88
9.9	Data MC comparison for the merged WZ HP TCR. The bottom panel shows the ratio of the difference between data and simulation to simulation. The red bands include the all systematic and statistical uncertainties on the background.	89
9.10	Data MC comparison for the merged WZ LP TCR. The bottom panel shows the ratio of the difference between data and simulation to simulation. The red bands include the all systematic and statistical uncertainties on the background.	90
9.11	Data MC comparison for the resolved WW TCR. The bottom panel shows the ratio of the difference between data and simulation to simulation. The red bands include the all systematic and statistical uncertainties on the background.	91

9.12 Data MC comparison for the resolved WZ TCR. The bottom panel shows the ratio of the difference between data and simulation to simulation. The red bands include the all systematic and statistical uncertainties on the background.	92
9.13 Selection acceptance times efficiency for the $W' \rightarrow WZ \rightarrow \ell\nu qq$ events from MC simulations as a function of the W' mass for (a) Drell-Yan and (b) VBF production, combining the merged HP and LP signal regions of the $WW \rightarrow \ell\nu J$ selection and the resolved regions of the $WW \rightarrow \ell\nu jj$ selection.	93
9.14 Selection acceptance times efficiency for the $G \rightarrow WW \rightarrow \ell\nu qq$ events from MC simulations as a function of the G mass for (a) Drell-Yan and (b) VBF production, combining the merged HP and LP signal regions of the $WW \rightarrow \ell\nu J$ selection and the resolved regions of the $WW \rightarrow \ell\nu jj$ selection.	94
9.15 The E_T^{miss} distribution in MJCR for 2017 data in the electron channel(left), muon channel with W-boson pT < 150 GeV (center) and > 150 GeV (right). Multi-jet templates are calculated as remaining data components after excluding known MC	97
9.16 Postfit Data/MC comparison of distributions of E_T^{miss} , m_T^W , lepton and neutrino p_T , $m_{\ell\nu jj}$, lepton- ν angular distance in the WW electron channel. The MJ template is obtained from the pre-MJ-fit.	98
9.17 Postfit Data/MC comparison of distributions of E_T^{miss} , m_T^W , lepton and neutrino p_T , $m_{\ell\nu jj}$, lepton- ν angular distance in the WW muon channel. The MJ template is obtained from the pre-MJ-fit.	99
9.18 Postfit Data/MC comparison of distributions of E_T^{miss} , m_T^W , lepton and neutrino p_T , $m_{\ell\nu jj}$, lepton- ν angular distance in the WZ untag electron channel. The MJ template is obtained from the pre-MJ-fit.	100
9.19 Postfit Data/MC comparison of distributions of E_T^{miss} , m_T^W , lepton and neutrino p_T , $m_{\ell\nu jj}$, lepton- ν angular distance in the WZ untag muon channel. The MJ template is obtained from the pre-MJ-fit.	101

9.20 Postfit Data/MC comparison of distributions of E_T^{miss} , m_T^W , lepton and neutrino p_T , $m_{\ell\nu jj}$, lepton- ν angular distance in the WZ untag electron channel. The MJ template is obtained from the pre-MJ-fit.	102
9.21 Postfit Data/MC comparison of distributions of E_T^{miss} , m_T^W , lepton and neutrino p_T , $m_{\ell\nu jj}$, lepton- ν angular distance in the WZ untag muon channel. The MJ template is obtained from the pre-MJ-fit.	103
9.22 Postfit Data/MC comparison of distributions of E_T^{miss} , m_T^W , lepton and neutrino p_T , $m_{\ell\nu jj}$, lepton- ν angular distance in the VBF WW electron channel. The MJ template is obtained from the pre-MJ-fit.	104
9.23 Postfit Data/MC comparison of distributions of E_T^{miss} , m_T^W , lepton and neutrino p_T , $m_{\ell\nu jj}$, lepton- ν angular distance in the VBF WW muon channel. The MJ template is obtained from the pre-MJ-fit.	105
9.24 Postfit Data/MC comparison of distributions of E_T^{miss} , m_T^W , lepton and neutrino p_T , $m_{\ell\nu jj}$, lepton- ν angular distance in the VBF WZ electron channel. The MJ template is obtained from the pre-MJ-fit.	106
9.25 Postfit Data/MC comparison of distributions of E_T^{miss} , m_T^W , lepton and neutrino p_T , $m_{\ell\nu jj}$, lepton- ν angular distance in the VBF WZ muon channel. The MJ template is obtained from the pre-MJ-fit.	107
 10.1 The $W/Z+jet$ systematics for the a) Merged ggF, b) Resolved ggF, c) Merged VBF, and d) Resolved VBF regions. The top subplot shows the nominal and variation distributions/bands, the middle shows the ratio of the two, and the final shows just the shape of the envelope (the final uncertainty).	113
10.2 The two-point generator comparison between Sherpa and MadGraph for the $W/Z+jet$ samples in the a) Merged ggF, b) Resolved ggF, c) Merged VBF, and d) Resolved VBF regions. The normalization of the Madgraph sample is set to the Sherpa value to consider only shape effects. The bottom inlet shows the ratio of the two.	114

10.3	Ratio between the variations of generator (red) and hadronization (blue) variations for the Merged regime for $t\bar{t}$ sample.	115
10.4	Ratio between the variations of generator (red) and hadronization (blue) variations for the Resolved regime for $t\bar{t}$ sample.	115
10.5	Ratio between the variations of ISR up (red) and down (blue) variations for the Merged regime for $t\bar{t}$ sample.	116
10.6	Ratio between the variations of ISR up (red) and down (blue) variations for the Resolved regime for $t\bar{t}$ sample.	117
10.7	Ratio between the variations of FSR up (red) and down (blue) variations for the Merged regime for $t\bar{t}$ sample.	118
10.8	Ratio between the variations of FSR up (red) and down (blue) variations for the Resolved regime for $t\bar{t}$ sample.	118
11.1	The HVT signal mass resolution as a function of mass fit with a straight line in the Resolved ggF region (left) and VBF (right) region.	122
11.2	The HVT signal mass resolution as a function of mass fit with a straight line in the Merged ggF region (left) and VBF (right) region.	122
12.1	These plots show the measured p_0 value as a function of resonance mass for HVT Z' DY production.	128
12.2	These plots show the measured p_0 value as a function of resonance mass for HVT Z' VBF production.	129
12.3	These plots show the measured p_0 value as a function of resonance mass for HVT W' DY production.	130
12.4	These plots show the measured p_0 value as a function of resonance mass for HVT W' VBF production.	131
12.5	These plots show the measured p_0 value as a function of resonance mass for the RS Graviton DY production.	132
12.6	Ranked systematics and their fitted values for WW DY (right) and VBF (left) selections.	133

12.7	Ranked systematics and their fitted values for WZ DY (right) and VBF (left) selections.	134
12.8	Correlations between systematics for WW DY (right) and VBF (left) selections.	134
12.9	This figure shows the distribution of $m_{\ell\nu qq}$ in the DY WW control regions.	142
12.10	This figure shows the distribution of $m_{\ell\nu qq}$ in the DY WZ control regions.	143
12.11	This figure shows the distribution of $m_{\ell\nu qq}$ in the VBF WW control regions.	144
12.12	This figure shows the distribution of $m_{\ell\nu qq}$ in the VBF WZ control regions.	145
12.13	This figure shows the distribution of $m_{\ell\nu qq}$ in the GGF WW signal regions.	146
12.14	This figure shows the distribution of $m_{\ell\nu qq}$ in the GGF WZ Untag signal regions.	146
12.15	This figure shows the distribution of $m_{\ell\nu qq}$ in the GGF WZ Tag signal regions.	147
12.16	This figure shows the distribution of $m_{\ell\nu qq}$ in the VBF WZ Tag signal regions.	147
12.17	This figure shows the distribution of $m_{\ell\nu qq}$ in the VBF WZ Tag signal regions.	148
12.18	This figure shows theory, expected and observed limits for HVT W' DY (left) and VBF (right) production.	148
12.19	This figure shows theory, expected and observed limits for HVT Z' DY (left) and VBF (right) production.	149
12.20	This figure shows theory, expected and observed limits for RS Gravitons via DY production.	149

13.1	PDGID of the truth-level parton matched to the small-R jets passing the Resolved GGF WW Signal Region selections for the (a) Leading (b) Sub-Leading jets . These distributions are shown for 300, 500, and 700GeV Z' signals and the background.	153
13.2	The number of tracks in small-R jets in events passing the Resolved GGF WW Signal Region selections for the (a) Leading (b) Sub-Leading jets. These distributions are shown for 300, 500, and 700GeV Z' signals and the background.	153
13.3	The number of tracks in background small-R jets in events passing the Resolved GGF WW Signal region selection vs. $\ln(p_T)$ for (a)Leading (b) Sub-Leading jets. The best fit line for the distribution is also shown, as well as the percentage of jets that pass a cut of number of tracks $< 4 \times \ln(p_T) - 5$. Note the number of total entries in these plots has been normalized to one.	154
13.4	The number of tracks in small-R jets in 300GeV Z' events passing the Resolved GGF WW Signal region selection vs. $\ln(p_T)$ for (a)Leading (b) Sub-Leading jets. The best fit line for the distribution is also shown, as well as the percentage of jets that pass a cut of number of tracks $< 4 \times \ln(p_T) - 5$.Note the number of total entries in these plots has been normalized to one.	154
13.5	The number of tracks in small-R jets in 500GeV Z' events passing the Resolved GGF WW Signal region selection vs. $\ln(p_T)$ for (a)Leading (b) Sub-Leading jets. The best fit line for the distribution is also shown, as well as the percentage of jets that pass a cut of number of tracks $< 4 \times \ln(p_T) - 5$.Note the number of total entries in these plots has been normalized to one.	155

13.6 The number of tracks in small-R jets in 700GeV Z' events passing the Resolved GGF WW Signal region selection vs. $\ln(p_T)$ for (a)Leading (b) Sub-Leading jets. The best fit line for the distribution is also shown, as well as the percentage of jets that pass a cut of number of tracks $< 4 \times \ln(p_T) - 5$.Note the number of total entries in these plots has been normalized to one.	155
13.7 The number of tracks in leading small-R jets in background events passing the Resolved GGF WW Signal region selection vs. $\ln(p_T)$ for (a)Gluons (b) Quarks jets. The best fit line for the distribution is also shown, as well as the percentage of jets that pass a cut of number of tracks $< 4 \times \ln(p_T) - 5$.Note the number of total entries in these plots has been normalized to one.	156
13.8 ROC Curve for Quark and Gluon Tagging with a cut on the number of tracks that depends on the $\ln(p_T)$	156
13.9 The top panel shows the distribution of m_{lvqq} with and without quark gluon tagging. The middle panel shows the ratio of the signals and backgrounds with and without quark gluon tagging. The bottom panel shows the change in S/\sqrt{B} with quark gluon tagging.	157
15.1 The top panel shows the distribution of m_{lvqq} with and without requiring jets to be true quarks. The middle panel shows the ratio of the signals and backgrounds with and without requiring jets to be true quarks. The bottom panel shows the change in S/\sqrt{B} when requiring jets to be true quarks.	165
15.2 Unfolded and extracted n_C qg dstbs.	166
15.3 PDGID of the truth-level parton matched to the small-R jets passing the Resolved GGF WW Signal Region selections for the (a) Leading (b) Sub-Leading jets . These distributions are shown for 300, 500, and 700GeV Z' signals and the background.	167

15.4 These figures show the impact of the uncertainties on the number of tracks in the leading jet in the sum of the background sample in the Resolved GGF WW SR (a) tracking efficiency (b) fake (c) PDF (d) ME (e) unfolding uncertainties. 168

List of Tables

2.1	Representations of the SM fermions under $SU(3)_C \times SU(2)_L \times U(1)_Y$ gauge symmetry group. $SU(2)_L$ gauge transformations allow one to go between rows and $SU(3)_C$ transformations allow one to go between columns in these fermion representations. [REWORD]	13
9.1	The list of triggers used in the analysis.	75
9.2	Summary of selection criteria used to define the signal region (SR), W +jets control region (W CR) and $t\bar{t}$ control region ($t\bar{t}$ CR) for merged 1-lepton channel.	85
9.3	The list of selection cuts in the resolved analysis for the WW and WZ signal regions (SR), W +jets control region (WR) and $t\bar{t}$ control region (TR).	86
9.4	Definitions of “inverted” leptons used in multijet control region . .	96
9.5	Fit validation result in WCRs for 2015+16 data. The fit is done in various WCRs, in order to obtain the corresponding scale factors for MJ templates: ggF resolved WCR for the $WW \rightarrow lvqq$ selection, ggF resolved untagged WCR for the $WZ \rightarrow lvqq$ selection, ggF resolved tagged WCR for the $WZ \rightarrow lvqq$ selection, VBF resolved WCR for the $WW \rightarrow lvqq$ selection, and VBF resolved WCR for the $WZ \rightarrow lvqq$ selection. Post-fit event yields for electroweak processes and MJ contributions are shown. The SF column shows the corresponding normalization scale factors for electroweak processes from the fit. R.U. stands for relative uncertainty.	108

12.1	Expected and Measured for DY WW $W+\text{jets}$, $t\bar{t}$ control regions and signal regions.	135
12.2	Expected and Measured for DY WZ $W+\text{jets}$, $t\bar{t}$ tag and untag control regions.	136
12.3	Expected and Measured for DY WZ $W+\text{jets}$, $t\bar{t}$ tag and untag signal regions.	137
12.4	Expected and Measured for VBF WW $W+\text{jets}$, $t\bar{t}$ control regions and signal regions.	138
12.5	Expected and Measured for VBF WZ $W+\text{jets}$, $t\bar{t}$ control regions and signal regions.	139
12.6	Fitted background normalizations for $t\bar{t}$ and $W+\text{jets}$ backgrounds for the DY WW analysis region.	140
12.7	Fitted background normalizations for $t\bar{t}$ and $W+\text{jets}$ backgrounds for the DY WZ analysis region.	140
12.8	Fitted background normalizations for $t\bar{t}$ and $W+\text{jets}$ backgrounds for the VBF WW analysis region.	140
12.9	Fitted background normalizations for $t\bar{t}$ and $W+\text{jets}$ backgrounds for the VBF WZ analysis region.	141

Abstract

Search for WW and WZ Resonances in $\ell\nu qq$ final states in pp collisions at

$\sqrt{s} = 13$ TeV with the ATLAS detector

by

Natasha Woods

This thesis presents a search for WW and WZ resonances using data from pp collisions at $\sqrt{s} = 13$ TeV using the ATLAS detector, corresponding to an integrated luminosity of 139 fb^{-1} . Diboson resonances are predicted in a number of Standard Model (SM) extensions, such as Extended Gauge Models, and Extra dimensional models. This search looks for resonances where one W boson decays leptonically and the other W or Z boson decays hadronically. This search is sensitive to diboson resonance production via vector-boson fusion as well as quark-antiquark annihilation and gluon-gluon fusion mechanisms. No significant excess of events is observed with respect to the Standard Model backgrounds, and constraints on the masses of new W' , Z' , and bulk-RS Gravitons are extended to up to 3.3 TeV, depending on the model. As the dominant backgrounds in this search contain gluons, classifying jets as quark-initiated or gluon-initiated would make this analysis more sensitive to new physics. Towards this end, this thesis provides a calibrated quark-gluon tagger based on the multiplicity of charged particles within a jet.

Loving Dedication

å

xix

Acknowledgments

Proper acknowledgments of everyone else who helped you graduate. Write later.

¹

Part I

²

Introduction

³ Chapter 1

⁴ Introduction

⁵ In general, humanity has continually strived to understand the structure and
⁶ dynamics of reality for widely varying reasons. Each academic field uses a spe-
⁷ cific set of concepts and models to describe nature. Physics is one such field,
⁸ that uses mathematical objects to systematically develop testable models about
⁹ the universe. Currently, the most fundamental types particles are fermions and
¹⁰ bosons. Fermions are the particles that make up the "ordinary" matter of the
¹¹ universe, while bosons are the quanta of the fundamental forces. The Standard
¹² Model (SM) of particle physics describes the quantum behavior of three of the
¹³ four fundamental forces: electromagnetic, strong, and weak forces.

¹⁴ The Standard Model has consistently described much of reality to an extreme
¹⁵ degree of accuracy. It has predicted cross sections for strong and electroweak
¹⁶ processes that span over ten orders of magnitude [see Fig. 3.1] and contains no
¹⁷ known logical inconsistencies. Despite the reality of the Standard Model, it still
¹⁸ fails to describe aspects of reality and suffers from aesthetic issues. The SM fails
¹⁹ to account for dark matter, dark energy, neutrino masses, the hierarchy of the
²⁰ fundamental force strengths, and other issues that may have not been noticed
²¹ yet! This incompleteness may indicate that a more fundamental theory exists. It

22 is hoped that such a theory would address the aforementioned phenomena and
23 the ad-hoc structure and parameter values of the SM. In particular the relative
24 scales of the fundamental forces impose oddly fine-tuned SM parameters, unless
25 there is additional structure at higher energies (e.g. between the electroweak and
26 Planck scales). This and other theoretical arguments motivate the search for new
27 physics at the TeV scale. The set of theories that hope to explain more of reality
28 are known as Beyond the Standard Model theories (BSM). Many of these theories,
29 if true, would revolutionize concepts of symmetry and space-time, which would
30 be intrinsically meaningful.

31 To probe the physics at this high energy frontier, physicists often collide ener-
32 getic particles that combine to produce massive particles, such as the Higgs boson
33 and top quark. The more energetic the colliding particles are the more massive
34 produced particles can be. Currently, the world's highest energy particle collider
35 is the Large Hadron Collider (LHC) at the European Organization for Nuclear
36 Research (CERN).

37 This thesis presents a search for WW and WZ resonances using data from pp
38 collisions at $\sqrt{s} = 13$ TeV using the ATLAS detector at CERN, corresponding
39 to an integrated luminosity of 139 fb^{-1} . Diboson resonances are predicted in a
40 number of BSM theories, such as Extended Gauge Models and Extra dimensional
41 models. This search looks for resonances where one W boson decays leptonically
42 and the other W or Z boson decays hadronically. This search is sensitive to
43 diboson resonance production via vector-boson fusion as well as quark-antiquark
44 annihilation and gluon-gluon fusion mechanisms (which will be collectively called
45 non-VBF modes).

46 To search for these new resonances, Monte-Carlo simulations are used to model
47 SM backgrounds and BSM signals. In these simulations, a series of optimized cuts

48 are used to create signal regions (SR) to identify the leptonic and hadronic decay
49 products of the resonance, maximize signal acceptance, and minimize background
50 contamination. In these regions, the resonance mass is calculated as the combined
51 system mass of the leptonic and hadronic system. The expected resonance mass
52 distribution from the simulated backgrounds and anticipated signal are compared
53 to data to search for the existence of these BSM signals (also known as a "bump
54 hunt"). Control regions enriched in the dominant backgrounds, $t\bar{t}$ and $W+\text{jets}$
55 (TCR and WCR, respectively) are constructed to be orthogonal to SRs and used
56 to determine the normalization of the $t\bar{t}$ and $W+\text{jets}$ backgrounds in SRs.

57 The VBF W' and Z' and ggF W' and Z' resonances studied have unique
58 SR and CR selections to maximize analysis sensitivity. RS Graviton signals are
59 probed using the same selections as the ggF Z' signal. Additionally, more mas-
60 sive resonances are more likely to have boosted W/Z bosons. As the boost of
61 the hadronically decaying boson increases the separation of its hadronic decay
62 products decreases. When the hadronically decaying boson has sufficient boost,
63 the two quarks will overlap and not be identified separately. For this reason, a
64 set of "resolved" selections are used when the hadronic decay products are recon-
65 structed separately, and "merged" selections when the decay products overlap and
66 identified as a single object in the event. A W/Z tagger identifies merged jets as
67 originating from a W/Z bosons based on jet substructure and mass cuts. However,
68 the more boosted the jet is the less likely it is to pass the jet substructure cut, due
69 to track merging. Consequently, the merged selection uses a high purity region
70 (HP), which requires that the jet pass both cuts, and low purity (LP) region where
71 the jet can fail the jet substructure cut.

72 The aforementioned SR definitions veto events with b -jets to minimize $t\bar{t}$ con-
73 tamination. However, b -jets are anticipated from W' resonances from the hadron-

74 ically decaying Z boson. To increase the signal acceptance of these resonances,
75 a $Z \rightarrow bb$ tagger is used to construct additional SR and CRs called the "tagged"
76 regions (and "un>tagged" if the event fails the $Z \rightarrow bb$ tagger).

77 For each signal model, the simulated and measured resonance mass distribu-
78 tions in the relevant SR and CRs are combined to construct a likelihood. This
79 likelihood is parameterized by the signal strength parameter, μ and systematic
80 uncertainties of the resonance mass distribution. This likelihood is used to quan-
81 tify the likelihood of a certain signal model given the anticipated backgrounds and
82 measured data.

83 No significant excess of events is observed with respect to the Standard Model
84 backgrounds, and constraints on the masses of new W' , Z' , and bulk-RS Gravi-
85 tons are extended to up to 3.3 TeV, depending on the model. As the dominant
86 backgrounds in this search contain gluons, classifying jets as quark-initiated or
87 gluon-initiated would improve the sensitivity of this analysis to new physics. To-
88 wards this end, this thesis provides a calibrated quark-gluon tagger based on the
89 multiplicity of charged particles within a jet.

90 Part II reviews the SM, its successes and shortcomings, and the aforemen-
91 tioned BSM theories that address the incompleteness of the SM. The structure
92 and performance of the ATLAS detector used is given in Part III.

Part II

93

Theoretical Motivation

94

⁹⁵ **Chapter 2**

⁹⁶ **The Standard Model of Particle**

⁹⁷ **Physics**

⁹⁸ **2.1 Introduction**

⁹⁹ By determining the dynamics of the most elementary degrees of freedom, par-
¹⁰⁰ ticle physics hopes to uncover the fundamental laws of the universe. The definition
¹⁰¹ of elementary has evolved through time and currently refers to matter and force
¹⁰² mediating particles: fermions and bosons, respectively. The Standard Model of
¹⁰³ Particle Physics (SM) describes the quantum behavior of three of the four funda-
¹⁰⁴ mental forces: weak, strong, and electromagnetic, via boson and fermion interac-
¹⁰⁵ tions. Gravity is not included in the SM and still under investigation.

¹⁰⁶ **2.2 Quantum Field Theory**

¹⁰⁷ In the SM, forces (and particles) are represented as fields. In this context,
¹⁰⁸ fields are mathematical objects that define a tensor (e.g. scalar, vector, etc) at
¹⁰⁹ every point on a manifold, here the manifold is space-time. These fields obey laws

110 dictated by Quantum Field Theory (QFT). Particles arise naturally in QFT as
111 quantized field excitations localized in spacetime.

112 According to Noether's theorem, symmetries of a field give rise to conserved
113 quantities (e.g. time-translation invariance leads to energy conservation). Often
114 in the history of physics, a conserved quantity of a field is found and then the
115 underlying symmetry of the field is inferred. Gauge symmetries are symmetries
116 among the internal degrees of freedom of the field (components of the tensor),
117 which give rise to quantities associated with fields. By specifying the symmetries
118 of a system the dynamics and conserved quantities of the system may be succinctly
119 defined.

120 2.3 $U(1)_{EM}$ Local Gauge Invariance

121 The Lagrangian of Quantum Electrodynamics (QED) describes the electro-
122 magnetic force. QED may be derived by requiring local $U(1)_{EM}$ gauge invariance
123 of the free dirac fermion Lagrangian, ψ :

$$\mathcal{L} = i\bar{\psi}\gamma^\mu\partial_\mu\psi - m\bar{\psi}\psi \quad (2.1)$$

124 This symmetry may be represented as a complex number with unit modulus,
125 $e^{i\theta}$. $U(1)$ gauge invariance requires this gauge transformation of ψ will leave the
126 Lagrangian unchanged.

$$\psi(x) \rightarrow \psi'(x) = e^{i\theta(x)}\psi(x) \quad (2.2)$$

127 NB: This transformation is a local gauge transformation as θ depends on the
128 spacetime coordinate.

129 By requiring this symmetry of the free Dirac fermion Lagrangian:

$$\mathcal{L} = i\bar{\psi}\gamma^\mu\partial_\mu\psi - m\bar{\psi}\psi \quad (2.3)$$

₁₃₀ The mass term is unaffected, but the kinetic term is modified due to $\theta(x)$.

$$\mathcal{L} \rightarrow \mathcal{L}' = i\bar{\psi}e^{-i\theta(x)}\gamma^\mu\partial_\mu\psi e^{i\theta(x)} - m\bar{\psi}e^{-i\theta(x)}\psi e^{i\theta(x)} \quad (2.4)$$

₁₃₁

$$= i\bar{\psi}\gamma^\mu(\partial_\mu\psi + i\psi\partial_\mu\theta) - m\bar{\psi}\psi \quad (2.5)$$

₁₃₂ The $\partial_\mu\theta$ terms breaks the gauge invariance of the Lagrangian. By introducing a
₁₃₃ new field, A_μ we can recover the gauge invariance of the derivative. Now redefining
₁₃₄ the derivative as the covariant derivative:

$$D_\mu\psi \equiv (\partial_\mu - iqA_\mu)\psi \quad (2.6)$$

₁₃₅ And letting A_μ transform under $U(1)$ as:

$$A_\mu \rightarrow A_\mu + \delta A_\mu \quad (2.7)$$

₁₃₆ The transformed covariant derivative becomes:

$$D_\mu\psi \rightarrow D_\mu\psi' = (\partial_\mu - iqA_\mu)\psi' \quad (2.8)$$

₁₃₇

$$= (\partial_\mu - iq(A_\mu + \delta A_\mu))\psi e^{i\theta} \quad (2.9)$$

₁₃₈

$$= e^{i\theta}D_\mu + ie^{i\theta}\psi(\partial_\mu\theta - q\delta A_\mu) \quad (2.10)$$

₁₃₉ The covariant derivative can be made gauage invariant by setting the last term
₁₄₀ to zero.

$$\delta A_\mu = \frac{1}{q} \partial_\mu \theta \quad (2.11)$$

¹⁴¹ So now A_μ transforms as:

$$A_\mu \rightarrow A_\mu + \frac{1}{q} \partial_\mu \theta \quad (2.12)$$

¹⁴² Finally, replacing the derivative with the covariant derivative the Dirac La-
¹⁴³ grangian we have:

$$\mathcal{L} = i\bar{\psi}\gamma^\mu D_\mu \psi - m\bar{\psi}\psi - \frac{1}{4}F_{\mu\nu}F^{\mu\nu} \quad (2.13)$$

¹⁴⁴

$$= \mathcal{L}_{QED} \quad (2.14)$$

¹⁴⁵ Here $F_{\mu\nu} \equiv \partial_\mu A_\nu - \partial_\nu A_\mu$. This last term in the Lagrangian is the kinetic
¹⁴⁶ energy of the gauge boson field.

¹⁴⁷ So we have derived the QED Lagrangian. By requiring the free Dirac La-
¹⁴⁸ grangian to be invariant under U(1) transformations we have generated a new
¹⁴⁹ gauge boson field, A_μ , which describes the photon. As expected the photon inter-
¹⁵⁰ acts with fermions.

¹⁵¹ Stepping back, a global U(1) gauge symmetry of the free Dirac Lagrangian
¹⁵² implies we cannot measure the absolute phase of a charged particle. A local U(1)
¹⁵³ gauge symmetry changes the phase of fields differently across space time. For this
¹⁵⁴ type of transformation to leave the Lagrangian invariant, we had to introduce an
¹⁵⁵ additional field, A_μ , which "communicates" these phase changes across space-time.
¹⁵⁶ In less formal language this effectively means: if the field at one location changes,
¹⁵⁷ this change is conferred to other particles via A_μ .

¹⁵⁸ 2.4 Yang-Mills Gauge Theories

¹⁵⁹ Requiring $U(1)_{EM}$ gauge invariance of the free Dirac Lagrangian gave us QED.

¹⁶⁰ Requiring different gauge symmetries we can derive the structure of other inter-

¹⁶¹ actions. Any gauge symmetry may be written as:

$$\psi_i \rightarrow \exp(i\theta^a T_{ij}^a) \psi_j \quad (2.15)$$

¹⁶² Here θ is a dimensionless real parameter and T is the generator of the gauge

¹⁶³ symmetry group. With this the covariant derivative can be written as:

$$D_\mu \psi_i \equiv \partial_\mu \psi_i + ig A_\mu^a T_{ij}^a \psi_j \quad (2.16)$$

¹⁶⁴ Then the gauge field must transform as:

$$A_\mu^a \rightarrow A_\mu^a - \frac{1}{g} \partial_\mu \theta^a - f^{abc} \theta^b A_\mu^c \quad (2.17)$$

¹⁶⁵ Here f is the structure constant of the gauge group. The field strength tensor

¹⁶⁶ is given by:

$$F_{\mu\nu}^a \equiv \partial_\mu A_\nu^a - \partial_\nu A_\mu^a - g f^{abc} A_\mu^b A_\nu^c \quad (2.18)$$

¹⁶⁷

$$F_{\mu\nu}^a \rightarrow F_{\mu\nu}^a - f^{abc} \theta^b F_{\mu\nu}^c \quad (2.19)$$

¹⁶⁸ This gives the Yang-Mills Lagrangian:

$$\mathcal{L}_{YM} = -\frac{1}{4} F_{\mu\nu}^{a\mu\nu} F_{\mu\nu}^a + i \bar{\psi}_i \gamma^\mu D_\mu \psi_i + m \bar{\psi}_i \psi_i \quad (2.20)$$

¹⁶⁹ 2.5 Particles in the Standard Model

¹⁷⁰ The SM consists of fermions (half-integer spin matter constituents) and bosons
¹⁷¹ (integer spin force mediators). Fermions are spinor representations of the Poincare
¹⁷² group and can be further separated into leptons and quarks. Bosons are the result
¹⁷³ of requiring a particular symmetry among the spinor fields:

$$SU(3)_C \times SU(2)_L \times U(1)_Y \quad (2.21)$$

¹⁷⁴ $SU(3)_C$ is the symmetry group of the strong force and generates eight gluon
¹⁷⁵ fields, G_μ . $SU(2)_L$ is the symmetry group of the Electroweak force and generates
¹⁷⁶ three electroweak boson fields. The mixing of this $SU(2)_L$ and $U(1)_Y$ gives rise
¹⁷⁷ to the photon field, where Y is the weak-hypercharge:

$$Y = 2(Q - T_3) \quad (2.22)$$

¹⁷⁸ Q is the electromagnetic charge, and T_3 is the z-component of the weak isospin.
¹⁷⁹ Weak isospin is the charge associated with the $SU(2)_L$ symmetry. The correspond-
¹⁸⁰ ing covariant derivative is then:

$$D_\mu \phi \equiv (\partial_\mu + ig_1 B_\mu Y_{L/R} + [ig_2 W_\mu^\alpha T^\alpha]_L + [ig_3 G_\mu^\alpha \tau^\alpha]_C) \psi \quad (2.23)$$

¹⁸¹ It is important to note that the gauge symmetry of the SM yields a particular
¹⁸² structure of the fermion representations. So for a given fermion to interact with
¹⁸³ a given gauge field it must have a non-zero corresponding Noether charge for
¹⁸⁴ that gauge symmetry. If the corresponding Noether charge is zero, that fermion
¹⁸⁵ transforms as a singlet and does not participate in that gauge interaction.

¹⁸⁶ Fermions are divided into quarks and leptons based on their transformations
¹⁸⁷ under $SU(3)_C$. Quarks transform as color triplets. Leptons transform as color

singlets and consequently do not interact with gluons. Fermions may be further
 classified by their $SU(2)_L$ interactions. Only the left-chiral part of fermions (denoted by L here) transform as $SU(2)_L$ doublets, the right-chiral part forms singlets under this gauge. Lastly, all these groups of particles come in three generations, each a heavier copy of the previous, but with differing flavor quantum numbers.
 This is summarized in Table 2.1 and shown in Figures 2.1 and 2.2.

SM Fermion Gauge Group	First Generation	Second Generation	Third Generation	$(SU(3)_C, SU(2)_L, U(1)_Y)$ Representations
Left-handed quarks	$\begin{pmatrix} u_L^r & u_L^g & u_L^b \\ d_L^r & d_L^g & d_L^b \end{pmatrix}$	$\begin{pmatrix} c_L^r & c_L^g & c_L^b \\ s_L^r & s_L^g & s_L^b \end{pmatrix}$	$\begin{pmatrix} t_L^r & t_L^g & t_L^b \\ b_L^r & b_L^g & b_L^b \end{pmatrix}$	$(3, 2, \frac{1}{6})$
Right-handed quarks	(u_R^r, u_R^g, u_R^b) (d_R^r, d_R^g, d_R^b)	(c_R^r, c_R^g, c_R^b) (s_R^r, s_R^g, s_R^b)	(t_R^r, t_R^g, t_R^b) (b_R^r, b_R^g, b_R^b)	$(3, 1, \frac{2}{3})$ $(3, 1, -\frac{1}{3})$
Left-handed leptons	$\begin{pmatrix} \nu_e^L \\ e_L \end{pmatrix}$	$\begin{pmatrix} \mu_e^L \\ \mu_L \end{pmatrix}$	$\begin{pmatrix} \tau_e^L \\ \tau_L \end{pmatrix}$	$(1, 2, -\frac{1}{2})$
Right-handed leptons	e_R	μ_R	τ_R	$(1, 1, -1)$

Table 2.1: Representations of the SM fermions under $SU(3)_C \times SU(2)_L \times U(1)_Y$ gauge symmetry group. $SU(2)_L$ gauge transformations allow one to go between rows and $SU(3)_C$ transformations allow one to go between columns in these fermion representations. [REWORD]

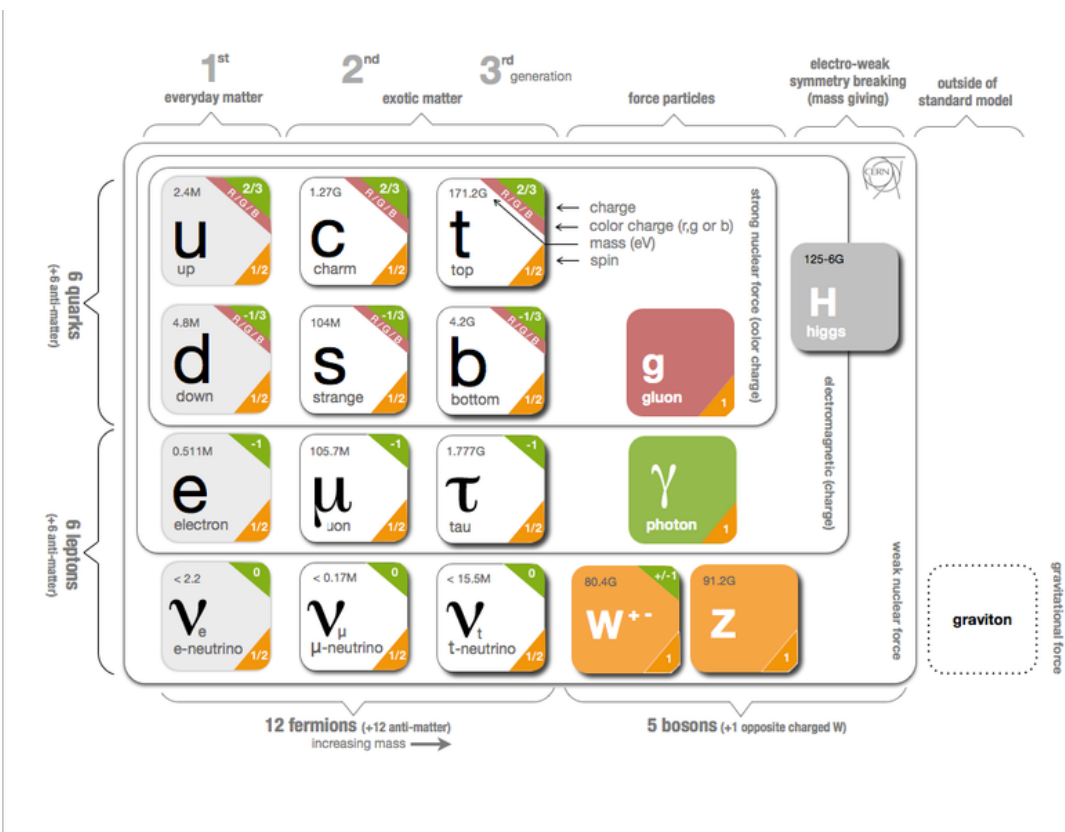


Figure 2.1: The particles of the Standard Model.



Figure 2.2: Summary of how Standard Model particles interact with other Standard Model particles.

¹⁹⁴ Now we can understand the SM Lagrangian density as a Yang-Mills theory
¹⁹⁵ with the gauge group: $SU(3)_C \times SU(2)_L \times U(1)_Y$ with an additional $SU(2)$ complex
¹⁹⁶ scalar Higgs field doublet that will be discussed later.

$$\begin{aligned} \mathcal{L}_{SM} = & \underbrace{-\frac{1}{4}B_{\mu\nu}B^{\mu\nu} - \frac{1}{4}W_{\mu\nu}^aW^{a\mu\nu} - \frac{1}{4}G_{\mu\nu}^\alpha G^{\alpha\mu\nu}}_{\text{Kinetic Energies and Self-Interactions of Gauge Bosons}} \\ & + \underbrace{\bar{L}_i \gamma^\mu (i\partial_\mu - \frac{1}{2}g_1 Y_{iL} B_\mu - \frac{1}{2}g_2 \sigma^a W_\mu^a) L_i}_{\text{Kinetic Energies and EW Interactions of Left-handed Fermions}} \\ & + \underbrace{\bar{R}_i \gamma^\mu (i\partial_\mu - \frac{1}{2}g_1 Y_{iR} B_\mu) R_i}_{\text{Kinetic Energies and EW Interactions of Right-Handed Fermions}} \\ & + \underbrace{\frac{ig_3}{2} \bar{Q}_j \gamma^\mu \lambda^\alpha G_\mu^\alpha Q_j}_{\text{Strong Interactions between Quarks and Gluons}} \\ & + \underbrace{\frac{1}{2} |(i\partial_\mu - \frac{1}{2}g_1 B_\mu - \frac{1}{2}g_2 \sigma^a W_\mu^a)\Phi|^2 - V(\Phi)}_{\text{Electroweak Boson Masses and Higgs Couplings}} \\ & - (\underbrace{y_{kl}^d \bar{L}_k \Phi R_l + y_{kl}^u \bar{R}_k \tilde{\Phi} L_l}_{\text{Fermion Mass terms and Higgs Couplings}} + h.c.) \end{aligned}$$

¹⁹⁷ Here several abstract spaces are being spanned:

- ¹⁹⁸ – a spans the three $SU(2)_L$ gauge fields with generators expanded in Pauli matrices, $T^\alpha = \frac{1}{2}\sigma^\alpha$
- ¹⁹⁹ – α spans the eight $SU(3)_C$ gauge fields, with generators expanded in Gell-Mann matrices, $\tau^\alpha = \frac{1}{2}\lambda^\alpha$
- ²⁰⁰ – L/R represent left and right projections of Dirac fermion fields. The Strong interaction is not chiral, so $Q = L+R$
- ²⁰¹
- ²⁰²
- ²⁰³

204 – μ and ν are four-vector indices

205 – i, j, k are summed over the three generations of SM particles.

206 2.6 Higgs Mechanism

207 The SM Lagrangian without the addition of a Higgs field does not allow for
208 gauge boson and fermion mass terms: $\frac{1}{2}m_A^2 A_\mu A_\mu$ and $m(\bar{\psi}\psi)$, as these terms are
209 not gauge invariant. By introducing the Higgs field, mass terms for these particles
210 may be included in a gauge invariant way. This field is a complex doublet with a
211 potential $V(\Phi)$:

$$\Psi = \begin{pmatrix} \Phi^\dagger \\ \Phi^0 \end{pmatrix} \quad (2.24)$$

212 $V(\Phi) = \mu^2 \Phi^\dagger \Phi + \lambda |\Phi^\dagger \Phi|^2 \quad (2.25)$

213 The minima of this field occurs for $|\Phi| = \sqrt{\frac{\mu^2}{2\lambda}} \equiv \frac{v}{2}$. This yields degenerate
214 minima, this symmetry is broken by choosing a specific minima (a.k.a. sponta-
215 neous symmetry breaking). By convention $\Phi_{min} = \frac{1}{\sqrt{2}} \begin{pmatrix} 0 \\ v \end{pmatrix}$ is chosen. This means
216 the ground state of the Higgs field (Higgs vacuum) is non-zero, $\sqrt{\frac{-\mu^2}{\lambda}}$. The Higgs
217 Field may now be expanded around this new ground state:

$$\Phi(x) = \frac{1}{\sqrt{2}} \begin{pmatrix} 0 \\ v + h(x) \end{pmatrix} \quad (2.26)$$

218 This non-zero Higgs vacuum now generates mass terms for the gauge bosons
219 from the following term in the Lagrangian:

$$|(-\frac{1}{2}g_1B_\mu - \frac{1}{2}g_2\sigma^aW_\mu^a)\Phi|^2 = \frac{1}{2}m_W^2W_\mu^+W^{-\mu} + \frac{1}{2}m_Z^2Z_\mu Z^\mu \quad (2.27)$$

220 where:

$$W_\mu^\pm \equiv \frac{1}{\sqrt{2}}(W_\mu^1 \mp iW_\mu^2) \quad (2.28)$$

$$\begin{aligned} \text{221} \quad Z_\mu &\equiv \frac{1}{\sqrt{g_1^2 + g_2^2}}(g_2W_\mu^2 - g_1B_\mu) \end{aligned} \quad (2.29)$$

$$\begin{aligned} \text{222} \quad m_W &= \frac{vg_2}{\sqrt{2}} \end{aligned} \quad (2.30)$$

$$\begin{aligned} \text{223} \quad m_Z &= \frac{v}{\sqrt{2}}\sqrt{g_1^2 + g_2^2} \end{aligned} \quad (2.31)$$

224 The Higgs field also generates a mass term for the Higgs boson and self-
225 interactions for the Higgs boson.

226 2.7 Electroweak Theory

227 $SU(2)_L$ generates W^\pm, W^0 gauge bosons, which would be massless if $SU(2)_L$
228 was a perfect symmetry. These bosons are massive as this symmetry is broken.

229 The mass eigenstates, Z and γ given by:

$$\begin{pmatrix} Z_\mu \\ A_\mu \end{pmatrix} = \begin{pmatrix} \cos\theta_W & -\sin\theta_W \\ \sin\theta_W & \cos\theta_W \end{pmatrix} \begin{pmatrix} W_\mu^3 \\ B_\mu \end{pmatrix} \quad (2.32)$$

230 Here θ_W is the Weinberg angle given by:

$$\cos\theta_W = \frac{g_2}{\sqrt{g_1^2 + g_2^2}} = \frac{m_W}{m_Z} \quad (2.33)$$

231 2.8 Quantum ChromoDynamics

232 As mentioned earlier the Strong Force, which binds the proton together, is
233 mediated by gluons. Quantum Chromodynamics is the QFT which describes the
234 interactions of quarks and gluons via $SU(3)_C$ symmetry. QCD contains features
235 not present in Electroweak Interactions due to $SU(3)_C$ generators not commuting
236 (a.k.a. $SU(3)_C$ is a non-abelian group). For example, in QCD there is color
237 confinement and asymptotic freedom due to the structure constants being non-
238 zero. Requiring $SU(3)_C$ local gauge invariance implies:

$$\psi(x) \rightarrow \psi(x)' = \exp[i g_S \alpha(x) \cdot \hat{T}] \psi(x) \quad (2.34)$$

239 where $\alpha(x)$ is the local phase function, g_S is the strong coupling constant, and
240 \hat{T} are the eight generators of $SU(3)$ (note $\hat{T}^a = \frac{1}{2}\lambda^a a$, where λ^a are the Gell-Mann
241 matrices). As the Gell-Mann matrices are 3x3, this means ψ has three degrees of
242 freedom under these $SU(3)$ rotations. So we represent ψ under $SU(3)$ rotations
243 as:

$$\psi = \begin{pmatrix} \psi_{red} \\ \psi_{green} \\ \psi_{blue} \end{pmatrix} \quad (2.35)$$

244 Consequently, particle fields transforming under $SU(3)$ rotations have three
245 components which physicists describe as color components (red, green, and blue).
246 A particle's corresponding antiparticle has the corresponding anticolor. This color
247 is the "charge" of QCD and is conserved under $SU(3)$ rotations. Combining colors,
248 color neutral states (e.g. red and antired, or red, green and blue) may be created.
249 For the Free Dirac Lagrangian to remain invariant under $SU(3)$ transformations,
250 we must again postulate a boson field that modifies the derivative. The gluon

251 field tensor is given by ($\alpha = 1, \dots, 8$):

$$G_{\mu\nu}^k = \partial^\mu G_\alpha^\nu - \partial^\nu G_\alpha^\mu - g_S f^{\alpha\beta\gamma} G_\beta^\mu G_\gamma^\nu \quad (2.36)$$

252 Here $f^{\alpha\beta\gamma}$ are the structure constants of $SU(3)$. Combining all this gives the
253 QCD Lagrangian:

$$\mathcal{L}_{QCD} = \bar{\psi}_q i\gamma^\mu (D_\mu)_{ij} \psi^{qj} - m \bar{\psi}^{qi} \psi_{qi} - \frac{1}{4} G_{\mu\nu}^\alpha G^{\alpha\mu\nu} \quad (2.37)$$

254 Here i are the color indices, and q are the quark flavors. It is important to
255 note that quarks transform under the fundamental representation of $SU(3)$, while
256 gluons transform under the adjoint representation. This means quarks carry a
257 single color charge (red, green, blue, antired, antigreen, antiblue) and gluons carry
258 a color and anticolor charge.

259 Figure 2.3 shows the three dominant QCD interactions. Since gluons carry
260 color charge, they interact with one another. This does not occur in QED, as
261 photons do not have electric charge and therefore do not interact with each other.
262 In QED, a bare electron's effective charge is largest closest to the electron and
263 decreases as a function of distance. This is because the QED vacuum fills with
264 particle antiparticle pairs spontaneously, which screen the charge of the bare elec-
265 tron. The larger the distance from the electron, the smaller the effective charge
266 and therefore the weaker the force. So for a pair of electrons, as the distance
267 between them increases the repulsive force decreases and they may be observed
268 separately.

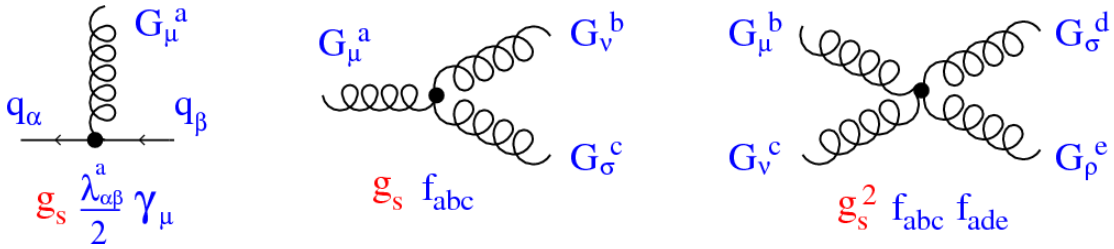


Figure 2.3: This figure shows the three dominant QCD interactions. From Ref. [17]

As the distance from a quark increases it's effective color charge increases due
 to the vacuum polarization in QCD. Color charge grows as the distance from
 the source increases (a.k.a. color is anti-screened in QCD). In this way, strong
 interactions become stronger at large distances (low momenta interactions). At
 small distances (large momenta interactions) strong interactions are significantly
 weaker and considered nearly free. This effect of referred to as asymptotic freedom.
 At large distances, a quark's effective charge is large and the strong force is more
 significant. This force becomes so strong that quarks form colorless bound states
 instead of remaining free particles. This effect is known as color confinement.
 This running of all SM fields is shown in Figure 2.4.



Figure 2.4: Strength of the U(1), SU(2), and SU(3) gauge couplings as a function of the energy scale of the interaction (Q). From Ref. [11]

Commonly the change in a particle's effective charge under a given force is quantified with $\beta(r) \equiv -\frac{de(r)}{d\ln r}$, where $e(r)$ is the effective charge of a given particle under a force. In QED this function is positive but in QCD this function is negative leading to confinement and asymptotic freedom. Moreover, one can calculate how the coupling (α) of a force varies with energies. (More deeply this amounts to incorporating renormalization and vacuum polarization in the boson propagators).

For QCD this is:

$$\alpha_S(x) = \frac{\alpha_S(\mu^2)}{1 + \beta_0 \alpha_S(\mu^2) \ln(Q^2/\mu^2)} \quad (2.38)$$

286

$$\beta_0 = \frac{11N_c - 2n_f}{12\pi} \quad (2.39)$$

287 where Q is the momentum of the the force is probed at, μ^2 is the renormalization scale.

289 As stated previously, quarks and gluons have not been observed in isolation.
290 Instead they form bound colorless states. Hadronization is the process by which
291 quarks and gluons form hadrons. The process of hadronization is still an active
292 area of research. One qualitative description is show in Figure [Natasha add
293 figure]. In this figure, as two quarks separate the color field between them is
294 restricted to a tube with energy density of 1GeV/fm. As they separate further,
295 the energy in the color field increases, until there is enough energy to produce
296 $q\bar{q}$ pairs, which breaks the color field. This process repeats until quarks and
297 antiquarks have low enough energy to form colorless hadrons. The resulting spray
298 of hadrons is called a jet.

299 Since quarks and gluons carry different color charges, their respective jets have
300 different properties. As quarks carry only a single color charge (vs. gluons which
301 have color and anticolor charge), so their jets have less constituent particles. More
302 precisely, the Altarelli-Parisi splitting functions [3] contain a factor C_A for gluon
303 radiation off a gluon and C_F for gluon radiation off a quark ($C_A/C_F = 9/4$). These
304 color factors are the prefactor in the Feynman diagrams for these processes [1],
305 which leads to gluon jets having more constituents and therefore more tracks than
306 quark jets. Gluon jets also tend to have a larger radius with lower momentum
307 constituents than quarks. There are many novel techniques to distinguish quarks
308 from gluons. For this study the number of charged particles will be focused on.

309 **Chapter 3**

310 **Standard Model Successes and
311 Limitations**

312 The Standard Model has consistently described much of reality to an extreme
313 degree of accuracy. It has predicted cross sections for strong and electroweak pro-
314 cesses that span over ten order of magnitude correctly [see Fig. 3.1] and contains
315 no known logical inconsistencies. Despite the strength and reality of the Stan-
316 dard Model, it still fails to describe aspects of reality and suffers from aesthetic
317 issues. To date, dark matter and energy comprise 95% of the universe, but are
318 not accounted for in the SM. Additionally, neutrinos are known to have mass but
319 are massless in the SM. There are mechanisms for introducing massive neutrinos
320 in the SM, but these mechanisms create hierarchy problems.

321 Possibly the most significant aesthetic issue is the hierarchy between the elec-
322 troweak and Planck scales. The electroweak scale is the scale of electroweak
323 symmetry breaking. The Planck scale is the scale where the gravitational force
324 is comparable in strength to the other forces. The Planck scale is where the SM
325 breaks down, as there is not an experimentally verified theory of quantum gravity,
326 and at this scale gravity cannot be ignored (like it can at the electro-weak scale).

327 These scales differ by ~ 30 orders of magnitude. Understanding the difference
328 in these energy scales, may help explain the weakness of gravity at electroweak
329 scales, and possibly a QFT for gravity. (NB: This hierarchy can also be framed in
330 terms of the corrections to the Higgs mass, which depend on the UV cutoff scale -
331 where the SM is suppose to break, which is taken at the Planck scale. This leads
332 the quantum corrections to the Higgs mass to force the Higgs mass to 10^{18} TeV.)

333 These stark contrasts in scales may indicate that a more fundamental theory
334 exists. It is hoped that such a theory would explain and motivate some of the ad-
335 hoc features of the SM. In particular, there currently are no experimentally verified
336 explanations of why there are three generations of fermions, the values of the 19
337 SM parameters (6 quark masses, 3 charged lepton masses, 3 gauge couplings,
338 Higgs parameters (μ^2, λ)), the structure of the fermion representations, etc.

Standard Model Production Cross Section Measurements

Status: July 2018

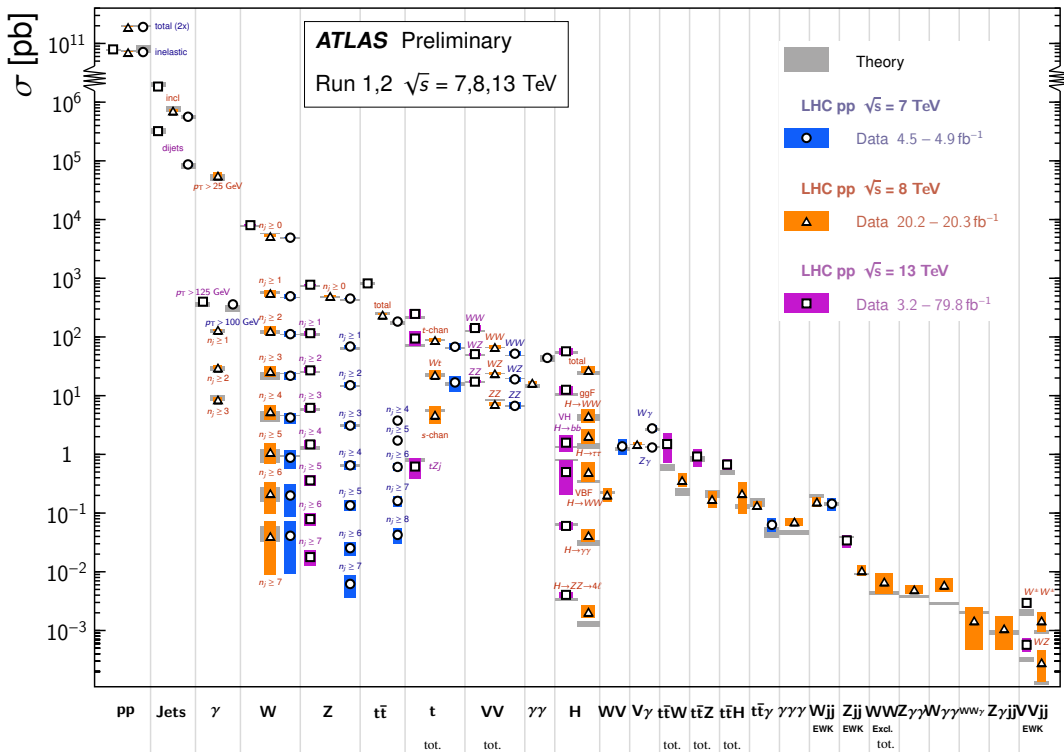


Figure 3.1: A comparison of cross section measurements at $\sqrt{s} = 7, 8, 13 \text{ TeV}$ from ATLAS compared to theoretical measurements. From Ref. [5]

³³⁹ **Chapter 4**

³⁴⁰ **New Physics Models with**
³⁴¹ **Diboson Resonances**

³⁴² **4.1 Randall Sundrum Bulk Model**

³⁴³ The electroweak-planck hierarchy may be explained by the existence of extra
³⁴⁴ dimensions, like the 5D Randall Sundrum Bulk Model ([18], [2]). In this model,
³⁴⁵ there is one extra warped spatial dimension, y , with a metric:

$$ds^2 = e^{-2k|y|} \eta_{\mu\nu} dx^\mu dx^\nu + dy^2 \quad (4.1)$$

³⁴⁶ where $e^{-k|y|}$ is the warp factor of the extra dimension, which is compactified on
³⁴⁷ a S^1/Z_2 orbifold (a.k.a. a circle where $y \rightarrow -y$). This can be visualized as every
³⁴⁸ point in space time having a line extending from it a distance L , representing
³⁴⁹ this fifth dimension. At the end of this line is the Planck brane. This fourth
³⁵⁰ spatial dimension separates two 4-D branes: Planck brane and TeV brane. We
³⁵¹ live on the TeV brane, as shown in Figure 4.1. The Higgs field (and to a lesser
³⁵² degree the top quark and graviton fields) is localized near the TeV Brane, while

353 the light fermion fields are localized more near the Planck brane. Fundamental
 354 parameters are set on the Planck brane. The warp factor may be scaled away from
 355 all dimensionless SM terms by field redefinitions. However, the only dimensionful
 356 parameter, $m_H^2 = v^2$ is rescaled by $\tilde{v} \sim e^{-kL} M_{Pl} \sim 1\text{TeV}$ for $kL \sim 35$, explaining
 357 why gravity is so weak on the TeV brane. Also, by localizing the light fermion
 358 fields near the Planck brane and top and graviton fields near the TeV brane, the
 359 light quarks will have smaller masses.

360 The two free parameters of this theory are M_{Pl} and k . Based on this RS Bulk
 361 model, all SM particles should have Kaluza-Klein (KK) excitations. In particular,
 362 the graviton would have KK excitations that prefer to decay to WW or ZZ, which
 363 is why this analysis searches for RS Gravitons.

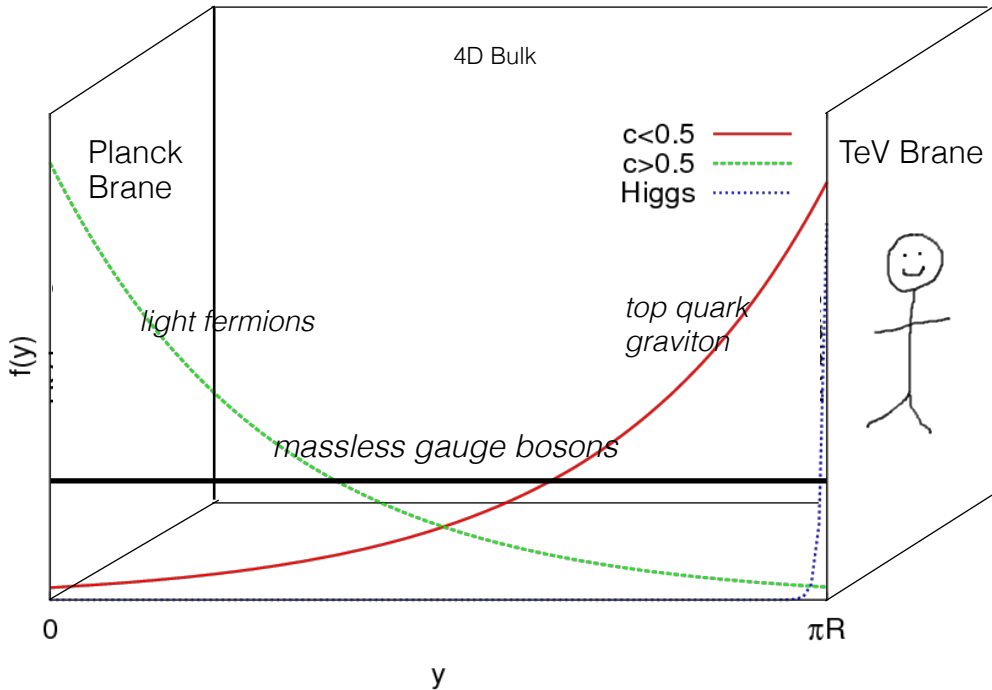


Figure 4.1: Cartoon of RS Bulk Model

³⁶⁴ 4.2 Simple Standard Model Extensions

³⁶⁵ The RS Bulk model is motivated by resolving the hierarchy problem. Ex-
³⁶⁶ tending the Scalar sector is a natural space to look for new physics due to the
³⁶⁷ complexity of fermion and boson groups. There are many other interesting and
³⁶⁸ well motivated frameworks, but there is a lack of completely predictive models,
³⁶⁹ due to model flexibility (free parameters). Therefore it is hard for experimentalists
³⁷⁰ to know which theories to search for in data. However, as seen in [16], a "Simpli-
³⁷¹ fied Model" approach may be taken. In the search for reasonably narrow width
³⁷² particles, as in this search, the search is not sensitive to all the details and free
³⁷³ parameters of the theory. Generally such searches are only sensitive to the reso-
³⁷⁴ nance mass and its interactions. Therefore, a theory's Lagrangian may be reduced
³⁷⁵ to only retain this information (mass parameters and couplings). Experimental
³⁷⁶ results using this framework may then be reinterpreted in a given theory.

³⁷⁷ In the simplified approach, the new resonance searched for is represented as
³⁷⁸ a real vector field in the adjoint representation of $SU(2)_L$ with vanishing hyper-
³⁷⁹ charge. This results in one neutral and two charged bosons. Defined as:

$$V^\pm = \frac{V_\mu^1 \mp i V_\mu^2}{\sqrt{2}} \quad (4.2)$$

³⁸⁰ $V_\mu^0 = V_\mu^3 \quad (4.3)$

³⁸¹ The SM Lagrangian is then augmented with the additional terms:

$$\mathcal{L} \supset -\frac{1}{4} D_{[\mu} V_{\nu]}^a D^{[\mu} V^{\nu]a} + \frac{m_V^2}{2} V_\mu^a V^{a\mu} + ig_V c_H V_\mu^a H^\dagger \tau^a \overset{\leftrightarrow}{D}{}^\mu H + \frac{g^2}{g_V} c_F V_\mu^a J_F^{\mu a} \quad (4.4)$$

³⁸² In order the terms represent: the kinetic, V mass, Higgs- V interaction, and
³⁸³ V -left-handed fermion interaction terms. Phenomenologically the three physical

384 particles this predicts are degenerate, where V couples most strongly to VV , via
385 the g_V coupling factor. The dominant production modes are DY and VBF.

386 Two versions of HVT are considered, Model A and B. Model A is a weakly
387 coupled model where $g_V \sim 1$, like the extended gauge symmetry discussed in Ref
388 . [16]. Model B is a strongly coupled model, where $1 < g_V < 4\pi$. The width
389 of the resonance grows with g_V so for this narrow resonance search only g_V is
390 chosen to be less than 6 (so $\Gamma/M < 10\%$). More precisely, the coupling of these
391 resonances to fermions scales as $g_f = g^2 c_F/g_V$, where g is the SM $SU(2)_L$ gauge
392 coupling and c_F is the free parameter (expected to be of order 1 for Model A and
393 B). This then means that for Model B the coupling to fermions is more suppressed
394 than for Model A, leading to a smaller DY production rate and BR to fermionic
395 final states. The coupling of V to SM bosons scales as $g_H = g_V c_H$, where c_H is
396 a free parameter on the order of 1 for Model A and B. So for small values of g_V
397 (i.e. Model A - weakly coupled theories) the BR to gauge bosons is smaller than
398 for Model B. So weakly coupled vectors have large production cross sections and
399 decay prominently to leptons or jets, while strongly coupled vectors are produced
400 less and decay predominantly to gauge bosons.

401 Vectors in Model A and B are generally produced via quark-anti-quark annihi-
402 lation. The more rare production via vector-boson-fusion is considered by setting
403 $g_H = 1$ and $g_F = 0$. In Model B diboson final states are enhanced as stated
404 previously due to g_H and moreover the BR to WZ , WH , WW , and ZH are the
405 same.

406 In summary, V couples most strongly to left-handed fermions and VV depen-
407 dent on g_V .

408

Part III

409

Experimental Setup

410 **Chapter 5**

411 **LHC**

412 The Large Hadron Collider (LHC) is the highest-energy particle collider in the
413 world. It was designed to expand the frontier of high energy particle collisions in
414 energy and luminosity. This enables LHC experiments to test the Standard Model
415 and search for new physics at higher energies than tested with previous colliders.
416 Collisions at higher energies not only produce more massive particles but also
417 more weakly interacting particles. Fig. 5.1 shows production cross sections for
418 various processes at hadron colliders. The rate for electroweak physics processes
419 including W and Z scale with the center-of-momentum energy, \sqrt{s} .

420 The LHC consists of a 26.7 km (17 miles) ring, approximately 100 m un-
421 derground, outside Geneva, Switzerland. Counter-circulating proton (and occa-
422 sionally heavy ions) beams collide inside four experiments along the beam line:
423 ATLAS, CMS, LHCb, ALICE. ATLAS and CMS are general purpose detectors de-
424 signed to explore the high energy frontier. LHCb is designed to study the physics
425 of b -quarks. ALICE specializes in studying heavy ion collisions.

proton - (anti)proton cross sections

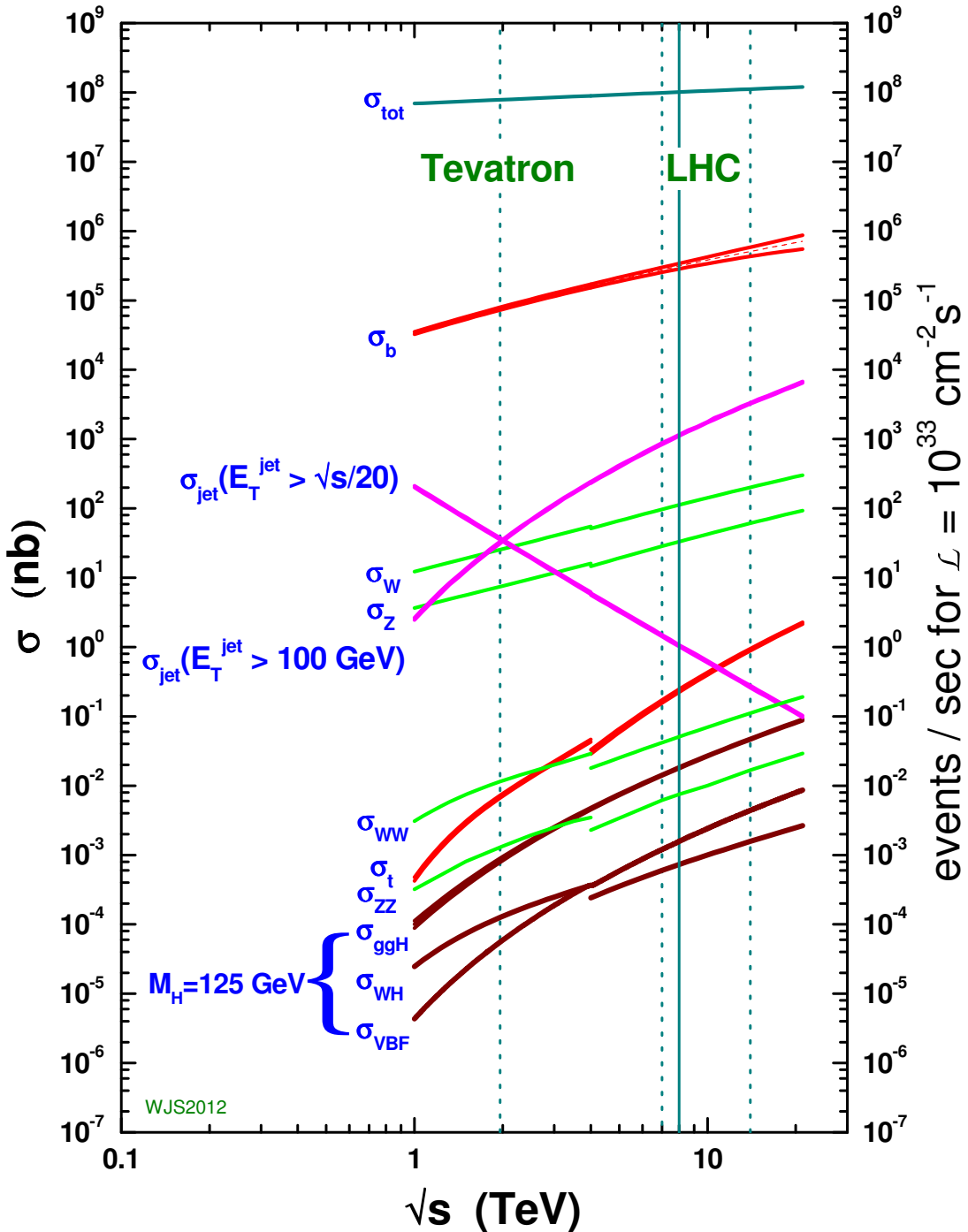


Figure 5.1: Scaling of cross sections with \sqrt{s} . Natasha: write more here

426 The first proton beams circulated in September, 2008. Nine days later an elec-
427 trical fault lead to mechanical damage and liquid helium leaks in the collider. This
428 incident delayed further operation until November 2009, when the LHC became
429 the world's highest energy particle collider, at 1.18TeV per beam. This first oper-
430 ational run continued until 2013, reaching 7 and 8 TeV collision energies. During
431 this run a particle with properties consistent with the Standard Model Higgs bo-
432 son was discovered. The next run began after a two year shutdown after upgrades
433 to the LHC and experiments. This run lasted from 2013 to 2018 reaching 13 TeV
434 collision energies. This analysis uses data from the second operational run.

435 **5.1 LHC Layout and Design**

436 The layout of the LHC is shown in Figure 5.2. The red and blue lines in the
437 figure represent the counter-circulating proton beams. The LHC is divided into
438 eight octants. Octant 4 contains the RF cavities that accelerate the protons and
439 octant 6 contains the beam dump system. Octants 3 and 7 house the collimation
440 systems for beam cleaning. The beams collide inside the four aforementioned
441 experiments. Each octant contains a curved and straight section. The LHC
442 magnets are built with NbTi superconductors cooled with super-fluid Helium to
443 2K, creating a 8.3T magnetic field to bend the proton beams.

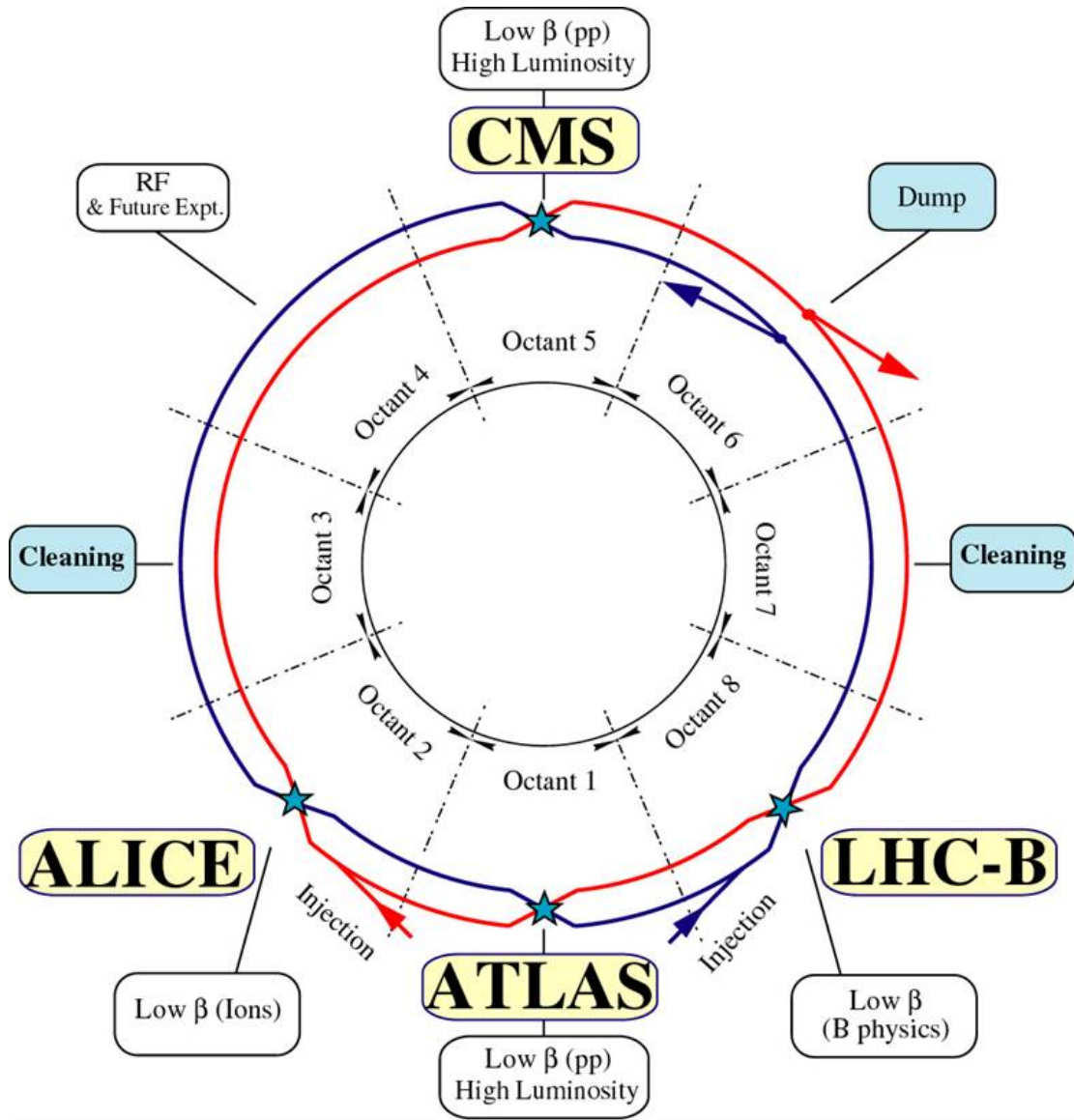
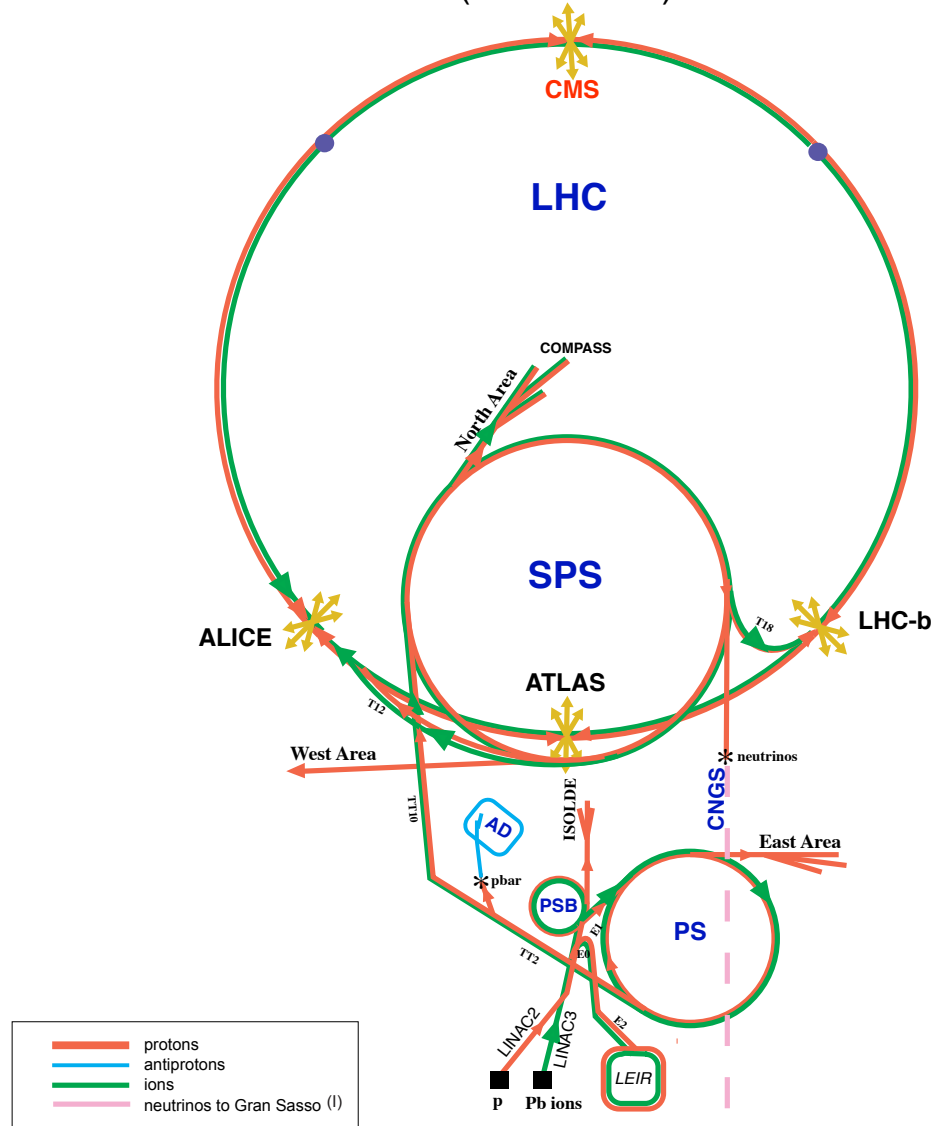


Figure 5.2: LHC Layout. Natasha write more

444 Four sequential particle accelerators are used to accelerate protons from rest
 445 as shown in Figure 5.3. First, Hydrogen gas is ionized to produce protons which
 446 are then accelerated to 50 MeV using Linac 2, a linear accelerator. The result-
 447 ing proton beam is then passed to three circular particle accelerators: Proton
 448 Synchrotron Booster, Proton Synchrotron, and Super Proton Synchrotron (SPS),

449 accelerating protons to 1.4, 25, and 450 GeV, respectively. Once the protons exit
450 the SPS, they are injected into the LHC at octant 2 and 8. Each proton bunch
451 contains $\sim 10^{11}$ protons. The spacing between bunches is 25 ns, which means
452 each beam contains 3564 bunches. However, some bunches are left empty due
453 to injection and safety requirements, yielding 2808 bunches per beam. Once the
454 proton beams are injected they are accelerated to 13 TeV.

CERN Accelerators (not to scale)



LHC: Large Hadron Collider

SPS: Super Proton Synchrotron

AD: Antiproton Decelerator

ISOLDE: Isotope Separator OnLine DEvice

PSB: Proton Synchrotron Booster

PS: Proton Synchrotron

LINAC: LINear ACcelerator

LEIR: Low Energy Ion Ring

CNGS: Cern Neutrinos to Gran Sasso

Rudolf LEY, PS Division, CERN, 02.09.96
Revised and adapted by Antonella Del Rosso, ETT Div.,
in collaboration with B. Desforges, SL Div., and
D. Manglunki, PS Div. CERN, 23.05.01

Figure 5.3: LHC Accelerator. Natasha write more

455 As many new physics models predict cross-sections below the weak scale it was
456 important to design the LHC to be capable of collecting enough data, by running
457 in high luminosity conditions. The machine luminosity depends only on beam
458 parameters:

$$L = \frac{N_p^2 f}{4\epsilon\beta^*} F \quad (5.1)$$

459 where N_p is the number of protons per bunch, f is the bunch crossing frequency,
460 ϵ is the transverse beam emittance, β^* is the amplitude function at the collision
461 point, and F is the geometric luminosity reduction factor due to the beams crossing
462 at an angle (rather than head-on).

463 **Chapter 6**

464 **The ATLAS Detector**

465 The ATLAS detector measures the position, momentum and energy of parti-
466 cles produced in the proton collisions by using magnetic fields, silicon detectors,
467 sampling calorimeters, and gaseous wire detectors. It is located approximately
468 100 m underground at Point-1 around the LHC beam line and weighs 7000 metric
469 tons. The detector is 46 m long, 25 m high, 25 m wide as shown in Figure 6.2.
470 The detector can be divided into three subsystems: the Inner Detector (ID), the
471 Calorimeters, and the Muon Spectrometer (MS). Figure 6.3 shows an overview of
472 how different particles interact in the detector.

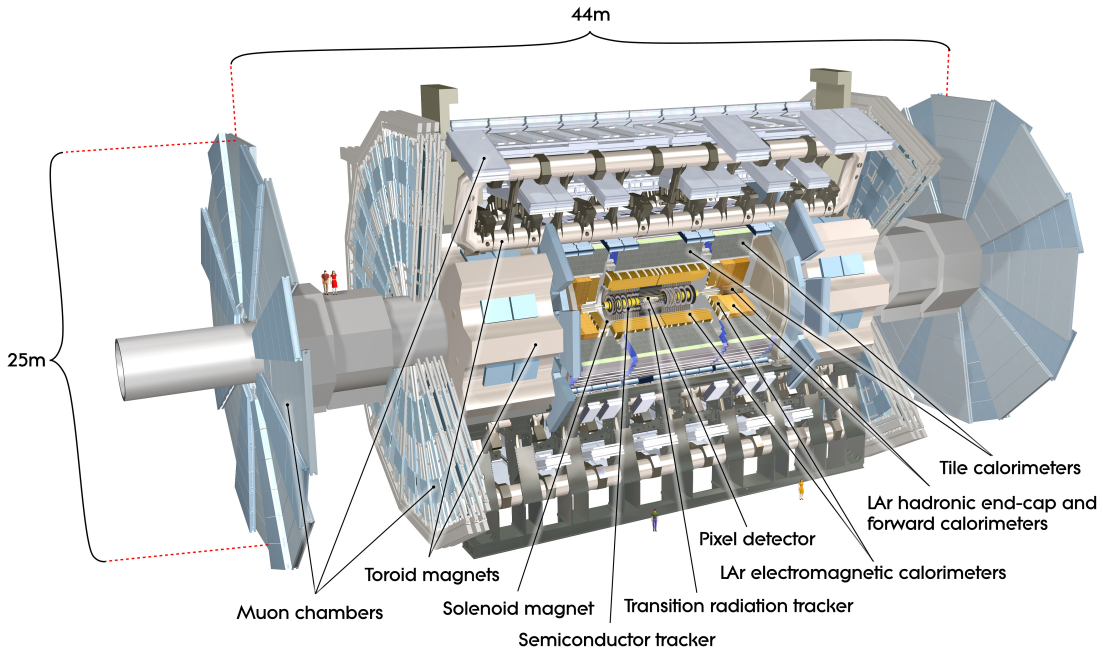


Figure 6.1: Big picture layout of ATLAS detector. Natasha: write more

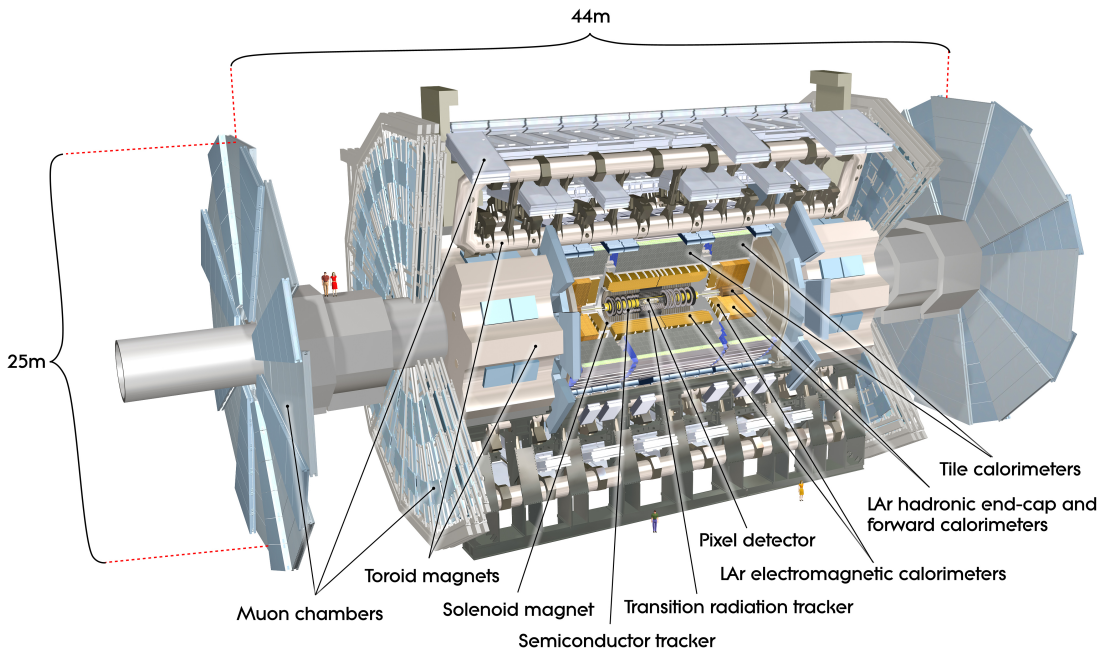


Figure 6.2: Big picture layout of ATLAS detector. Natasha: write more

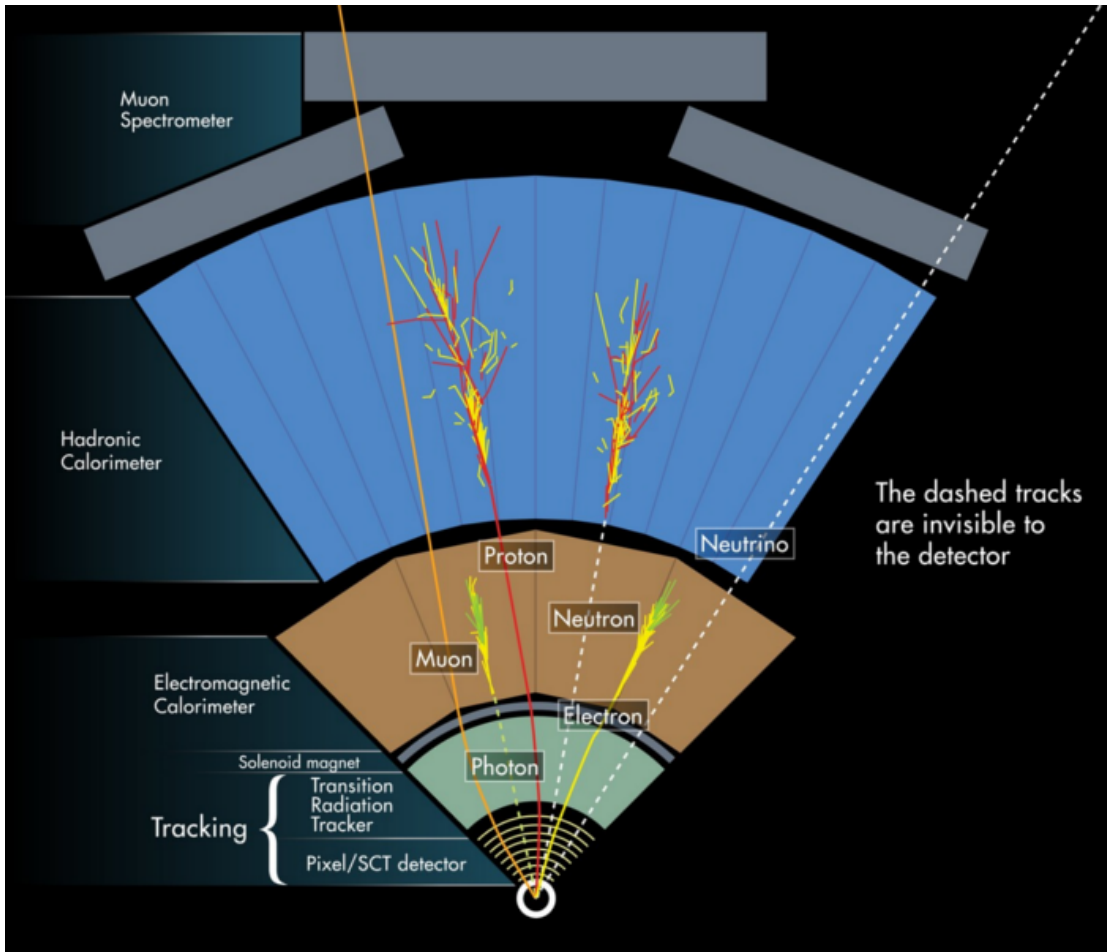


Figure 6.3: A simplified schematic of how different particles interact and are detected within ATLAS.

473 6.1 Coordinate System

474 The trajectory of particles within ATLAS is measured relative to the nominal
 475 interaction point. The z -axis points along the beam line, such that when the
 476 LHC is viewed from above, the counter-clockwise circulating beam points along
 477 the positive- z direction. The $x - y$ plane is transverse to the beam line, with the
 478 positive x -axis pointing towards the center of the LHC ring. The positive y -axis
 479 points vertically upward. The azimuthal angle, ϕ , is the angular distance about

480 the z -axis, with $\phi = 0$ along the x -axis. The polar angle from the z -axis is denoted
481 as θ . However, this quantity is not Lorentz invariant, like rapidity, $y = \frac{1}{2} \ln \frac{E+p_z}{E-p_z}$,
482 where E is the energy of the particle considered, and p_z , is it's momentum along
483 the z -axis. Pseudo-rapidity is preferred as $\Delta\eta$ is invariant under boosts along z
484 and particle production is approximately invariant under η . For massless particles,
485 rapidity and a related quantity, pseudorapidity, are the identical. The pseudora-
486 pidity is defined as: $\eta = -\ln \tan(\frac{\theta}{2})$. This quantity is preferred as it is purely a
487 geometric quantity, independent of particle energy. Angular separation between
488 particles in ATLAS are given by $\Delta R = \sqrt{\Delta\eta^2 + \Delta\phi^2}$. The distance from the
489 beamline is given by $r = \sqrt{x^2 + y^2}$

490 6.2 Inner Detector

491 The Inner Detector (ID) was designed to identify and reconstruct vertices,
492 distinguish pions from electrons, and measure the momentum of charged particles.
493 The ID uses three different technologies for particle reconstruction: the Pixel
494 Detector, Semiconductor Tracker (SCT), and the Transition Radiation Tracker
495 (TRT), shown in Figure 6.4 and 6.5. The entire ID is immersed in a 2T solenoidal
496 magnetic field parallel to the $+z$ -axis, causing charged particles to bend in the
497 transverse-plane, allowing particle momentum measurements.

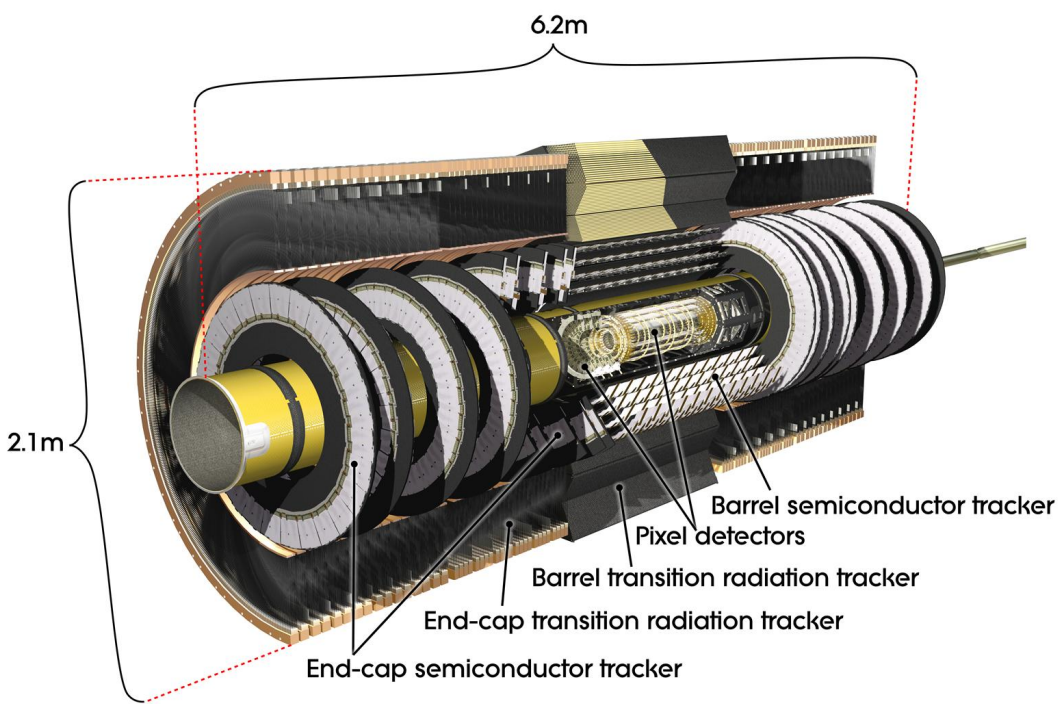


Figure 6.4: Layout of ATLAS Inner Detector

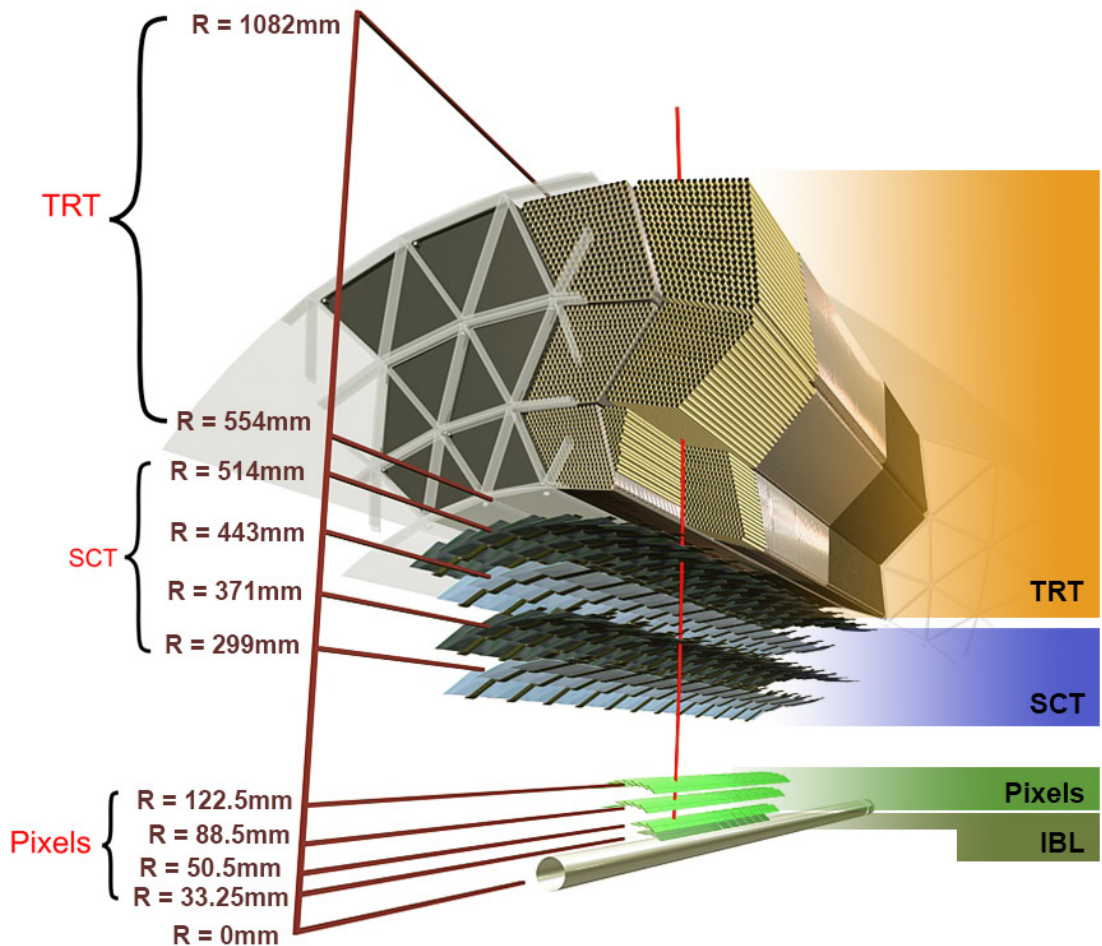


Figure 6.5: Layout of ATLAS ID Barrel System.

498 **6.2.1 Pixel Detector**

499 The pixel detector consists of four barrel layers between $r = 32.7$ and 122.5
500 mm, extending to $|z| = 400.5$ mm. The remaining detectors are arranged in bar-
501 rels and forward and backward rings. The innermost pixel barrel, the Insertable
502 b-Layer (IBL), only extends to $|z| = 332$ mm. The pixel detectors closer to the
503 beam line (larger η values) consists of six parallel cylindrical rings of pixel de-
504 tectors transverse to the beam line. The entire pixel detector consists of 1744
505 identical pixel sensors each with 46080 readout channels, totaling about 80 mil-
506 lion individual pixels. Most of the pixel sensors are $50 \times 400 \mu\text{m}^2$. Each pixel has
507 a position resolution of $14 \mu\text{m}$ in ϕ and $115 \mu\text{m}$ in the z direction.

508 **6.2.2 Semiconductor Tracker**

509 The SCT is located outside the pixel detector and has the same barrel and
510 endcap geometry as the pixel detector. SCT sensors are $80 \mu\text{m} \times 12$ cm with
511 a $80 \mu\text{m}$ strip pitch. In the barrel the strips are parallel to the z -axis and are
512 segmented in ϕ . In the endcaps, the strips extend radially. Sensors are grouped in
513 modules containing two layers of strips rotated 40 mrad with respect to each other.
514 This offset allows for the two-dimensional position of a track to be determined by
515 identifying the crossing point of the strips that registered a hit. SCT modules
516 measure tracks with an accuracy of $17 \mu\text{m}$ in $r - \phi$ and $580 \mu\text{m}$ in $z(r)$ in the
517 barrel (end-cap) region.

518 **6.2.3 Transition Radiation Tracker**

519 The transition radiation tracker (TRT), enveloping the SCT, is a gaseous
520 straw-tube tracker mainly used for electron/pion track separation. Each straw
521 is 4 mm in diameter and filled with a Xe- CO_2 - O_2 gas mixture. An anode wire at

522 the center of the straw is held at ground potential, while the walls of the straw
523 are kept at -1.4kV. When a charged particle passing through the TRT ionizes the
524 gaseous mixture, the resulting ions form an avalanche on the anode wire with a
525 gain of $\sim 10^4$. The signal from the anode wire is then digitized and discriminated.
526 Signals passing a low threshold cutoff are used to distinguish noise from tracks.
527 Signals passing a high threshold cutoff are sensitive to transition radiation (TR).
528 TR photons are emitted when charged particles pass between materials with dif-
529 ferent dielectric constants. The probability that a charged particle with energy E
530 and mass m passing between two materials emits a TR photon in the keV range
531 is proportional to $\gamma = E/m$. In the TRT straws these often then convert via the
532 photoelectric effect, causing a large avalanche triggering the high-threshold. Since
533 electrons have a smaller mass than pions, electron tracks are more likely to trig-
534 ger the high threshold. This then provides discrimination between electrons and
535 charged hadrons.

536 The barrel region of the TRT extends from $r = 563\text{-}1066$ mm and $|z| < 712$
537 mm. Barrel Straws are 144 cm long (divided $\sim \eta \approx 0$) and orientated parallel to
538 the beam direction. End-cap straws extend radially and are 37 cm long. There
539 are 53,544 straws in the barrel and 160,000 straws in the end-caps. Radiator mats
540 of polypropylene/polyethylene fibers in the barrel are aligned perpendicular to the
541 barrel straws (with holes for the straws to pass through). In the end-cap region,
542 radiator foils are layered between the radial TRT straws.

543 The arrival time of the signal pulse is sensitive to the distance between the
544 charged particle track and the anode wire and allows for a hit resolution of $130\mu\text{m}$.
545 The TRT extends to $|\eta| = 2.0$ and provides about 36 hits per track.

546 6.3 Calorimeters

547 The ATLAS electromagnetic and hadronic calorimeters (EMC and HCAL,
548 respectively) absorb and measure the energy of high energy hadrons, photons,
549 and electrons with $|\eta| < 4.9$. Both systems use sampling calorimeters which
550 consist of alternating layers of dense absorbing and active layers. In the absorbing
551 layer particles interact and lose energy, creating showers. These showers are then
552 detected and measured in the active layer. The amount of charge measured in the
553 active material scales with the energy of the incident particle, and thus provides a
554 measurement of the particle's energy. An overview of the layout of the calorimeter
555 system is shown in Figure 6.6.

556 The EMC measures and contains the energy of electromagnetically interacting
557 particles. It consists of layered accordion-shaped Lead absorber plates and elec-
558 trodes immersed in liquid Argon with 170k channels.. Using accordion-shaped
559 electrode and absorbers ensures ϕ symmetry and coverage. The EMC is com-
560 posed of a barrel part ($|\eta| < 1.475$), two end-caps ($1.375 < |\eta| < 3.2$), and a
561 presampler ($|\eta| < 1.8$). The presampler, containing only liquid Argon, corrects
562 for upstream energy losses of electrons and photons. The EMC barrel is segmented
563 into three layers. The first layer has finest segmentation with readout cells ex-
564 tending $\Delta\eta \times \Delta\phi = 0.025/8 \times 0.1$. This provides a precise shower measurements
565 used to separate prompt photons from $\pi^0 \rightarrow \gamma\gamma$ decays. The second layer has
566 coarser segmentation and is approximately 16 radiation lengths long. A radiation
567 length is the average distance an electron travels before losing all but $1/e$ of its
568 energy to bremsstrahlung. The last layer is the most coarse and measures the tail
569 of the electromagnetic shower. A schematic of the ECAL is shown in Figure 6.7.

570 The hadronic calorimeter located outside the EMC and is used to contain
571 and measure the energy of hadronically interacting particles. It consists of a tile

572 calorimeter (TileCal), hadronic end-cap calorimeter (HEC), and liquid Argon for-
 573 ward calorimeter (FCAL). TileCal is located behind the LAr EMC and uses steel
 574 absorbers and liquid Argon as the active material. TileCal consists of three barrel
 575 layers in the central and forward regions, extending up to $|\eta| < 1.7$. Photons
 576 generated from hadronic interactions are collected via wavelength-shifting fibers
 577 connected to photomultiplier tubes, as shown in Figure 6.8. The HEC lies behind
 578 the EMC endcap wheels. It uses copper absorbers and liquid Argon as the active
 579 material and covers $1.5 < |\eta| < 3.2$. Finally, the FCAL covers $3.1 < |\eta| < 4.9$
 580 and consists of three modules all using liquid Argon as the active material. The
 581 first module uses copper absorber and was designed for electromagnetic measure-
 582 ments. The second and third modules consist of tungsten absorber and are used
 583 to measure the kinematics of hadronically interacting particles. A schematic of
 584 the HCAL is shown in Figure 6.8.

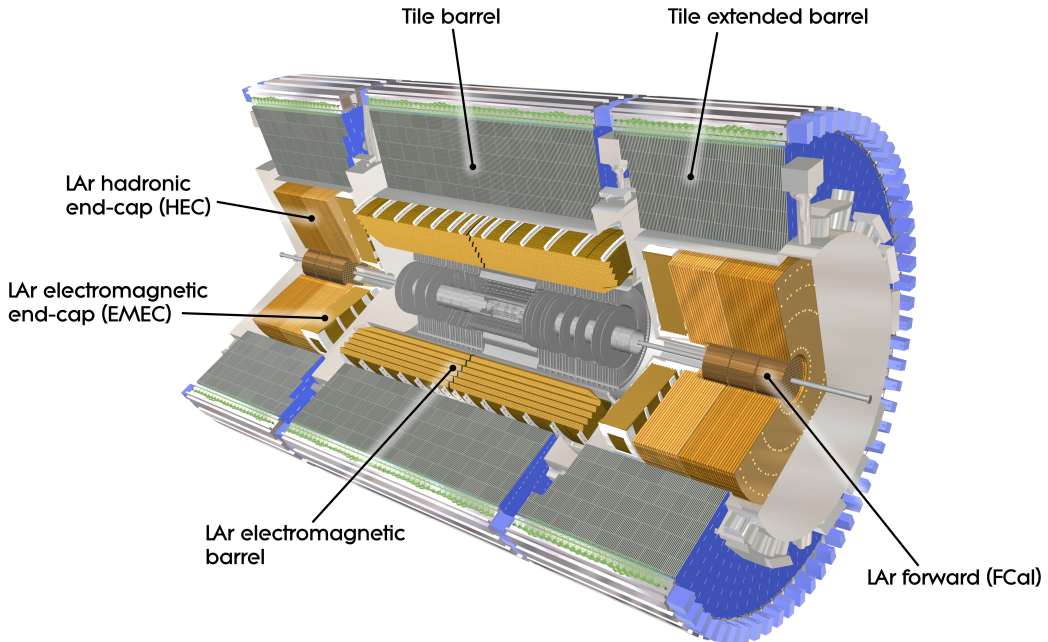


Figure 6.6: Overview of ATLAS electromagnetic and hadronic calorimeters.

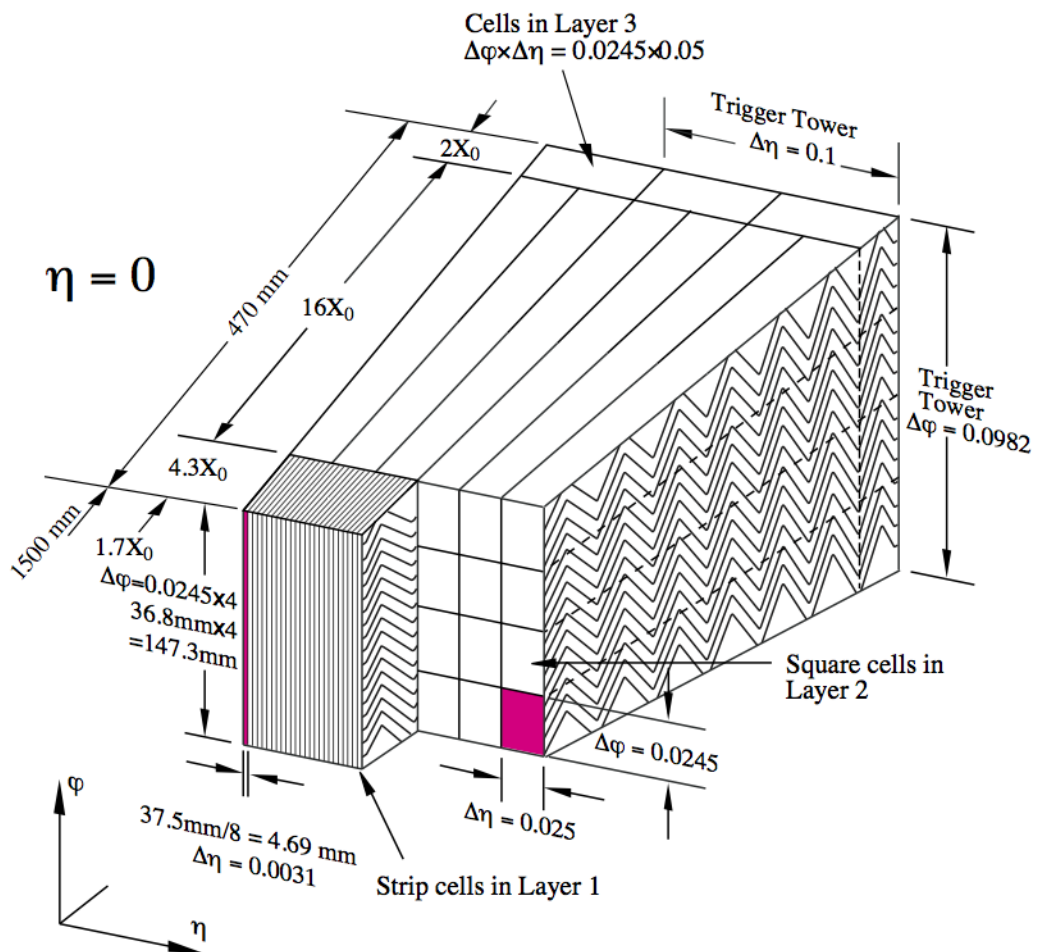


Figure 6.7: Schematic of ECAL.

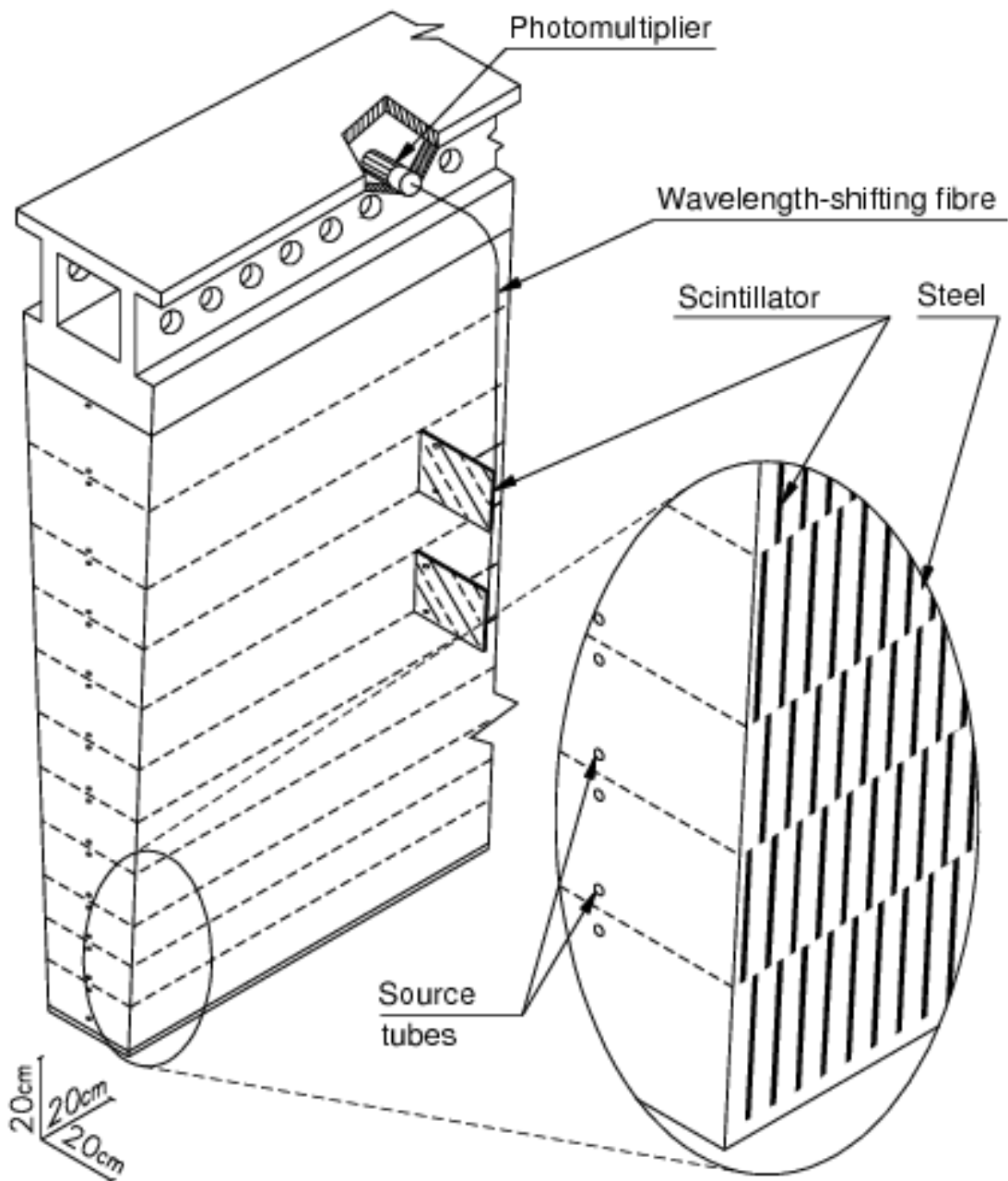


Figure 6.8: Schematic of HCAL.

585 The energy resolution of the calorimeter subsystems are:

586 $\frac{\sigma_E}{E} = \frac{10\%}{\sqrt{E}} \oplus 0.7\% \text{ EMC}$

587 $\frac{\sigma_E}{E} = \frac{50\%}{\sqrt{E}} \oplus 3\% \text{ hadronic barrel}$

588 $\frac{\sigma_E}{E} = \frac{100\%}{\sqrt{E}} \oplus 10\% \text{ hadronic end-cap}$

589

6.4 Muon Spectrometer

590 The muon spectrometer (MS) is the outermost detector system in ATLAS.

591 Muons with a $p_T > 4$ GeV are energetic enough to reach the MS. To measure the
592 momentum of these muons barrel and end-cap toroid magnets are used covering
593 $|\eta| < 1.4$ and $1.6 < |\eta| < 2.7$. For $1.4 < |\eta| < 1.6$, a combination of the barrel
594 and end-cap toroidal magnetic fields bend muon trajectories. The detector in the
595 barrel region form three concentric rings at $R = 5, 7.5, 10$ m and are segmented
596 in ϕ to accommodate the magnets. The end-cap region consists of three circular
597 planes perpendicular to z and located at $|z| = 7.4, 14, 21.5$ m from the interaction
598 region. An additional detector at $|z| = 10.8$ m covers the transition region between
599 the barrel and end-cap.

600 The MS readout consists of four subsystems: Monitored Drift Tubes (MDT),
601 Cathode Strip Chambers (CSC), Resistive Plate Chambers (RPC), and Thin Gap
602 Chambers (TGC). The first two subsystems are used primarily for measuring
603 muon track parameters, while the RPC and TGC subsystems are used for muon
604 triggering. A schematic of this system is shown in Figure 6.9.

605 The MDT subsystem consists of precision tracking chambers for $|\eta| < 2.7$,
606 except for the inner most end-cap layer ($2.0 < |\eta| < 2.7$), where CSCs are used.
607 The basic unit of MDT chambers are thin walled Aluminum tubes with a diameter
608 of 3 cm and length of 0.9-6.2 m. These tubes are filled with a mixture of Ar-CO₂
609 gas with a 50μm W-Rn wire running down the center of the tube, which is kept at

610 3080 V. Since the maximum drift time of these chambers is ~ 700 ns, they are not
611 used for triggering. MDT chambers consist of 3-4 layers of tubes mounted on a
612 rectangular support system, as seen in Figure 6.10, orientated along ϕ to measure
613 the coordinate in the bending plane of the magnetic field with a resolution of 35
614 μm .

615 The MDT subsystem can only handle hit rates below $150\text{Hz}/\text{cm}^2$. For this
616 reason, CSCs are used in the innermost end-cap layer where hit rates are larger.
617 CSCs can handle hit rates up to $1000\text{Hz}/\text{cm}^2$. CSC are multiwire proportional
618 chambers. These chambers are filled with a Ar- CO_2 gas mixture and evenly spaced
619 wires kept at 1900 V. These wires are orientated in the radial direction but not
620 read out. Instead on one side of the cathode are copper strips parallel to the wires,
621 measuring η , while on the other side of the cathode are strips parallel to the wires
622 measuring ϕ . The width between strips is approximately 1.5 mm providing a
623 resolution of 60 μm in the bending-plane and 5 mm in the non-bending plane.

624 Since the CSC and MDT systems do not have prompt timing signals, the RPC
625 and TGC systems are used for triggering. The RPC system is used in the barrel
626 region ($|\eta| < 1.05$). RPC consist of two parallel resistive plates separated by a 2
627 mm insulated spacer with 100 mm spacing kept at 9.8 kV, as shown in Figure 6.11.
628 A gaseous mixture of $\text{C}_2\text{H}_2\text{F}_4$, C_4H_{10} , and SF_6 fills the space between the two
629 plates. Metallic strips on the outer faces of the plates are used to read out signals
630 produced by the gas ionizing. The middle barrel layer consists of two layers of
631 RPCs on either side of the MDT layer and one layer on the outermost MDT
632 layer. Each layer contains two orthogonal sets of metallic strips providing η and
633 ϕ measurements. The timing resolution of RPCs is 1.5 ns, and therefore may be
634 used to identify bunch crossings.

635 Finally, the TGCs are used in the end-cap regions and are primarily used to

636 provide L1 trigger decisions and ϕ measurements. TGCs are multi-wire propor-
 637 tional chambers consisting of arrays of gold-coated tungsten wires placed between
 638 two cathode planes. These wires are separated by 1.8 mm and cathodes are 1.4 mm
 639 from the wires. Orthogonal to the wires, on the opposite side of the cathode plane
 640 are copper strips held at 2900 V. The chambers are filled with a mixture of CO_2
 641 and n-pentane gas, the latter acts as a quenching gas to prevent avalanches initi-
 642 ated by secondary γ -rays from the primary avalanche. Figure 6.12 is a schematic
 643 of a TGC. The timing resolution of TGCs is less than 25 ns and therefore they
 644 are used for bunch crossing measurements.

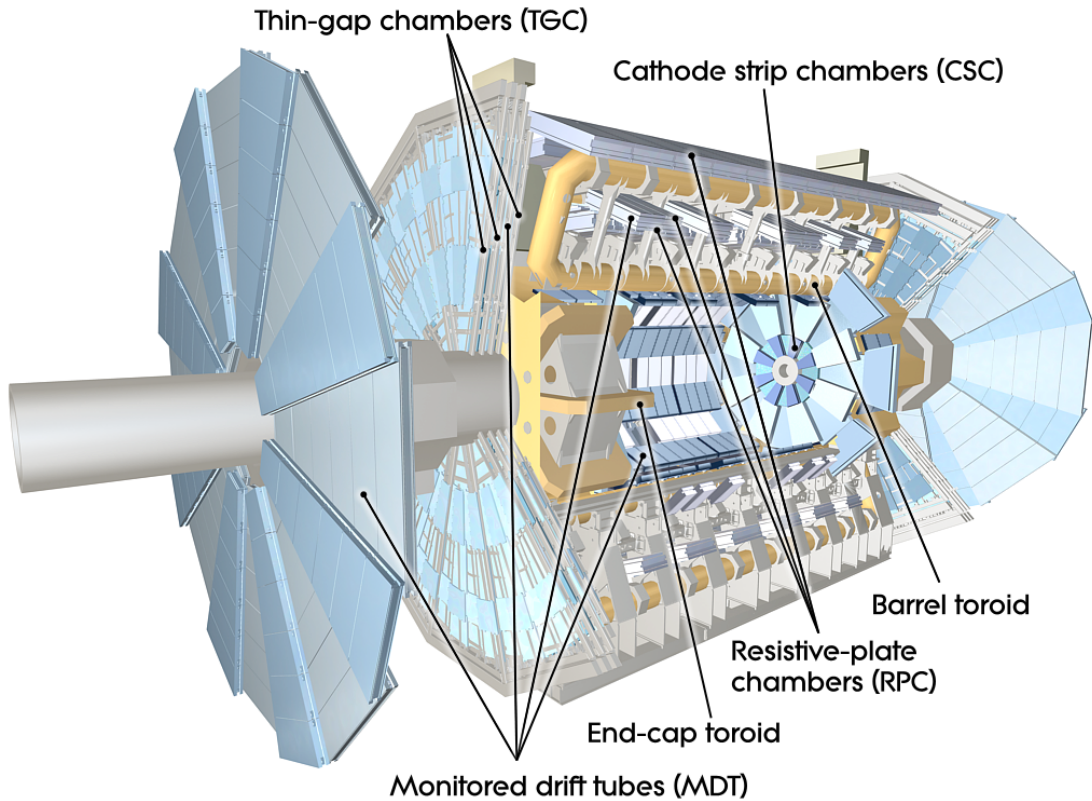


Figure 6.9: Schematic of Muon Spectrometer [cite G35]

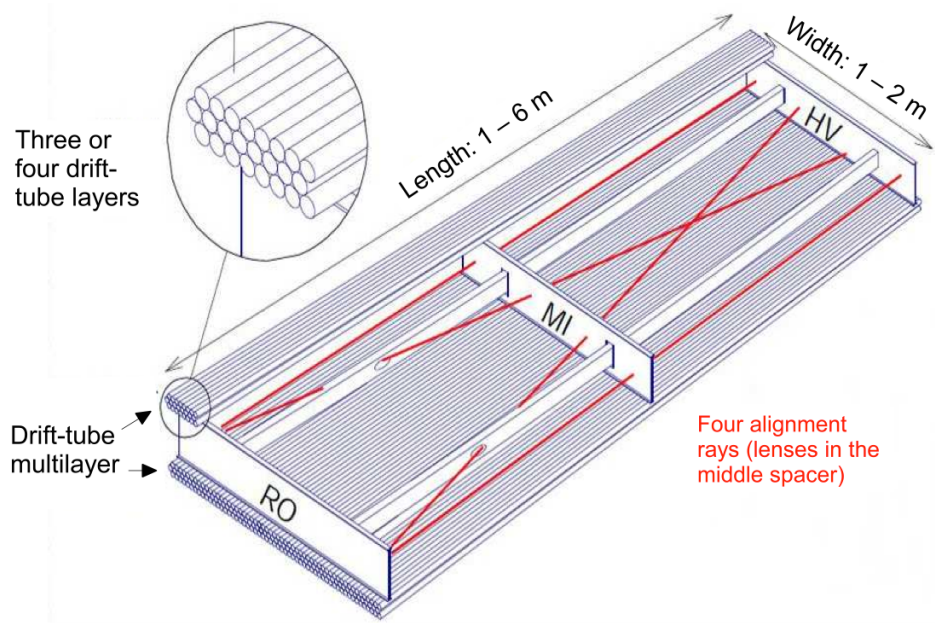


Figure 6.10: Schematic of MDT chamber. [cite G35]

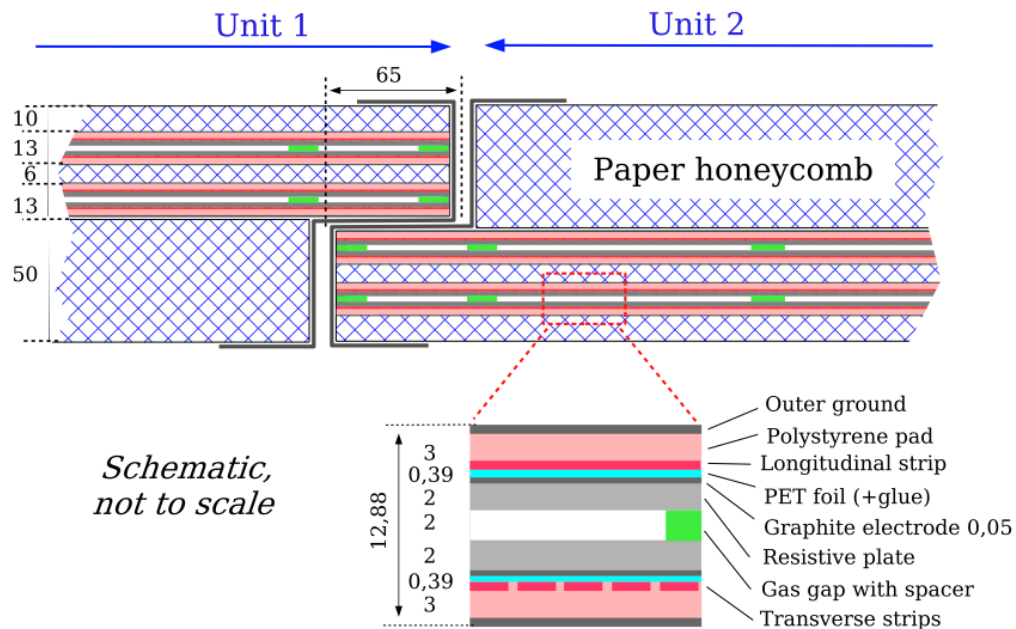


Figure 6.11: Schematic of RPC chamber, which is used for triggering in the central region of the detector [cite G35].

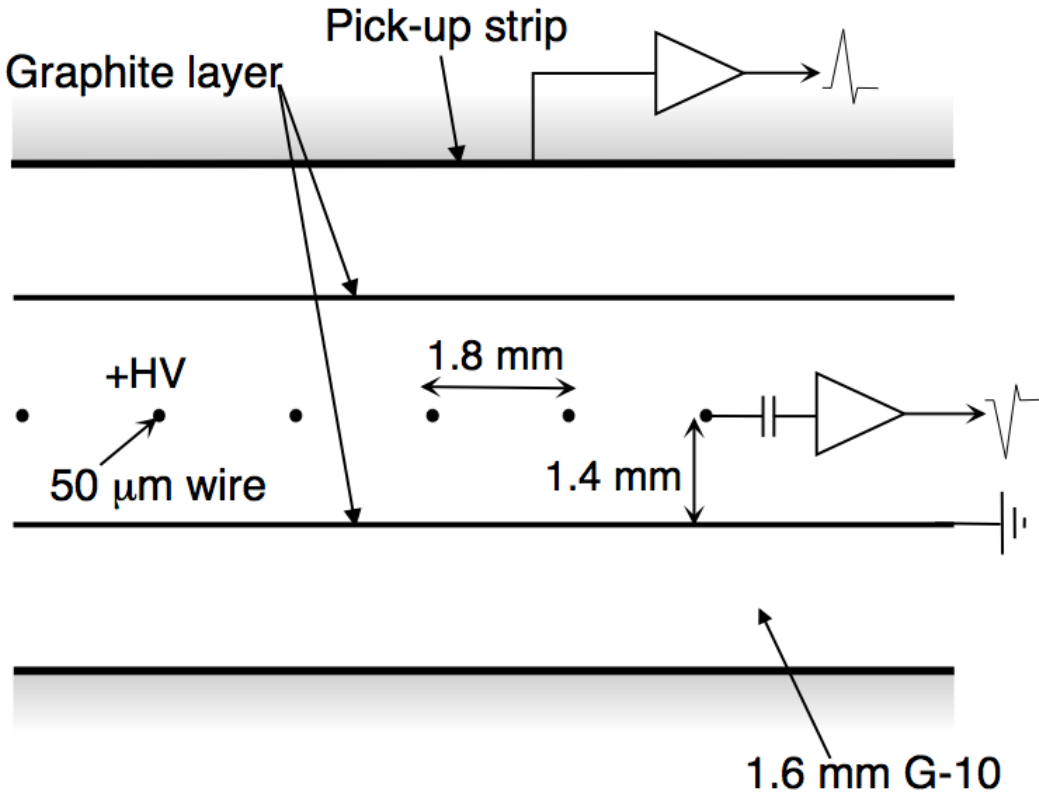


Figure 6.12: Schematic of TGC chamber, which is used for triggering in the muon end-cap region. [cite G35]

645 6.5 Magnet System

646 A particles with charge, q , and velocity v , moving in magnetic field, B , ex-
 647 periences a force, $F = qv \times B$. This force can cause charged particles to have a
 648 curved trajectory in magnetic fields, which the ID and MS use to determine the
 649 particles p_T . The central solenoid provides the magnetic field for the ID and the
 650 toroidal magnets provide the magnetic field for the MS.

651 The layout of the magnet system is shown in Figure 6.13. The central solenoid
 652 consists of a single-layer Al-stabilized NbTi conductor coil wound inside an Al

653 support cylinder. The solenoid is 5.8 m long, 50 cm thick and has an inner radius
654 of 1.23 m. It is cooled to 4.5 K to reach superconducting temperatures and shares
655 the liquid argon calorimeter vacuum vessel to minimize material in the detector.
656 A current of 7.730kA produces a 1.998 T solenoidal magnetic field, pointing in
657 the $+z$ direction.

658 The toroidal magnet system consists of a barrel and two end-cap toroidal
659 magnets used to create a magnetic field outside the calorimeters that is orientated
660 along ϕ . Each barrel toroid is 25.3 m long with an inner and outer diameter of 9.4
661 and 20.1 m and weighs 830 tonnes. Endcap toroids are 5 m long with an inner and
662 outer radius of 1.65 and 10.7 m. Both toroid systems use Al-stabilized Nb/Ti/Cu
663 conductors. The magnetic field strength in the barrel and endcap regions are 0.5
664 and 1 T, respectively.

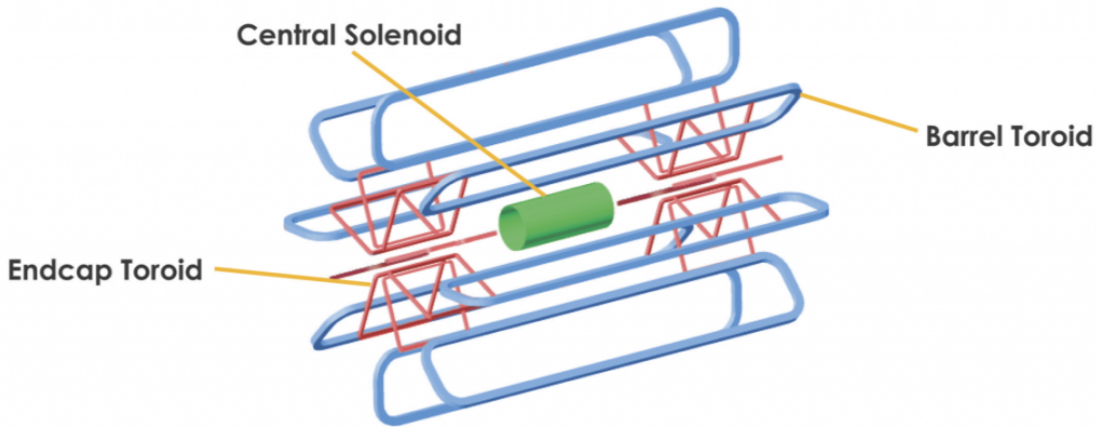


Figure 6.13: Layout of ATLAS magnet systems.

665 **6.6 Trigger System**

666 Since collisions occur every 25 ns and reading out all detector channels and
667 storing that information is not currently feasible (would require saving 60 million
668 megabytes per second), the majority of events are not kept for analysis. ATLAS

669 uses a multi-stage trigger system to select approximately 1,000 of the 1.7 billion
670 collisions that occur each second (corresponding to a rate of 1 kHz from the 40
671 MHz proton collision rate). The first stage of the trigger system is the hardware
672 level (L1) trigger. This trigger reduces the event rate to \sim 100 kHz by identifying
673 Regions-of-Interest (ROIs) containing high p_T leptons, photons, jets, or E_T^{miss} by
674 using information from RPCs, TGCs, and calorimeters to make a $2.5 \mu\text{s}$ decision.
675 This information is then passed to a high-level trigger (HLT) which further de-
676 creases event rates to \sim 1 kHz. The HLT uses finer granularity measurements
677 from the MS and ID to perform simplified offline reconstruction to decide which
678 events to keep.

Part IV

679

Method

680

681 **Chapter 7**

682 **Dataset and Simulated Samples**

683 **7.1 Dataset**

684 This analysis uses pp collision data collected from 2015 to 2018 at $\sqrt{s} = 13$
685 TeV, corresponding to 139/fb of data as shown in Figure 7.1 and 7.2. From this
686 dataset, only those events in which the tracker, calorimeters, and muon spectrom-
687 eter have good data quality are used. For a given event, the solenoid and toroidal
688 magnets must also be operating at their nominal field strengths. In addition to
689 this, events must pass further quality checks to reject events where detector sub-
690 systems may have failed. These selections reject events that containing LAr noise
691 bursts, saturation in the electromagnetic calorimeter, TileCal errors, and failures
692 in event recovery due to tracker failures. Events with information missing from
693 subsystems (usually due to busy detector conditions) are rejected. Events must
694 also contain a primary vertex with at least two associated tracks, where the pri-
695 mary vertex is selected as the vertex with the largest $\sum p_T^2$ over tracks associated
696 with the vertex and $p_T > 0.5$ GeV.

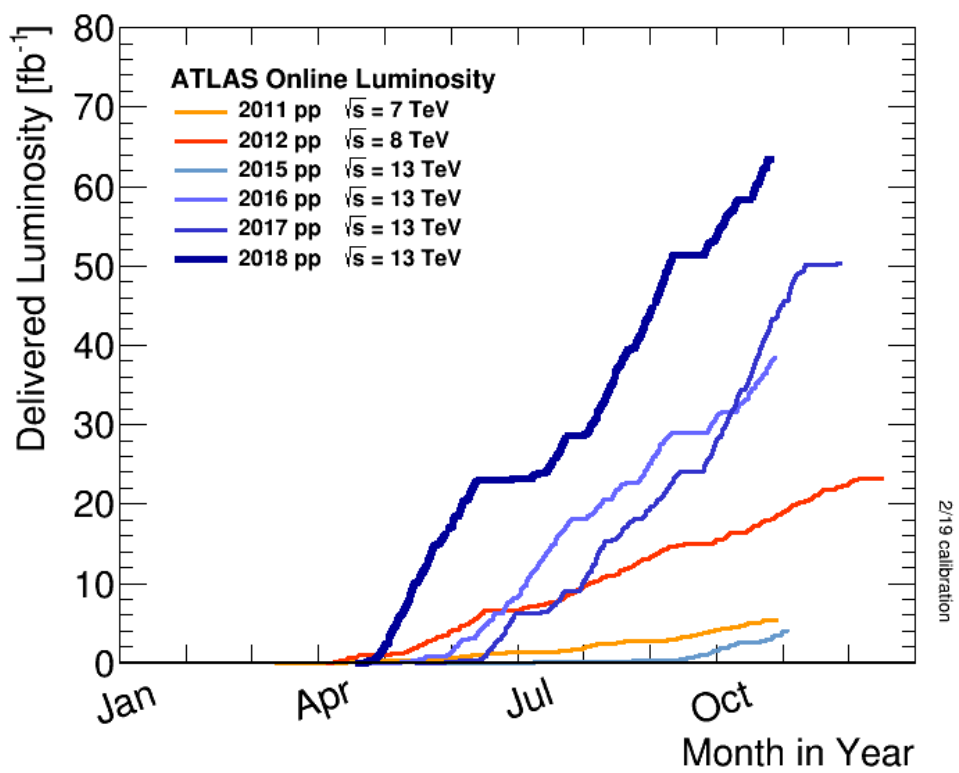


Figure 7.1: Integrated luminosity for data collected from ATLAS from 2011 - 2018

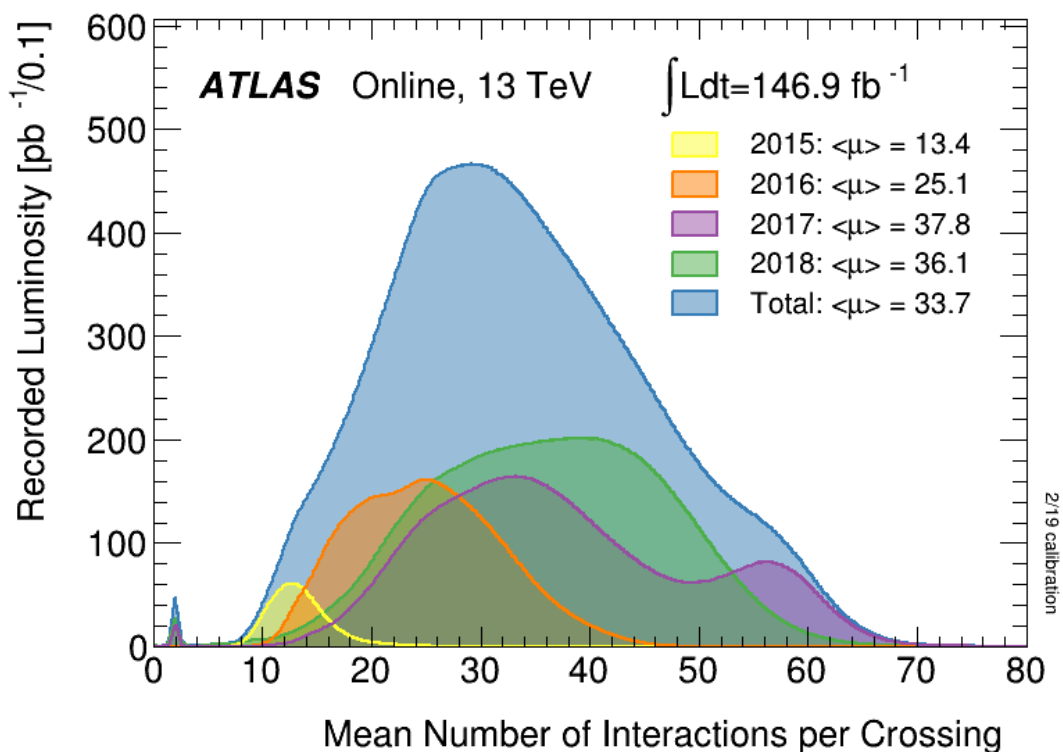


Figure 7.2: Mean number of interactions per crossing for data collected from ATLAS from 2011 - 2018

697 7.2 Simulated Samples

698 Samples are simulated in order to model backgrounds, evaluate signal ac-
699 ceptance, optimize event selection and estimate systematic and statistical uncer-
700 tainties. The dominant backgrounds for this analysis are $W/Z + \text{jets}$, diboson
701 (WZ/WW), $t\bar{t}$, single top and multijet production.

702 $W/Z+\text{jet}$ events are simulated using Sherpa 2.2.1 at NLO [cite [29]] and merged
703 with the Sherpa parton shower using the ME+PS@NLO prescription [12]. These
704 events are then normalized to NNLO cross sections. The $t\bar{t}$ and single-top back-
705 grounds are generated with Powheg-Box with NNPDF3.0NLO PDF sets in the
706 matrix element calculation [cite[35]]. For all processes, the parton shower, frag-
707 mentation, and underlying event are simulated using Pythia 8.320 with the A14
708 tune set[cite[ATL-PHYS-PUB-2014-02]]. Diboson processes are generated using
709 Sherpa 2.2.1.

710 Signal samples are simulated using MadGraph 5-2.2.2 [cite 42] and Pythia
711 8.186 with NNPDF230LO. RS Graviton samples are generated with $k/M_{PL}=1$.
712 HVT Model A (B) samples are simulated with $g_V = 1(3)$, as the difference in the
713 width of the samples is smaller than detector resolution. Model C is generated by
714 setting $g_H = 1$ and $g_f = 0$ to model VBF production of HVT bosons. Signals are
715 generated for masses between 300 GeV and 5 TeV.

716 **Chapter 8**

717 **Objects**

718 **8.1 Electrons**

719 Electrons are reconstructed from electromagnetic showers in the LAr EM
720 calorimeter. During reconstruction cells of $\Delta\eta \times \Delta\phi = 0.025 \times 0.025$ are grouped
721 into 3×5 clusters. These clusters are then scanned for local maxima that seed
722 electron clusters. These clusters must then be matched to ID track from the PV.
723 This requirement minimizes non-prompt electron and fake electron backgrounds.
724 Electrons must pass identification and isolation requirements. Electron identifica-
725 tion (loose, medium, tight) classification is based on a multivariate discriminant
726 that identifies electrons using a likelihood based method. For this analysis, events
727 are required to have one tight electron and no additional loose electrons. Elec-
728 trons are also required to be isolated. The electrons are considered isolated if the
729 quotient of the sum of the transverse momentum (of calorimeter energy deposits)
730 in a cone around the electron of size $\Delta R = 0.2$ and the transverse momentum
731 of the electron to be less than $0.015 * p_T$ or 3.5 GeV, whichever is smaller. This
732 requirement rejects non-prompt photons and other fake leptons. Electrons in this
733 analysis are also required to have $p_T > 30$ GeV and $|\eta| < 2.47$. Electrons are also

734 required to have $p_T > 30$ GeV.

735 Electrons are calibrated to determine data-driven scale factors using $J/\Psi \rightarrow$
736 ee , $Z \rightarrow ee$, $Z \rightarrow \ell\ell\gamma$ processes. These corrections account for the non-uniform
737 response of the detector which introduces modeling and reconstruction uncertain-
738 ties.

739 8.2 Muons

740 As muons traverse the entire detector, they are reconstructed from ID and
741 MS tracks. For this analysis the muon identification and isolation working points
742 are chosen to minimize the contributions from non-prompt muons. Towards this
743 end, each selected event must contain exactly one muon that passes the medium
744 identification working point, and no additional muons (that pass the loose working
745 point). For the medium working point, two types of reconstructed muons are
746 used: combined and extrapolated muons (CB and ME, respectively). For CB
747 muons, ID and MS tracks are reconstructed independently and a combined track
748 fit is performed by adding or removing MS tracks to improve the fit quality.
749 ME muons are reconstructed from only MS tracks with hits in at least two layers,
750 which ensures the track originates from the PV. ME muons extend the acceptance
751 for muon reconstruction outside the ID from $2.5 < |\eta| < 2.7$. The medium
752 identification working point uses CB and ME tracks. CB tracks must have at
753 least 3 hits in two MDT layers. ME tracks are required to have at least three
754 MDT/CSC hits. To further minimize contributions from fake muons, the selected
755 muons are required to be isolated from other tracks, as muons from W, Z decays are
756 often isolated from other particles. To insure the selected muons are isolated, the
757 scalar sum of the transverse momentum of tracks in a cone of $\Delta R = 0.3$ compared
758 to the transverse momentum of the muon must be less than 0.06. Muons are also

759 required to have $p_T > 30$ GeV.

760 Muons are calibrated using well-studied resonances $J/\Psi \rightarrow \mu\mu$ (low- p_T), $Z \rightarrow$
761 $\mu\mu$ (high- p_T). Figure 8.1 shows the combined muon p_T uncertainty from this
762 calibration. The total systematic uncertainty is less than 1% for all p_T ranges
763 considered in this analysis.

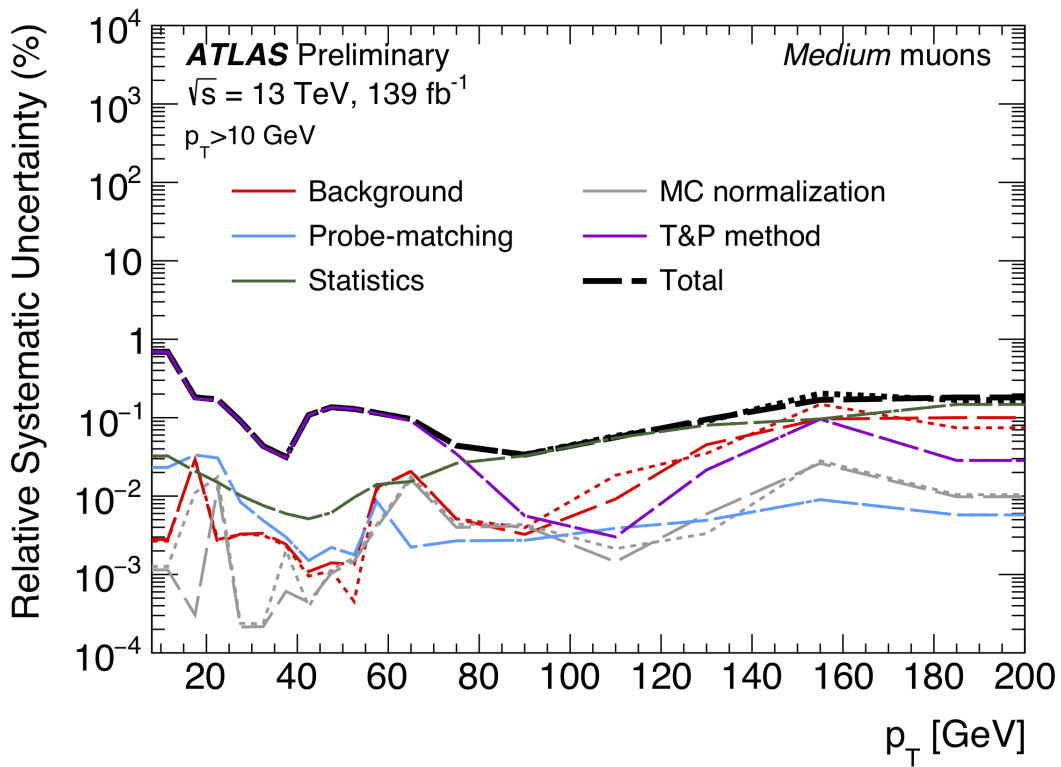


Figure 8.1: This figure shows the breakdown of the muon reconstruction efficiency scale factor measured in $Z \rightarrow \mu\mu$ as a function of p_T [4].

764 8.3 Jets

765 Three types of jets are used in this analysis: variable radius, small-R and
766 large-R jets. Variable radius jets are used to reconstruct Z bosons decaying to
767 two b -jets in the jet catchment area of large-R jet in the Merged regime. Small-R

768 jets are used to reconstruct the hadronically decaying W/Z candidates in the
769 resolved analysis and the forward jets from resonances produced through vector
770 boson fusion. Large-R jets are used to reconstruct the hadronically decaying boson
771 in the merged regime.

772 For all of these jet collections, the jet energy is calibrated sequentially as shown
773 in Figure 8.2. After the jet direction is corrected to point to the PV, the energy
774 of the jet is corrected. First, the jet energy is corrected to account for pileup
775 contributions based on the p_T and area of the jet (these corrections are extracted
776 from a $pp \rightarrow jj$ sample). Following this, another pileup correction is applied that
777 scales with μ and N_{PV} .

778 MC-based corrections are then applied that are meant to transform the jet
779 energy and η back to truth level. Therefore, these corrections account for the
780 non-compensating nature of the ATLAS calorimeters and inhomogeneity of the
781 detector. Following this, the Global Sequential Calibration is applied that re-
782 duces flavor dependence of jet calibrations and accounts for energy leakage of jets
783 outside the calorimeters. Finally, in-situ corrections are applied that account for
784 differences in jet responses between data and simulation ($\gamma/Z + \text{jet}$ and fake lep-
785 ton samples are used). These differences can be due to mismodelling of the hard
786 scatter event, pile-up, jet formation, etc.

787 To further reject fake jets, jets must pass quality requirements based on the
788 following variables ([cite P42]):

- 789 - f_Q^{LAr} : fraction of energy of jet's LAr cells with poor signal shape
- 790 - f_Q^{HEC} : fraction of energy of jet's HEC cells with poor signal shape
- 791 - E_{neg} : sum of cells with negative energy
- 792 - f_{EM} : fraction of jet's energy deposited in EM calorimeter

- 793 - f_{HEC} : fraction of jet's energy deposited in HEC calorimeter
- 794 - f_{max} : maximum energy fraction in any single calorimeter layer
- 795 - f_{ch} : ratio of the scalar sum of the p_T of a jet's charged tracks to the jet's p_T
- 796 Jets selected for the resolved analysis must pass one of the following criteria:
- 797 - $f_{HEC} > 0.5$ and $|f_Q^{HEC}| > 0.5$ and $\langle Q \rangle > 0.8$
- 798 - $|E_{neg}| > 60$ GeV
- 799 - $f_{EM} > 0.95$ and $f_Q^{LAr} > 0.8$ and $\langle Q \rangle > 0.8$ and $|\eta| < 2.8$
- 800 - $f_{max} > 0.99$ and $|\eta| < 2$
- 801 - $f_{EM} < 0.05$ and $f_{ch} < 0.05$ and $|\eta| < 2$
- 802 - $f_{EM} < 0.05$ and $|\eta| > 2$

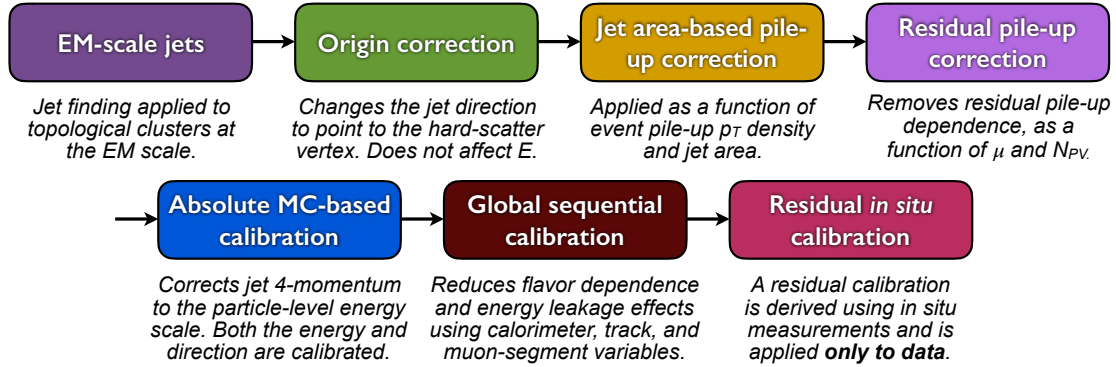


Figure 8.2: [7] This diagram shows the calibration stages for EM jets.

803 **8.3.1 Small-R jets**

804 Small-R jets are used to reconstruct the hadronically decaying W/Z candi-
805 date when the two resulting jets are well-separated in $\eta\text{-}\phi$ space. Small-R jets
806 are also used to identify forward jets from resonances produced through vector
807 boson fusion. Small-R jets are constructed from topologically connected clusters
808 of calorimeter cells (topoclusters), seeded from calorimeter cells with energy de-
809 posits significantly above the noise threshold. These cells are then used as inputs
810 to the $anti-k_t$ algorithm [15] with a radius parameter, $R = 0.4$.

811 Jets used in this analysis must have $p_T > 30$ GeV and $|\eta| < 2.5$. To further
812 reduce fake jets the jet-vertex-tagger (JVT) is used to reject pile-up jets [6]. The
813 JVT uses two track-based variables, corrJVF and R_{p_T} to calculate the likelihood
814 that the jet originated from the PV. The corrJVF compares the scalar sum of the
815 p_T of tracks associated with the jet and PV to the scalar sum of the p_T of tracks
816 associated with the jet. This variable also includes a correction that reduces the
817 dependency of corrJVF with the number of reconstructed vertices in the event.
818 The other discriminant, R_{p_T} , is given by the ratio of the scalar sum of the p_T of
819 tracks associated with the jet and PV to the p_T of the jet. Both of these variables
820 peak around zero for pileup jets, as these jets are unlikely to have tracks associated
821 with the PV. JVT cuts are applied to all jets with $p_T > 120$ GeV. Central jets
822 ($|\eta| < 2.4$) are required to have a $JVT > 0.59$ and forward jets ($2.4 < |\eta| < 2.5$)
823 are required to have $JVT > 0.11$.

824 **8.3.2 Large-R jets**

825 Large-R ($R = 1.0$) jets are used to reconstruct the hadronically decaying W/Z
826 candidate when the resulting jets are not well-separated in $\eta\text{-}\phi$ space, and overlap
827 forming one large-R jet. Track-Calorimeter Clusters (TCCs) are used to reconstruct these

jets [cite ANA 50]. These jets are constructed using a pseudo particle flow method
 using ID tracks matched to calorimeter clusters. The angular resolution of the
 calorimeter degrades sharply with jet p_T , but the jet energy resolution improves.
 The tracker has excellent angular resolution which improves with p_T . Therefore,
 by matching tracks to jets, TCCs have more precise energy and angular resolution
 than jets constructed from calorimeter information only. These jets are required
 to have $p_T > 200$ GeV, $|\eta| < 2.0$ and $m_J > 50$ GeV.

TCC jets are trimmed as detailed in [cite ANA 45], which suppresses pileup
 and soft radiation in the jet, the jet mass is calculated as the four-vector sum
 of the jet's constituents (assuming massless constituents). The jet mass peaks
 around the W/Z boson mass for $W/Z \rightarrow qq$ jets, and more broadly for quark and
 gluon induced jets.

These jets are then tagged as W jet if it passes optimized jet mass and D_2
 cuts for W bosons, and a Z jet if it passes the optimized cuts for the Z boson.
 The jet substructure variable D_2 is given by the ratio of energy correlation func-
 tions. These fuctions are derived from the energies and pair-wise angles of a jet's
 constituents [cite ANA 46, 47]:

$$D_2^{\beta=1} = E_{CF3} \left(\frac{E_{CF1}}{E_{CF2}} \right)^3 \quad (8.1)$$

Where the energy correlation functions are defined as:

$$E_{CF1} = \sum_i p_{T,i} \quad (8.2)$$

$$E_{CF2} = \sum_{ij} p_{T,i} p_{T,j} \Delta R_{ij} \quad (8.3)$$

$$E_{CF3} = \sum_{ijk} p_{T,i} p_{T,j} p_{T,k} \Delta R_{ij} \Delta R_{jk} \Delta R_{ki} \quad (8.4)$$

848 A two-dimensional optimization of the jet mass and D_2 thresholds was per-
 849 formed to provide maximum sensitivity for this analysis. This optimization was
 850 done by maximizing the signal sensitivity (using HVT W' and G_{KK} samples)
 851 against the single quark and gluon jet backgrounds in bins of jet p_T . Figure 8.3
 852 shows the optimized thresholds on D_2 and jet mass as a function of jet p_T . Figure
 853 8.4 shows the efficiency of the optimized W/Z taggers as a function of jet p_T .

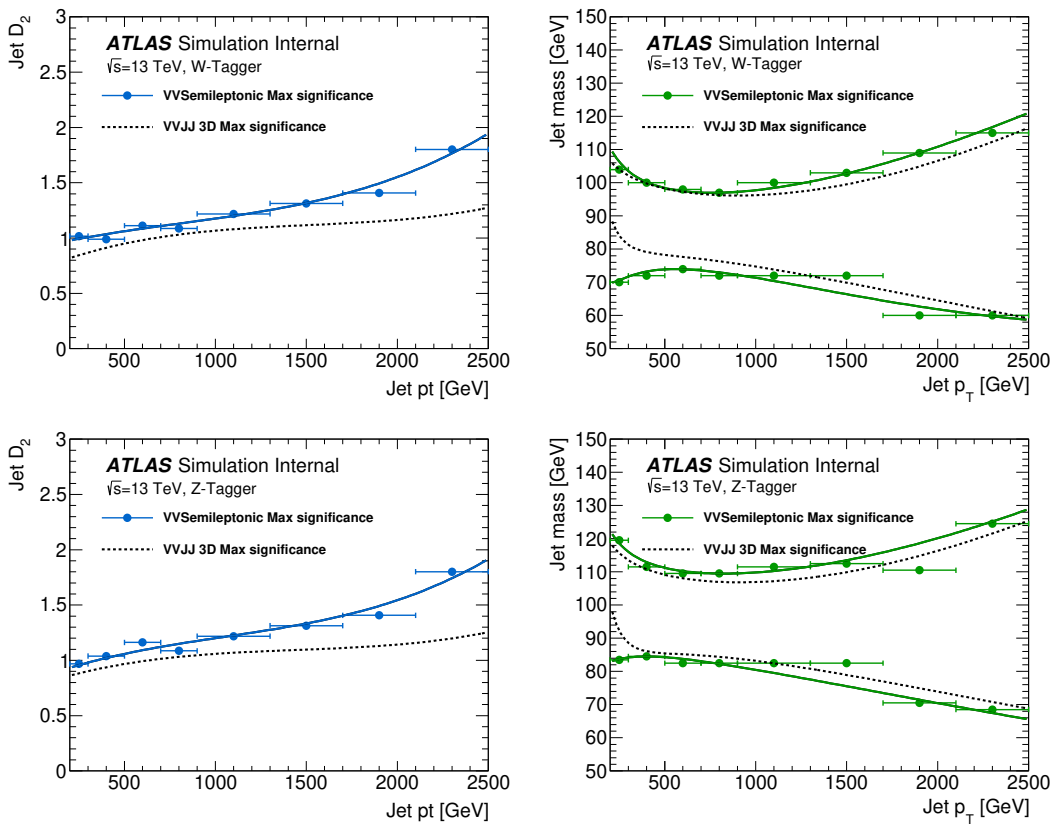


Figure 8.3: The upper cut on D_2 (a) and jet mass window cut i.e. the upper and lower boundary of the mass (b) of the W -tagger as a function of jet p_T . Corresponding values for Z -tagger are shown in (c) and (d). The optimal cut values for maximum significance are shown as solid markers and the fitted function as solid lines. Working points from $VV \rightarrow JJ$ [ATLAS-HDBS-2018-31-002] is also shown as dashed lines as a reference. Natasha reword?

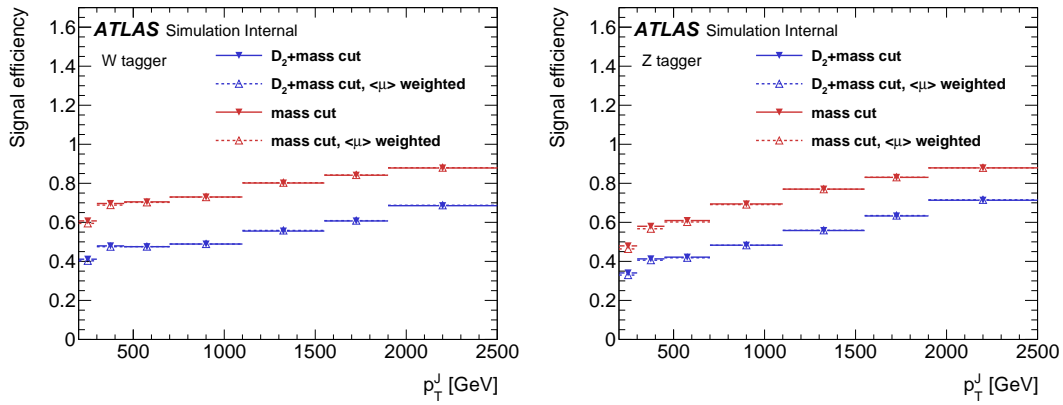


Figure 8.4: Natasha write caption

854 8.3.3 Variable Radius jets

855 To more accept more boosted Z bosons decaying to $b\bar{b}$ that would normally be
 856 rejected due to topological cuts discussed ?? variable radius (VR) track jets are
 857 used to identify b -jets within the catchment area of large- R jets [14]. VR jets are
 858 constructed from ID tracks using the anti- k_t algorithm with a radius parameter
 859 that depends on the p_T of the track, shown in Equation 8.5.

$$R_{eff}(p_{T,i}) = \frac{\rho}{p_{T,i}} \quad (8.5)$$

860 For this search $\rho = 30$ GeV and an upper and lower limit on cone size are set
 861 to 0.02 and 0.4, respectively, to prevent unphysical asymptotic behavior of ρ .
 862 Collinear VR jets are possible, so track jets that are not separated by the the
 863 smaller jet's cone size are not used. Additionally, VR jets are required to have
 864 $p_T > 10$ GeV and $|\eta| < 2.5$.

865 **8.3.4 Jet Flavor Tagging**

866 To further classify events, the small-R and VR jets originating from a b-quark
867 are classified using a multivariate b -tagging algorithm (BDT), MV2c10 [cite G 210
868 199]. This algorithm uses the impact parameters of the jet's ID tracks, secondary
869 vertices (if they exist), and reconstructed flight paths of b and c hadrons in the
870 jet to determine if the jet was induced by a b -quark. For this analysis the 85%
871 efficient working point of this algorithm is used giving c , τ , and light-flavor jet
872 rejection of 3, 8, and 34 respectively in simulated $t\bar{t}$ samples.

873 **8.4 MET/Neutrinos**

874 As neutrinos are uncharged and colorless they do not leave tracks or jets in the
875 detector. For this reason, neutrinos are reconstructed calculated the E_T^{miss} , the
876 negative vector sum of p_T all the physics objects and an extra "soft" term. The
877 "soft" term accounts for energy deposits not associated with any of the objects in
878 the event. For this analysis the soft term is given by the sum p_T of all ID tracks
879 not associated with objects in the event. The selected tracks must be matched to
880 the primary vertex, which decreases pile-up contamination [cite G 217 218]. The
881 tight working point is used [Natasha look up what this means].

882 **8.5 Overlap Removal**

883 Reconstructed jets and leptons in this analysis can arise from the same energy
884 deposits. For instance, a cluster of energy from an electron can also be a valid
885 calorimeter seed for a jet. To mitigate this confusion of multiple objects originating
886 from a single jet or lepton overlapping objects are removed via a procedure referred
887 to a overlap removal. In this procedure the separation of the two objects, $\Delta(R) =$

888 $\sqrt{(\Delta\eta)^2 + (\Delta\phi)^2}$ determines which object is removed from the event.

889 The overlap selections used in this analysis are:

890 - when an electron shares a track with another electron with the lower p_T
891 electron is rejected, as it is more likely to be a fake electron

892 - when a muon and electron share a track the muon is rejected if it is a
893 calo-muon, otherwise the electron is rejected

894 - when $\Delta R < 0.2$ for an electron and jet, the jet is rejected to maximize signal
895 acceptance

896 - when $\Delta R > 0.2$ for an electron and jet, the electron is rejected as likely
897 originated from decays within the jet

898 - when $\Delta R < \min(0.4, 0.04 + 10\text{GeV}/p_T^\mu)$ the muon is rejected, again maximiz-
899 ing signal acceptance, otherwise the jet is rejected

900 - when $\Delta R < 1.0$ for the a large-R jet and electron, the jet is rejected

901 **Chapter 9**

902 **Event Selection and**

903 **Categorization**

904 **9.1 Pre-selection**

905 Before applying topological cuts to suppress backgrounds and reduce data
906 size in this search, preselection cuts are applied which include trigger and event
907 requirements. Events must contain exactly one tight lepton (no additional loose
908 leptons), the $p_T^{\ell\nu} > 75$ GeV, and there must be at least two small-R jets or one
909 large-R jet.

910 **9.2 Trigger**

911 The data were collected using the lowest unprescaled single-lepton or E_T^{miss}
912 triggers, as summarized in Table 9.1. Since the muon term is not considered in the
913 trigger E_T^{miss} calculation, the E_T^{miss} trigger is fully efficient to events with high- p_T
914 muons. For this reason, the E_T^{miss} trigger is used for events where $p_T^\mu > 150$ GeV, to
915 compensate for the poor efficiency of the single muon trigger above $p_T^\mu > 150$ GeV.

ζ

Table 9.1: The list of triggers used in the analysis.

Data-taking period	$e\nu qq$ channel	$\mu\nu qq$ ($p_T(\mu\nu) < 150$ GeV) channel	$\mu\nu qq$ ($p_T(\mu\nu) > 150$ GeV) channel
2015	HLT_e24_lhmedium_L1EM20 OR HLT_e60_lhmedium OR HLT_e120_lhloose	HLT_mu20_iloose_L1MU15 OR HLT_mu50	HLT_xe70
2016a (run < 302919) $(L < 1.0 \times 10^{34} \text{ cm}^{-2} \text{ s}^{-1})$	HLT_e26_lhtight_nod0_ivarloose OR HLT_e60_lhmedium_nod0 OR HLT_e140_lhloose_nod0 HLT_e300_etcut	HLT_mu26_ivarmedium OR HLT_mu50	HLT_xe90_mht_L1XE50
2016b (run ≥ 302919) $(L < 1.7 \times 10^{34} \text{ cm}^{-2} \text{ s}^{-1})$	same as above	same as above	HLT_xe110_mht_L1XE50
2017	same as above	same as above	HLT_xe110_pufit_L1XE55
2018	same as above	same as above	HLT_xe110_pufit_xe70_L1XE50

916 9.3 non-VBF/VBF RNN

917 To classify events as originating from non-VBF or VBF production a recursive
918 neural network (RNN [21]) is used. This approach is more powerful than a cut-
919 based classification as it improves signal efficiency and analysis sensitivity by
920 exploiting correlations between variables that the RNN learns. In particular, a
921 RNN architecture is ideal as it can handle variable numbers of jets in the events.

922 The RNN uses the four-momentum of candidate VBF jets to classify events
923 as VBF or non-VBF topologies. Sometimes jets are incorrectly reconstructed,
924 so the number of jets in the event is expected to vary across the input samples.
925 VBF candidate jets are identified by removing jets from the event that are likely
926 from $W/Z \rightarrow qq$. For the resolved regime this means removing the two leading
927 small-R jets from the VBF candidate jet list. For the merged regime this means
928 removing small-R jets separated by less than 1.0 in dR from the large-R jet. VBF
929 candidate jets are also required to be within $|\eta| < 4.5$. From the list of remaining
930 VBF candidate jets, the two highest- p_T jets are chosen.

931 The architecture of the RNN is shown in Figure 9.2. The RNN is composed
932 of Long Short Term Memory Cells (LSTM) that extract meaningful information
933 and retains³ it. The logic embedded in the LSTM is shown in Figure ???. LSTMs
934 are useful for VBF event classification for events with two jets, where using the
935 kinematic properties of both jets (and their correlations) will lead to more efficient
936 event classification.

937 In this RNN architecture, the VBF candidates are first passed to a masking
938 layer which checks the number of jets in the event. If there is only one jet, only one
939 vertical LSTM layer is used. The output of masking is then passed to a LSTM,
940 with a tanh activation function. The output of the LSTM is then passed to a
941 second horizontal LSTM layer (and vertical LSTM layer if there are two jets in

942 the event). Finally the output of the last LSTM cell is passed to a dense layer
943 and then to a sigmoid activation layer, leading to an overall RNN score.

944 The weights and other parameters of the network are learned by training the
945 network with VBF and non-VBF signals over 200 epochs with an Adam Optimizer
946 [13]. To prevent overfitting during training, dropout is applied to RNN weights
947 and training is truncated if the network parameters are unchanged after ten it-
948 erations [23]. Figure 9.4 shows the ROC curve for the RNN using k-fold cross
949 validation [19].

950 Figure 9.3 shows the RNN discriminant for backgrounds, non-VBF signals,
951 and VBF signals. The RNN score is ~ 0 for non-VBF signals and background
952 processes and ~ 1 for VBF processes. Figure 9.5 shows the limits for various signal
953 processes based on the RNN cut applied. Requiring the RNN score to be > 0.8
954 was chosen as it provided the best significance (and signal efficiency) for this final
955 state and the $\nu\nu qq$ and $\ell\ell qq$ channels, which this channel will be combined with
956 for future publications.

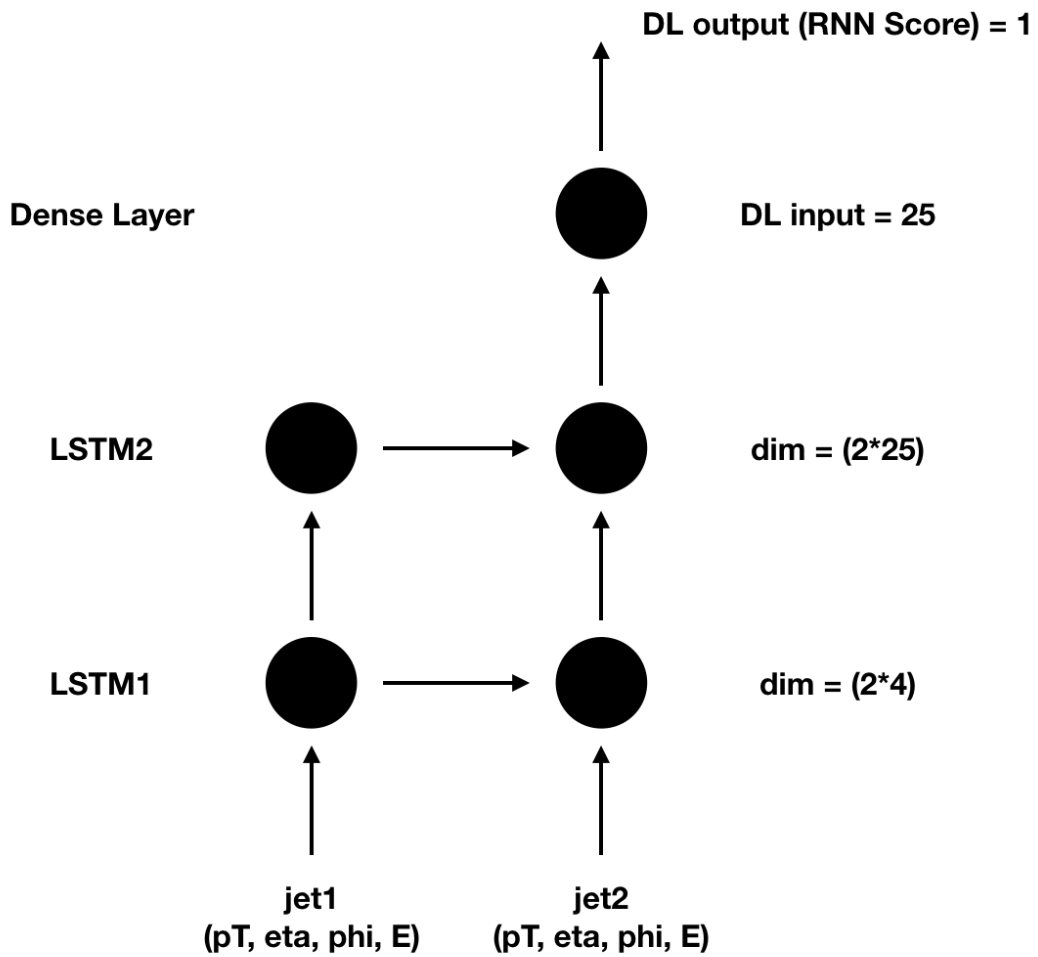


Figure 9.1: RNN architecture. Natasha add caption

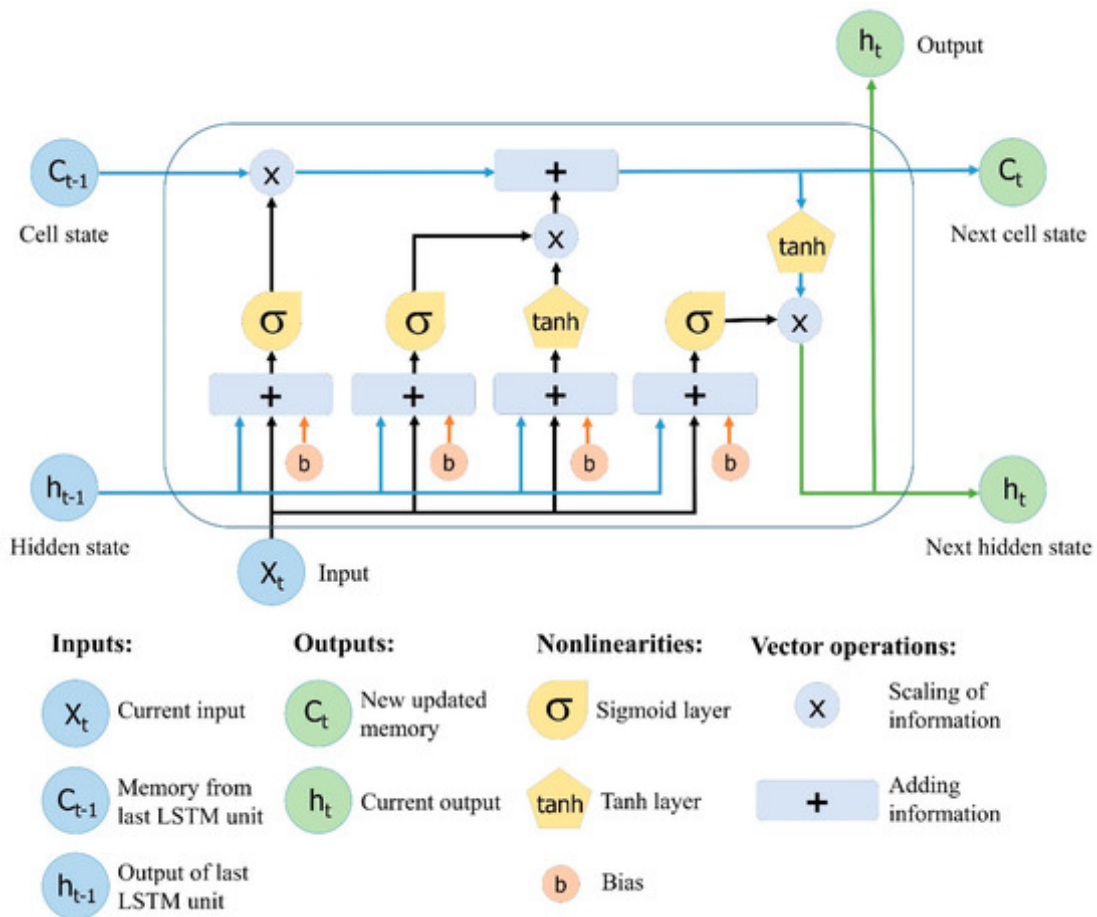


Figure 9.2: This figure shows the embedded logic in LSTM cells. This image was taken from [22], where a more in depth discussion about LSTMs may be found.

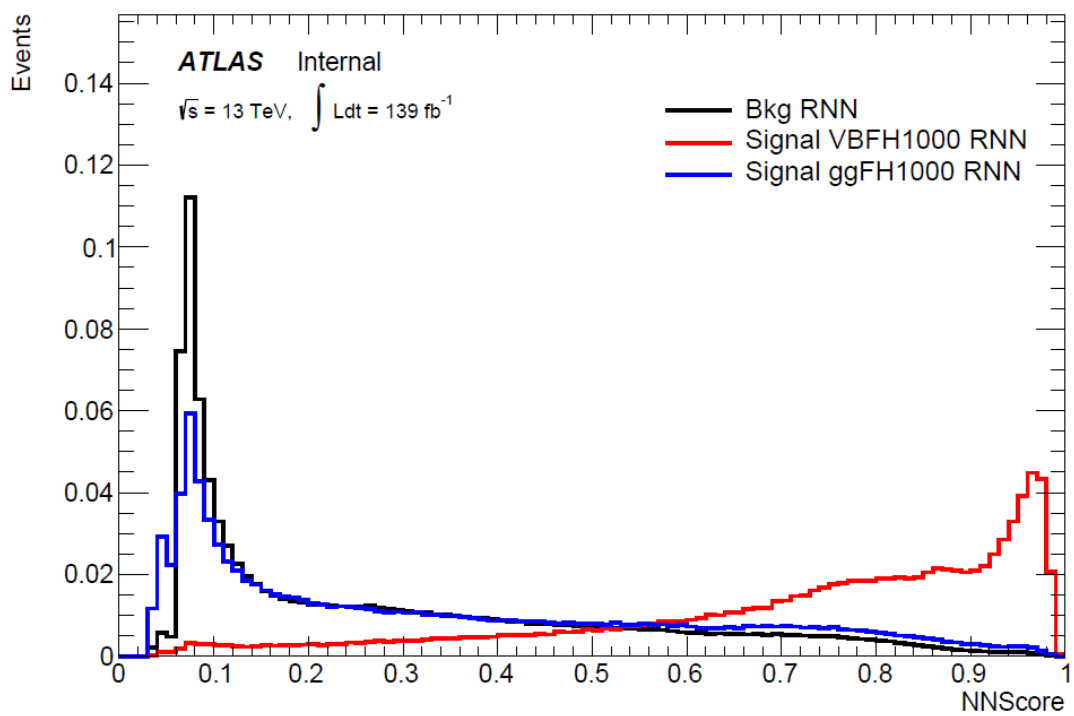


Figure 9.3: RNN Score distribution for ggF and VBF signals and backgrounds.

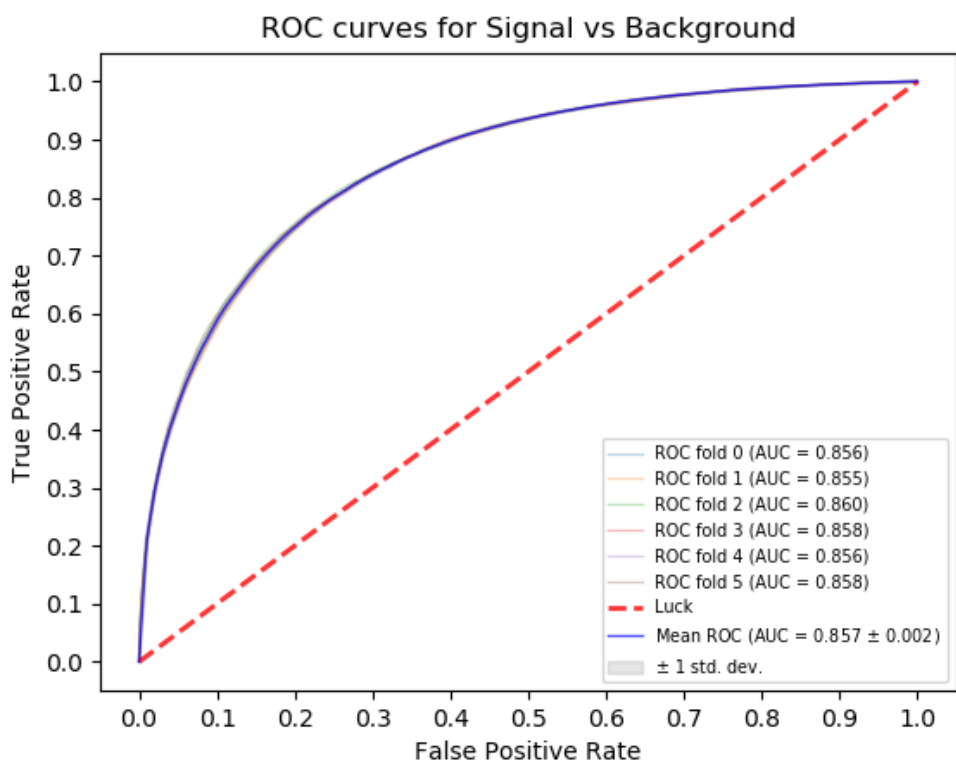


Figure 9.4: ROC curve using k-fold validation for RNN.

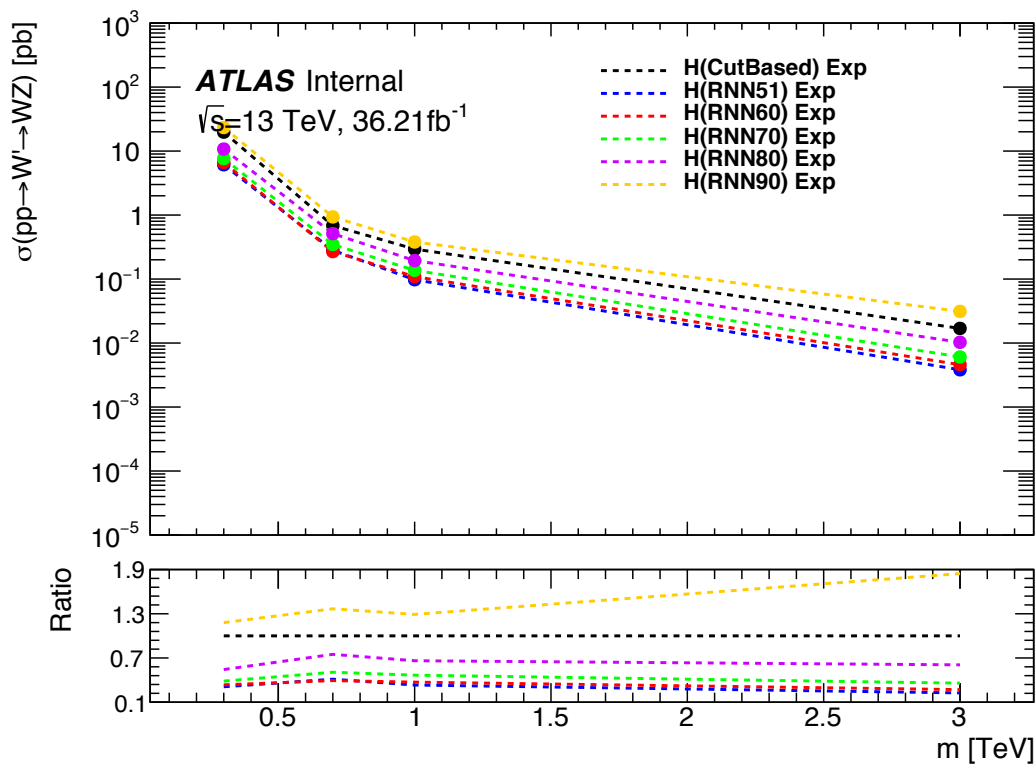


Figure 9.5: Comparison of GGF Z' limits for different RNN score selections. The bottom panel shows the ratio of the upper limits set for different RNN cuts to the cut-based analysis. In this panel smaller numbers, indicate that the expected upper limit is smaller than the cut-based analysis, which is desired.

957 9.4 Signal Region Definitions

958 Signal regions are constructed to be dominated by signal and used in the final
959 likelihood fit to look for a bump in the reconstructed resonance mass distribution.
960 Once an event is classified by the RNN, it must pass topological cuts that maximize
961 S/\sqrt{B} . To efficiently select events with a $W \rightarrow \ell\nu$ candidate exactly one tight
962 lepton is required and $E_T^{miss} > 100(60)$ GeV and $p_{T,\ell\nu} > 200(75)$ GeV in the
963 merged (resolved) analysis to suppress the fake lepton backgrounds.

964 For the merged analysis, in addition to the $W \rightarrow \ell\nu$ and $W/Z \rightarrow J$ selections
965 above, the $\min(p_{T,\ell\nu}, p_{T,J})/m_{WV} > 0.35(0.25)$ for the non-VBF (VBF) category.
966 To reduce $t\bar{t}$ contamination, events with at least one b jet with $\Delta R > 1.0$ from
967 the large-R jet are excluded. High purity signal regions require the D_2 and W/Z
968 mass window cut to be passed, whereas the low purity region only requires the
969 W/Z mass window cut to be passed.

970 For the HVT W' resonance search tagged and untagged regions are used to
971 increase signal acceptance. For events to be classified as tagged the large-R jet
972 must contain exactly two b-tagged jets. Untagged events must have no more than
973 one b-tagged jet matched to the large-R jet. These selections are shown in Table
974 9.2.

975 Events failing the merged selection are then re-analyzed in the resolved cat-
976 egory. To enhance resolved signals, the event should contain two high- p_T boson
977 candidates that are back-to-back in the ϕ as shown by the cuts in Table 9.3.
978 Again, to suppress the $t\bar{t}$ backgrounds, events are required to have no additional
979 b-jets.

980 The WV system mass, m_{WV} is reconstructed from the lepton, neutrino, and
981 hadronically-decaying boson candidate. The momentum of the neutrino along the
982 z -direction is obtained by constraining the W boson mass of the lepton neutrino

983 system to be $80.3 \text{ GeV}/c^2$. For complex solutions to this constraint, p_Z is taken
 984 as either the real component of the solution or the one with the smaller absolute
 985 value of the two real solutions. For the resolved analysis, m_{WV} is reconstructed
 986 by constraining the $W(Z)$ dijet system:

$$p_{T,jj}^{corr} = p_{T,jj} \times \frac{m_{W/Z}}{m_{jj}} \quad (9.1)$$

987

$$m_{jj}^{corr} = m_{W/Z} \quad (9.2)$$

988 where m_{jj} and $m_{W/Z}$ are the reconstructed invariant mass of the hadronically-
 989 decaying W/Z boson and the PDG values of the W/Z boson masses, respectively.
 990 A summary of the resolved selections is shown in Table 9.3.

991 The analysis cutflow is shows in Figure 9.6. Events classified as VBF events
 992 are classified as Merged High purity, low purity or resolved signal region selections
 993 sequentially. If the event does not pass any of these selections but passes a VBF
 994 control region selection it is classified as a VBF CR event. If the event fails the
 995 VBF selection it is then checked if it passes the Merged High purity, Low purity
 996 or resolved signal region selections (NB: for the WZ decay modes all the regions
 997 have tagged and untagged categories). If the event fails all the GGF signal region
 998 selections, it is then kept for GGF control region selections, if it passes those
 999 selections.

Table 9.2: Summary of selection criteria used to define the signal region (SR), $W+jets$ control region (W CR) and $t\bar{t}$ control region ($t\bar{t}$ CR) for merged 1-lepton channel.

Selection	SR		W CR (WR)		$t\bar{t}$ CR (TR1)	
	HP	LP	HP	LP	HP	LP
$W \rightarrow \ell\nu$	Num of Tight leptons		1			
	Num of Loose leptons		0			
	E_T^{miss}		> 100 GeV			
	$p_T(\ell\nu)$		> 200 GeV			
$W/Z \rightarrow J$	Num of large- R jets		≥ 1			
	D_2 cut		pass	fail	pass	fail
	W/Z mass window cut		pass	pass	fail	pass
	Numb. of associated VR track jets b -tagged		For $Z \rightarrow J$: ≤ 1 ($= 2$) for untagged (tagged) category			
Topology cut	$\min(p_{T,\ell\nu}, p_{T,J}) / m_{WV}$		> 0.35(0.25) for DY/ggF (VBF) category			
Top-quark veto	Num of b -tagged jets outside of large- R jet		0		≥ 1	
	Pass VBF selection		no (yes) for DY/ggF (VBF) category			

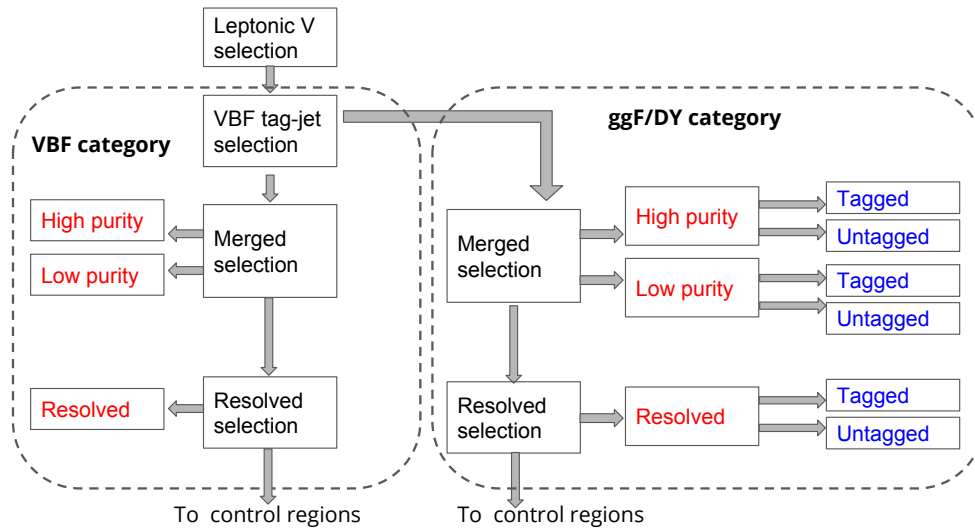


Figure 9.6: Event Categorization. Natasha write more.

Table 9.3: The list of selection cuts in the resolved analysis for the WW and WZ signal regions (SR), W +jets control region (WR) and $t\bar{t}$ control region (TR).

cuts		SR	W CR (WR)	$t\bar{t}$ CR (TR1)
$W \rightarrow \ell\nu$	Number of Tight leptons		1	
	Number of Loose leptons		0	
	E_T^{miss}		> 60 GeV	
	$\$p_T(\ell\nu)$		> 75 GeV	
$W/Z \rightarrow jj$	Number of small-R jets		≥ 2	
	Leading jet p_T		> 60 GeV	
	Subleading jet p_T		> 45 GeV	
	$Z \rightarrow q\bar{q}$	$78 < m_{jj} < 105$ GeV	$50 < m_{jj} < 68$ GeV or	$50 < m_{jj} < 150$ GeV
Topology cuts	$W \rightarrow q\bar{q}$	$68 < m_{jj} < 98$ GeV	$105 < m_{jj} < 150$ GeV	
	Num. of b -tagged jets	For $Z \rightarrow jj$: ≤ 1 ($= 2$) for untagged (tagged) category		
	$\Delta\phi(j, \ell)$		> 1.0	
	$\Delta\phi(j, E_T^{miss})$		> 1.0	
Top veto	$\Delta\phi(j, j)$		< 1.5	
	$\Delta\phi(\ell, E_T^{miss})$		< 1.5	
min $(p_{T,\ell\nu}, p_{T,jj}) / m_{WV}$		$> 0.35(0.25)$ for DY/ggF (VBF) category		
Top veto	Number of additional b -tagged jets	0		≥ 1
	Pass VBF selection	no (yes) for DY/ggF (VBF) category		

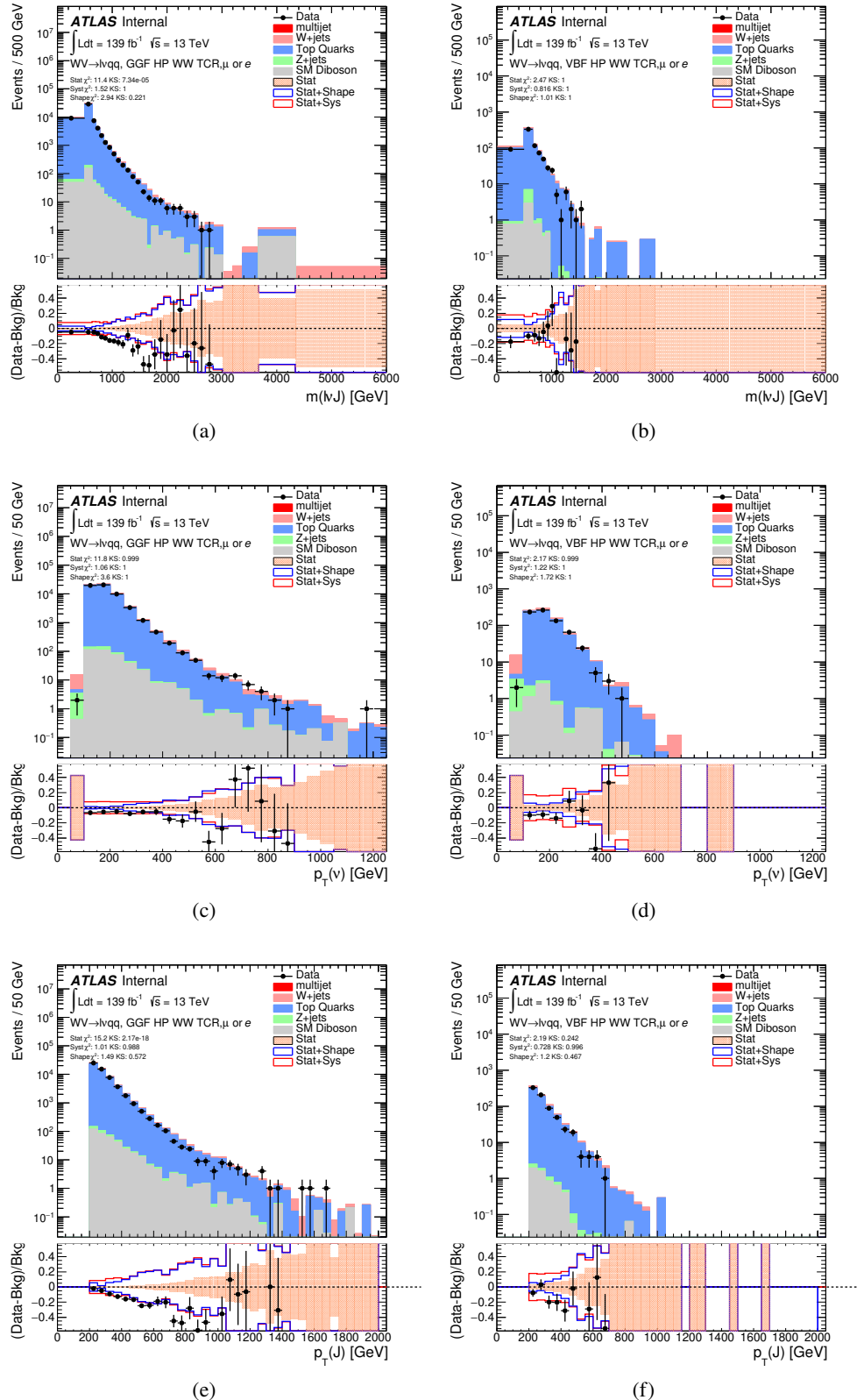


Figure 9.7: Data MC comparison for the merged WW HP TCR. The bottom panel shows the ratio of the difference⁸⁷ between data and simulation to simulation. The red bands include the all systematic and statistical uncertainties on the background.

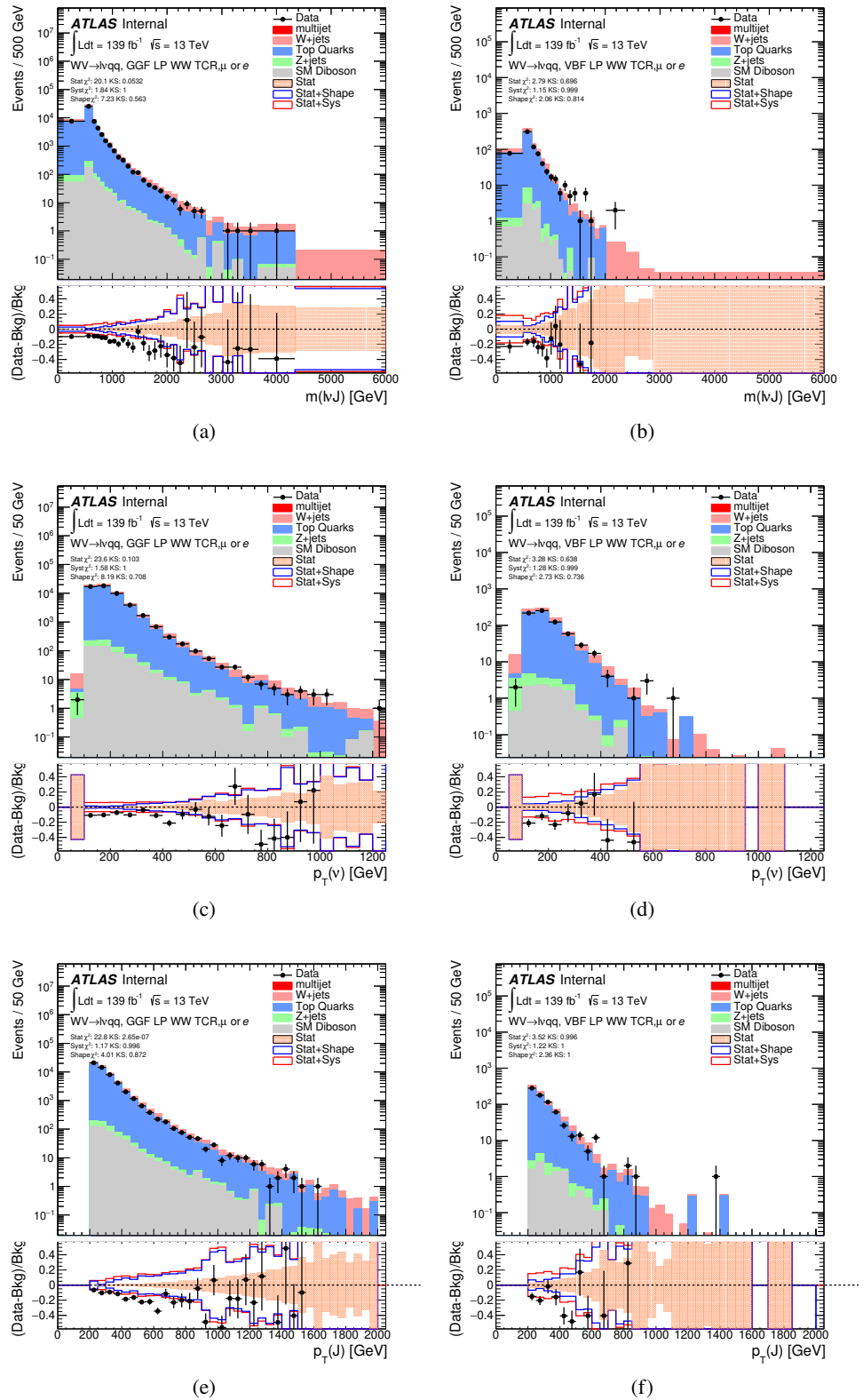


Figure 9.8: Data MC comparison for the merged WW LP TCR. The bottom panel shows the ratio of the difference between data and simulation to simulation. The red bands include the all systematic and statistical uncertainties on the background.⁸⁸

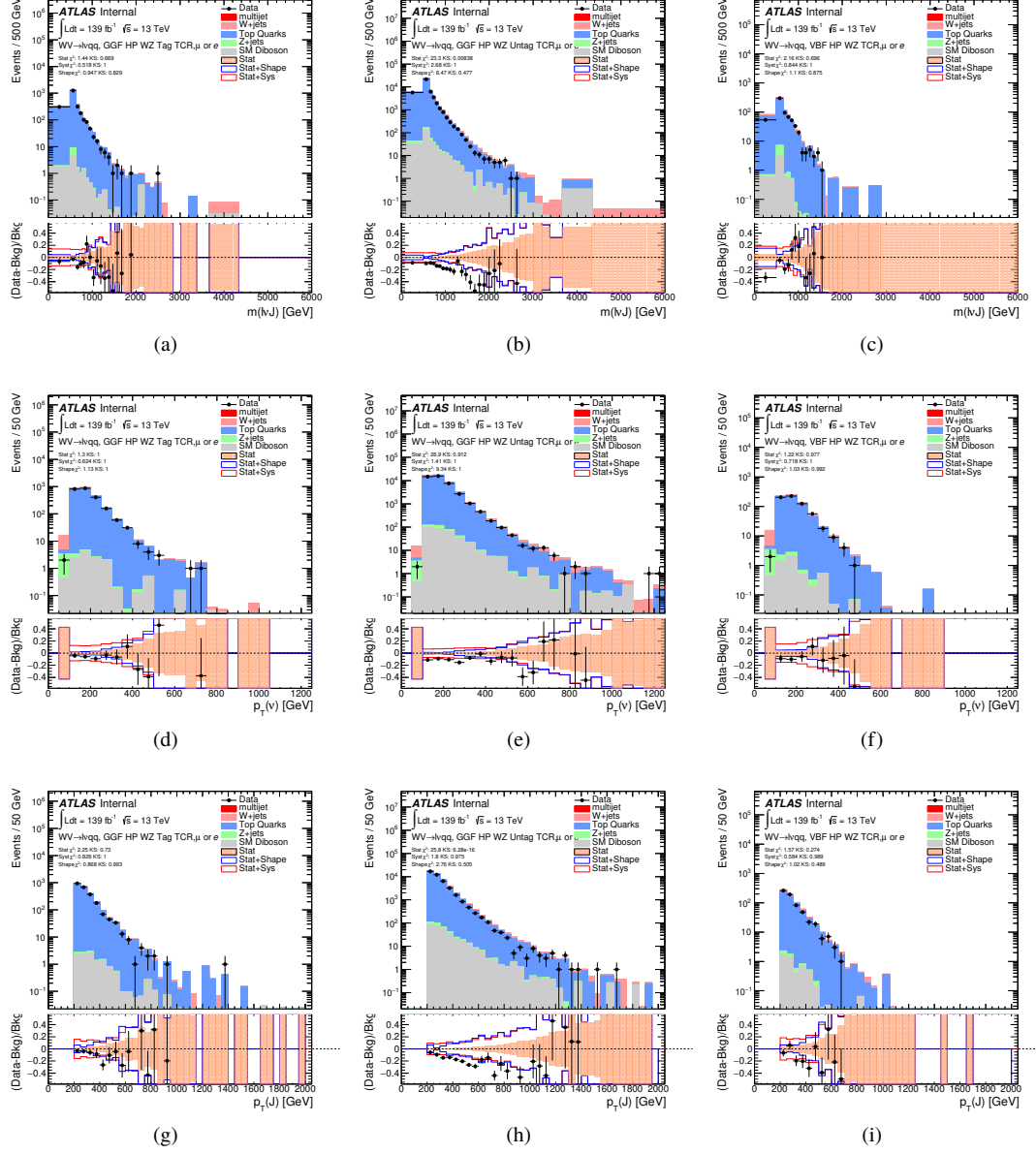


Figure 9.9: Data MC comparison for the merged WZ HP TCR. The bottom panel shows the ratio of the difference between data and simulation to simulation. The red bands include the all systematic and statistical uncertainties on the background.

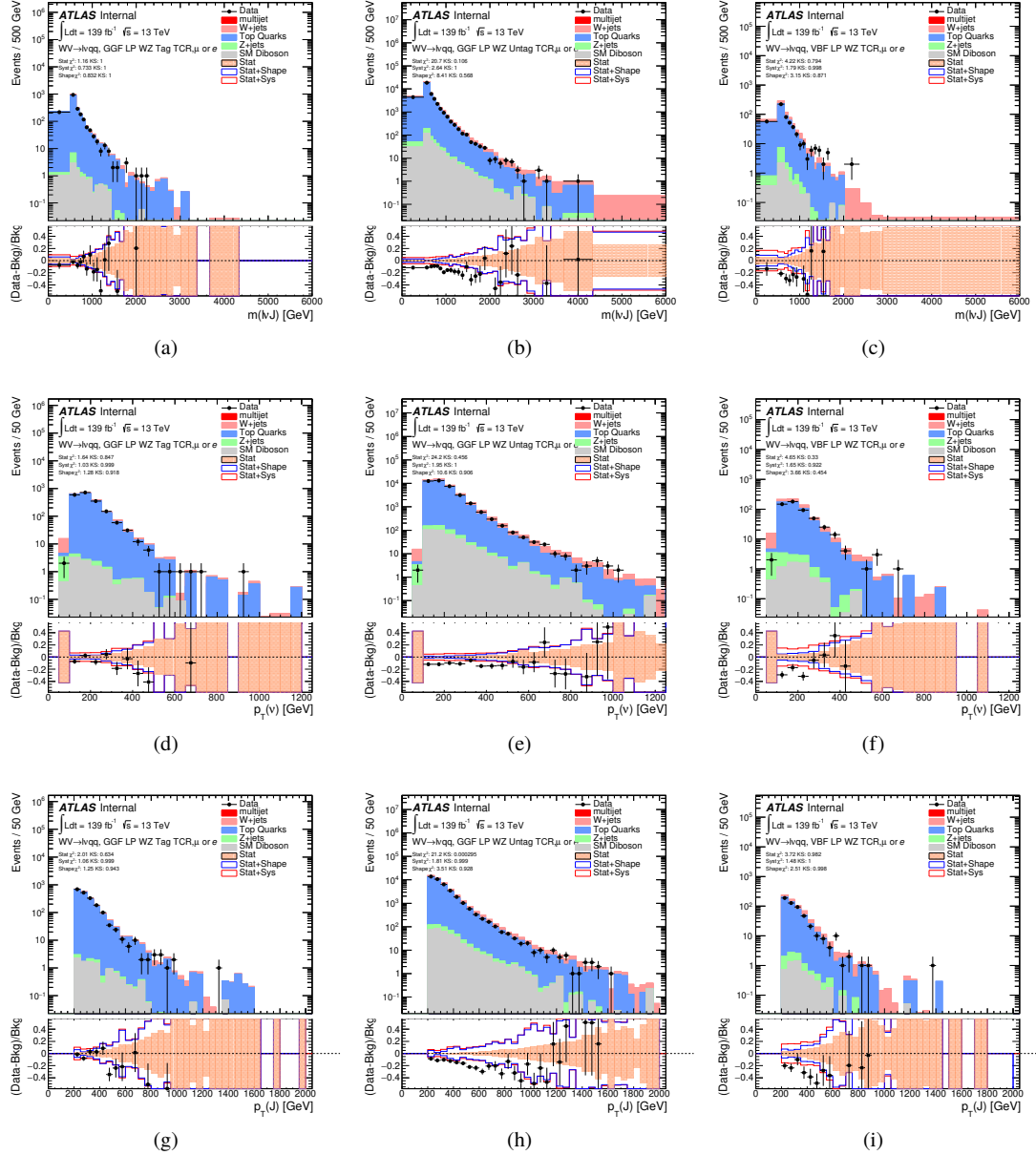


Figure 9.10: Data MC comparison for the merged WZ LP TCR. The bottom panel shows the ratio of the difference between data and simulation to simulation. The red bands include the all systematic and statistical uncertainties on the background.

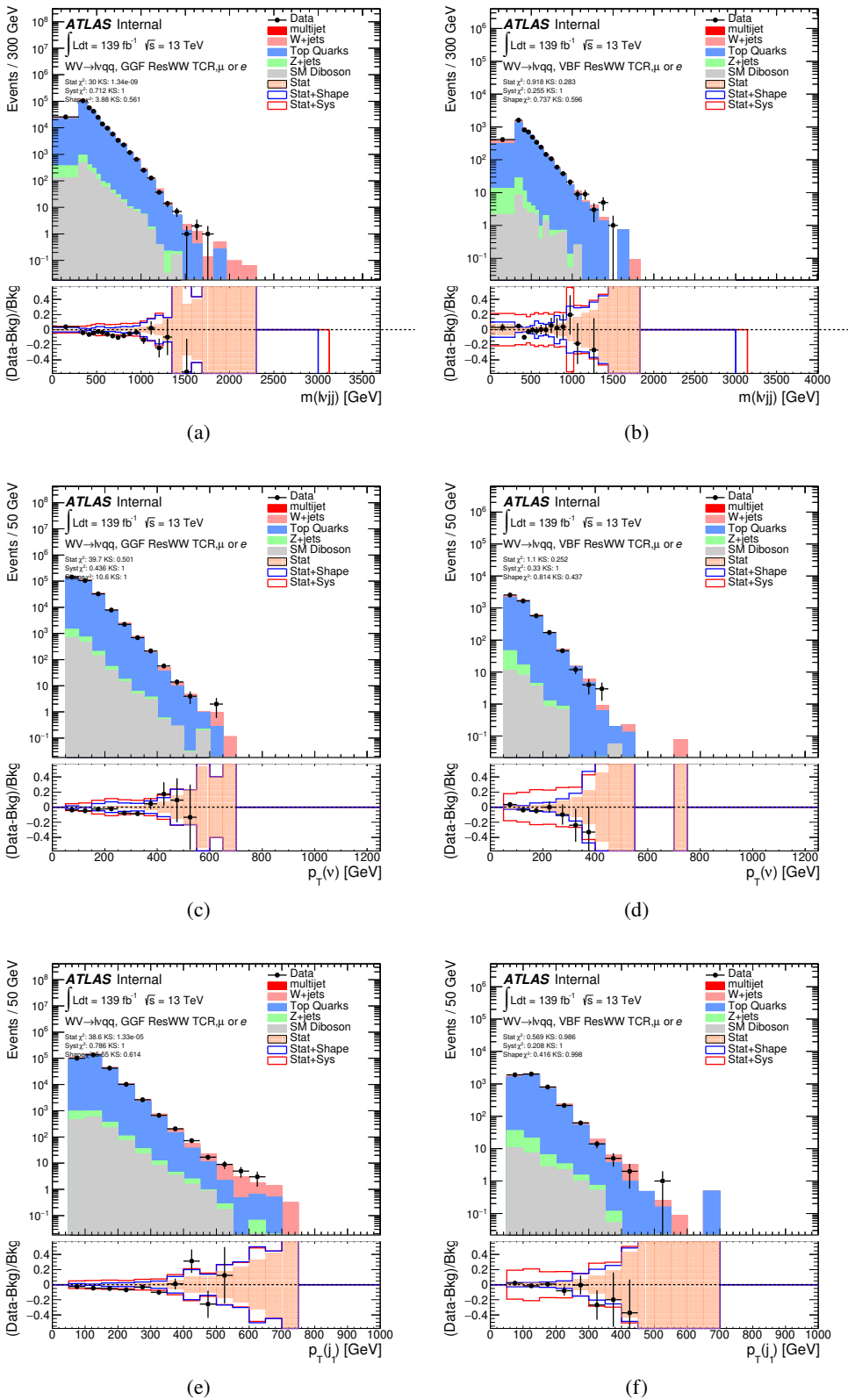


Figure 9.11: Data MC comparison for the resolved WW TCR. The bottom panel shows the ratio of the difference between data and simulation to simulation. The red bands include the all systematic and statistical uncertainties on the background.

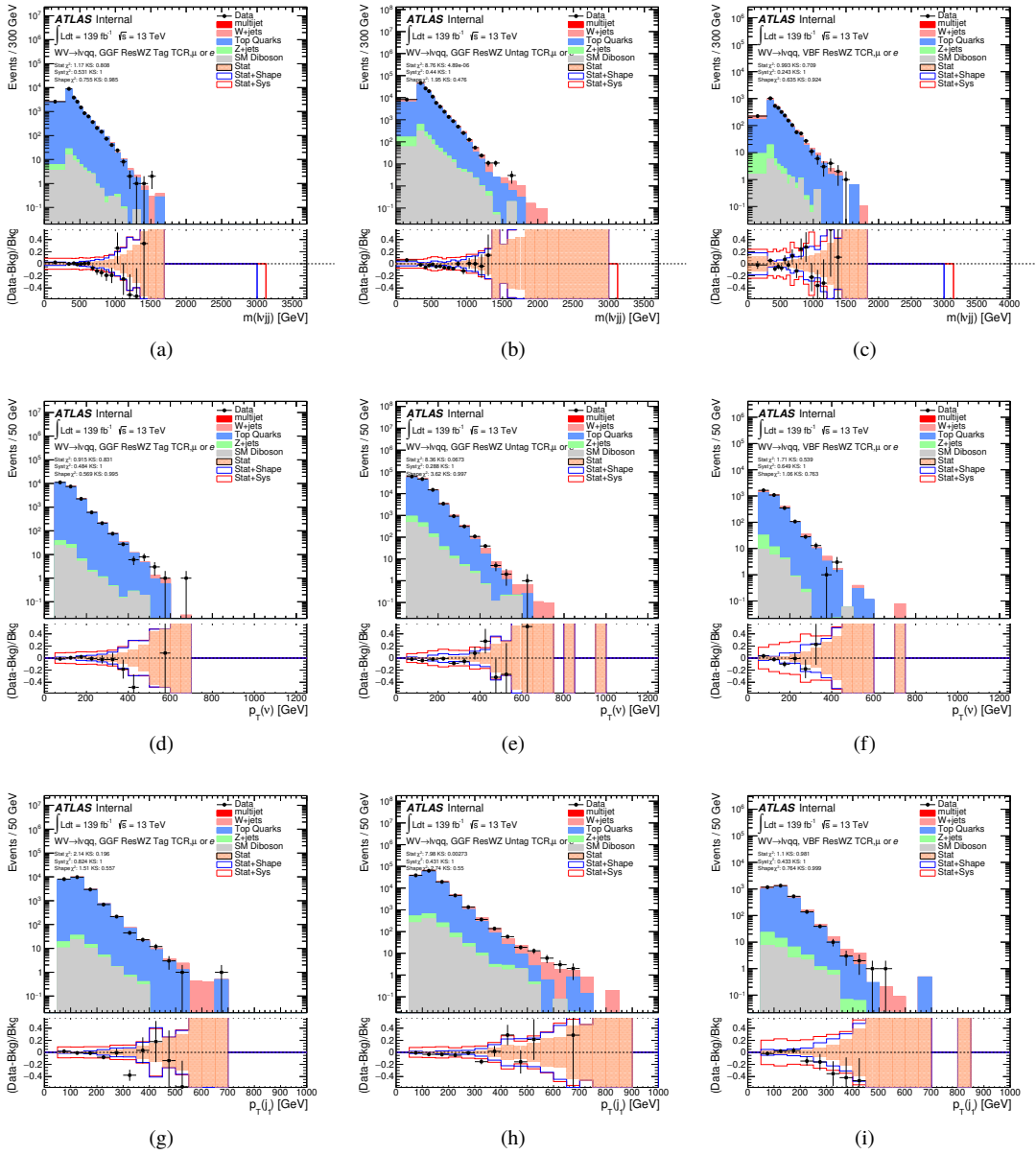


Figure 9.12: Data MC comparison for the resolved WZ TCR. The bottom panel shows the ratio of the difference between data and simulation to simulation. The red bands include the all systematic and statistical uncertainties on the background.

1000 9.5 Selection Acceptance times efficiency for Sig- 1001 nal Events

1002 The acceptance times efficiency for the signal region selection is defined as:

$$A \cdot \epsilon = \frac{N_{\text{events selected}}^{\text{truth}}}{N_{\text{events generated}}^{\text{truth}}} \cdot \frac{N_{\text{events selected}}^{\text{reco}}}{N_{\text{events selected}}^{\text{truth}}} = \frac{N_{\text{events selected}}^{\text{reco}}}{N_{\text{events generated}}^{\text{truth}}} \quad (9.3)$$

1003 The distributions of $A \cdot \epsilon$ as a function of the resonance mass for the different spin
1004 models are shown in Figures 9.14 - ??.

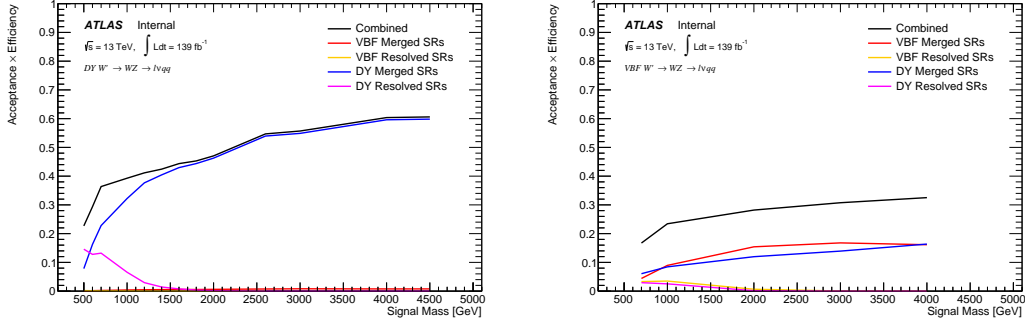


Figure 9.13: Selection acceptance times efficiency for the $W' \rightarrow WZ \rightarrow \ell\nu qq$ events from MC simulations as a function of the W' mass for (a) Drell-Yan and (b) VBF production, combining the merged HP and LP signal regions of the $WW \rightarrow \ell\nu J$ selection and the resolved regions of the $WW \rightarrow \ell\nu jj$ selection.

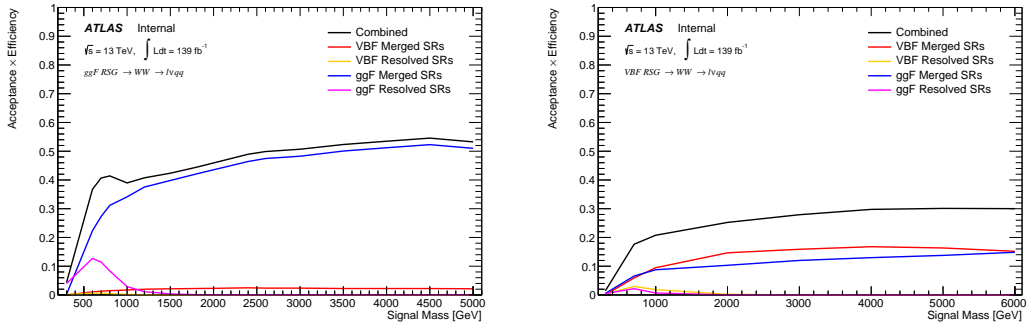


Figure 9.14: Selection acceptance times efficiency for the $G \rightarrow WW \rightarrow \ell\nu qq$ events from MC simulations as a function of the G mass for (a) Drell-Yan and (b) VBF production, combining the merged HP and LP signal regions of the $WW \rightarrow \ell\nu J$ selection and the resolved regions of the $WW \rightarrow \ell\nu jj$ selection.

1005 9.6 Background Estimate

1006 9.6.1 Control Regions

1007 The distributions for the variables used in merged analysis for top control
1008 regions are shown in Figure 9.7-9.10.

1009 The distributions for the variables used in the resolved analysis in the TCR
1010 are shown in Figure 9.11, 9.12.

1011 To more accurately model the two dominant backgrounds in this analysis,
1012 $W+jets$ and $t\bar{t}$, control regions are constructed for each. These control regions
1013 are dominated by these processes and used to extract normalization factors in
1014 the final likelihood fit that are then used in the signal region estimates. For the
1015 $t\bar{t}$ control region the event must contain at least one such b jet. The WCR is
1016 constructed using the $m_{jj/J}$ mass window sidebands. All other backgrounds are
1017 estimated using simulation, except fake lepton backgrounds, which are derived
1018 using a data-driven method.

1019 **9.6.2 Fake Lepton Backgrounds**

1020 Backgrounds in this analysis containing real leptons (e.g. $W/Z + \text{jets}$, diboson,
1021 $t\bar{t}$, single- t) are well-modeled with simulated samples and constrained with data
1022 from CRs. However, the fake lepton background (also referred to as the multijet
1023 background) is not well-modeled with simulation. For this reason, the multijet
1024 background is extracted from data. Heavy flavor decay products, jets, and con-
1025 verted photons can be mistakenly reconstructed as electrons. Fake electrons often
1026 arise from jet fakes while non-prompt muons usually arise from heavy flavor decay.
1027 For this analysis, these fake electrons generally fail the electron ID criteria and
1028 fake muons fail the muon isolation requirement. Therefore, to derive the multijet
1029 template shape the SR and CR selections and inverted lepton requirements are
1030 used as seen in Table 9.4. NB: by inverting the lepton isolation/identification
1031 criteria the SRs and CRs are orthogonal.

1032 The template shape of the MJ background is determined by using a multijet
1033 validation region (MJVR) that requires the inverted lepton isolation/identification
1034 requirement and the two signal jets to satisfy the m_{jj} requirement used in the
1035 $W + \text{jets}$ CRs. The E_T^{miss} distribution in MJCR is shown in Figure 9.15 for 2017
1036 data. The template is then extracted by subtracting the data in the MJVR from
1037 the electroweak background processes. The resulting template and electroweak
1038 backgrounds are then fit to data. In this fit, the E_T^{miss} distribution compared to
1039 data to extract electroweak background, multijet electron and muon background
1040 normalizations. The fitted scale factors from this MJVR template are then applied
1041 in the MJCR template. The electron and muon background normalizations in the
1042 MJCR template are parameters in the final simultaneous fit. Technically, there
1043 should be a separate template for every CR and SR, but some MJ regions have
1044 insufficient statistics to do this. Additionally, the shapes for the MJ templates for

1045 VBF and ggF regions are found to be compatible within statistical uncertainty.
 1046 Therefore, the sample MJ template used for VBF and ggF CR/SRs, but with
 1047 different pre-MJ-fit scale factors.

1048 This template method was validated using WCR and full Run 2 data. The
 1049 results of the fit are shown in Table 9.5. The multijet contribution in the muon
 1050 channel for $p_T^W > 150$ GeV is consistent with zero, and therefore neglected in
 1051 the final fit. Applying the extracted normalization factor to MJVR in WCRs for
 1052 various kinematic variables such as E_T^{miss} , W transverse mass, lepton p_T , and the
 1053 invariant mass as show in Figures 9.16 -9.25. These figures show good agreement
 1054 between the data and background estimate.

Table 9.4: Definitions of “inverted” leptons used in multijet control region

	Criterion	signal lepton	inverted lepton
Electron	ID	TightLH	MediumLH !TightLH
	Calo Isolation	FixedCutHighPtCaloOnlyIso	FixedCutHighPtCaloOnlyIso
Muon	ID	WHSignalMuon	WHSignalMuon
	Track Isolation	FixedCutTightTrackOnlyIso	!FixedCutTightTrackOnlyIso $ptvarcone30/pt < 0.07^*$
*Only applied to events with $pTW < 150GeV$			

1055

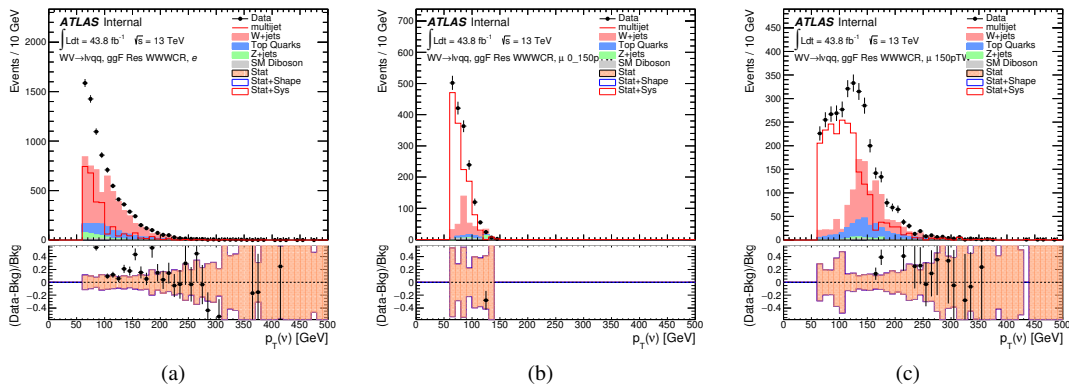


Figure 9.15: The E_T^{miss} distribution in MJCR for 2017 data in the electron channel(left), muon channel with W -boson $pT < 150$ GeV (center) and > 150 GeV (right). Multi-jet templates are calculated as remaining data components after excluding known MC

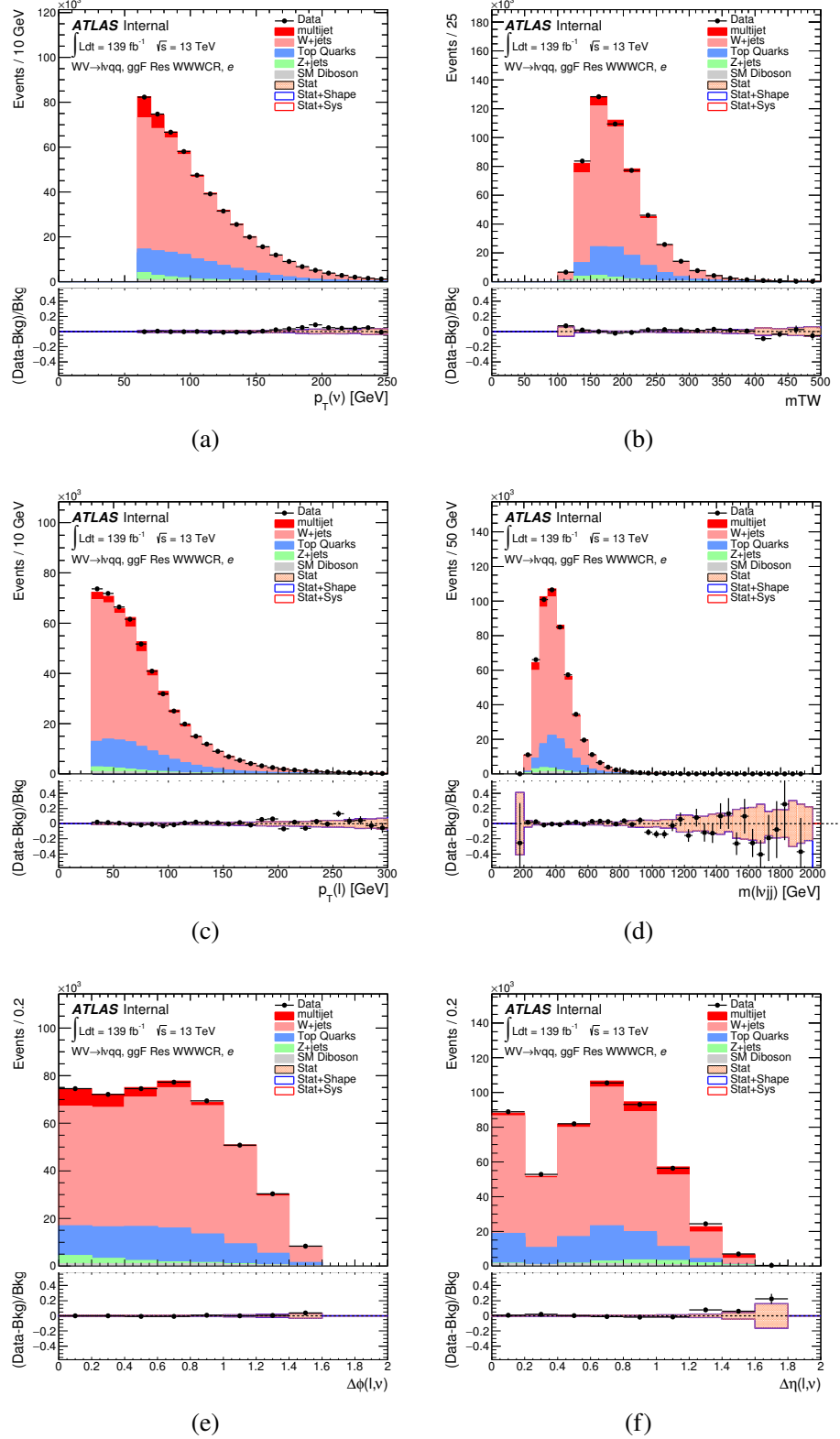


Figure 9.16: Postfit Data/MC comparison of distributions of E_T^{miss} , m_T^W , lepton and neutrino p_T , $m_{l\nu jj}$, lepton- ν angular distance in the WW electron channel. The MJ template is obtained from the pre-MJ-fit.

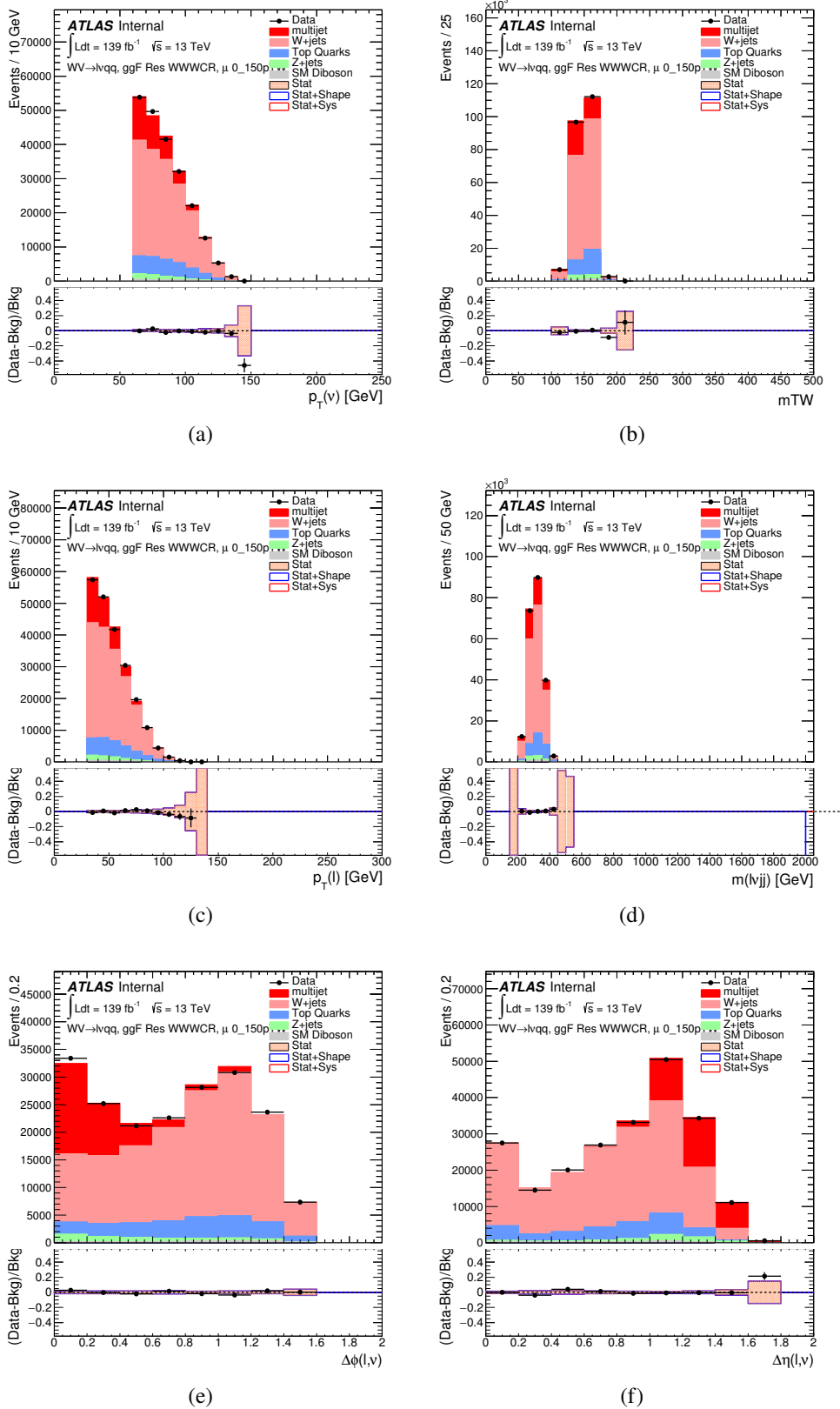


Figure 9.17: Postfit Data/MC comparison of distributions of E_T^{miss} , m_T^W , lepton and neutrino p_T , m_{ljj} , lepton- ν angular distance in the WW muon channel. The MJ template is obtained from the pre-MJ-fit.

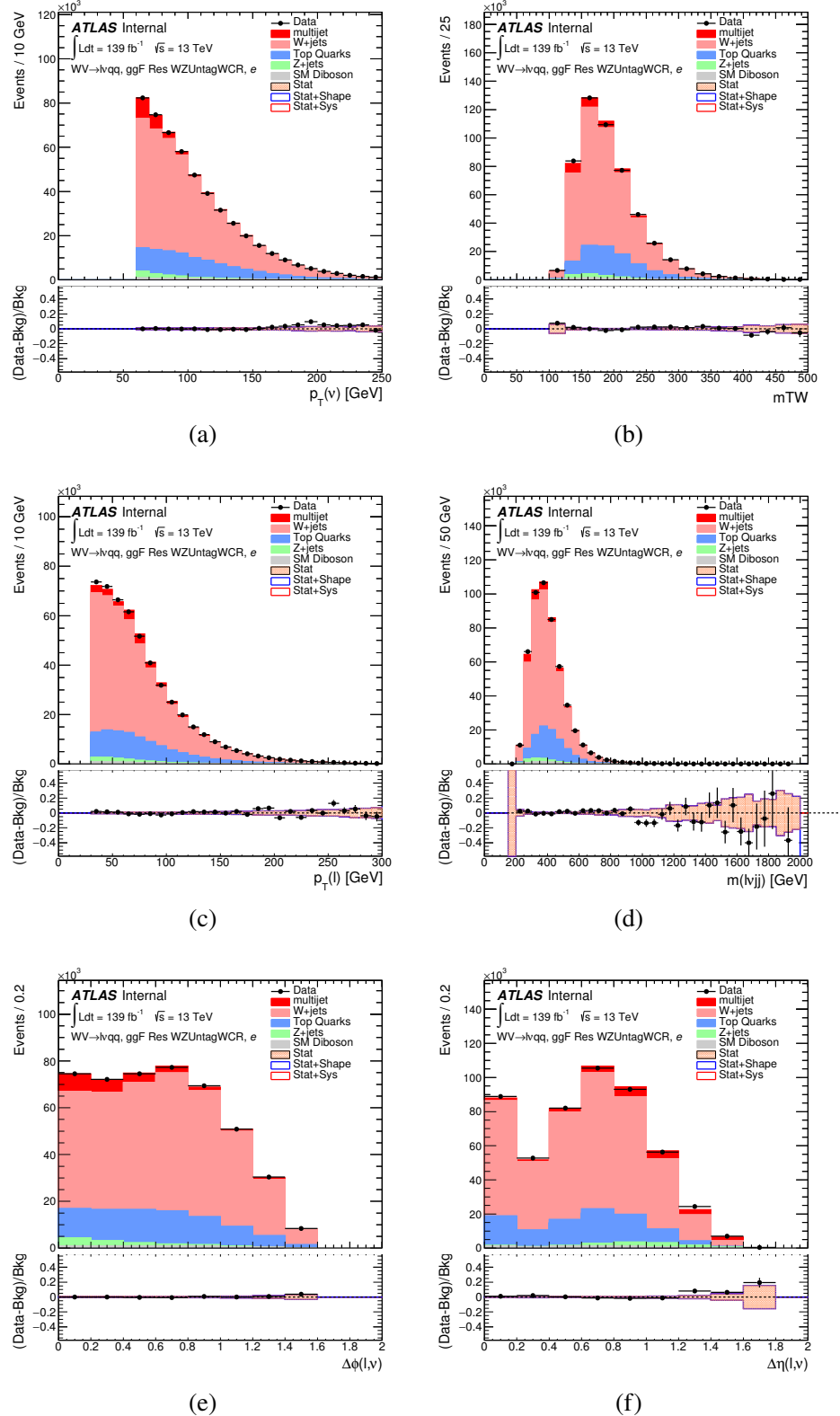


Figure 9.18: Postfit Data/MC comparison of distributions of E_T^{miss} , m_T^W , lepton and neutrino p_T , $m_{l\nu jj}$, lepton- ν angular distance in the WZ untag electron channel. The MJ template is obtained from the pre-MJ-fit.

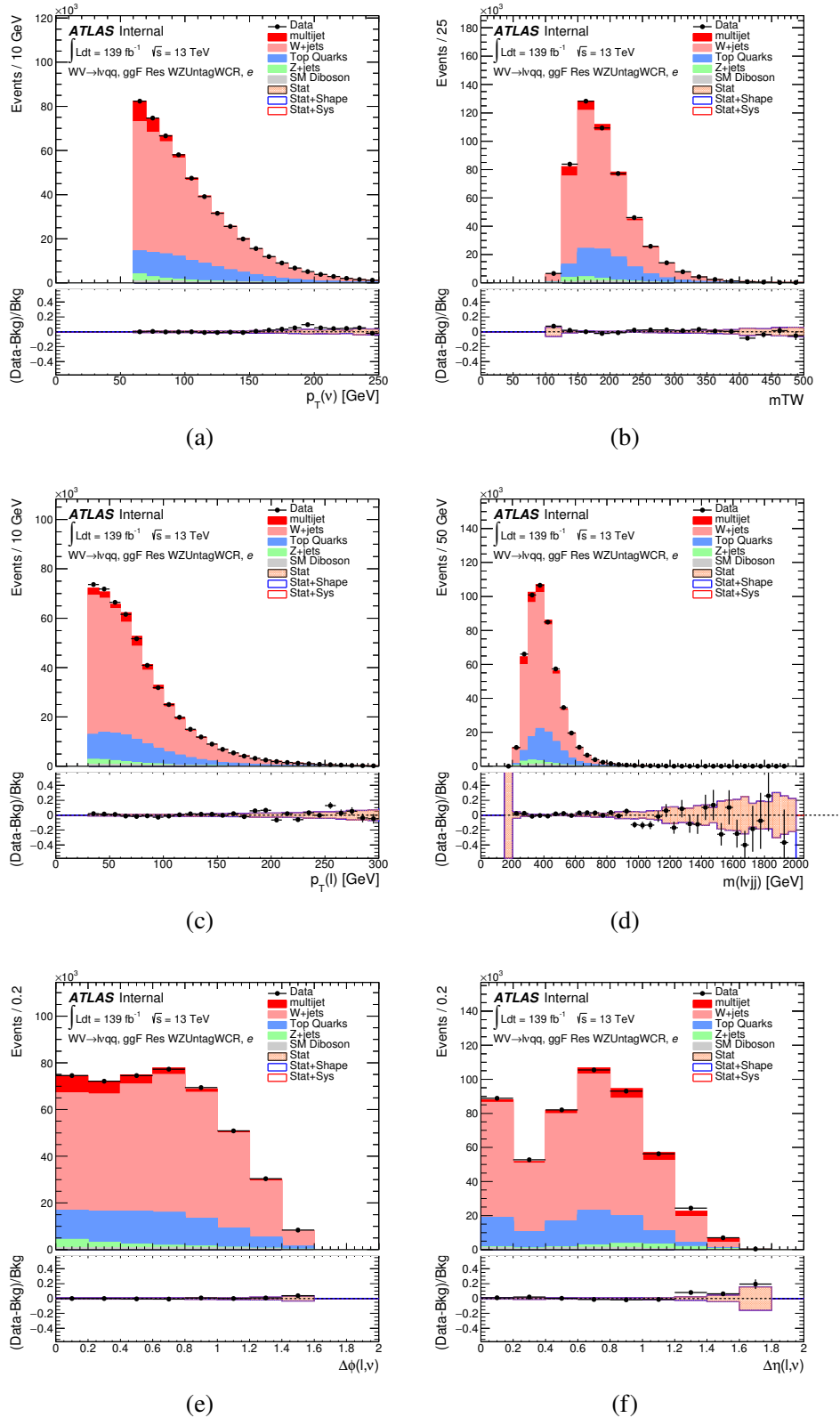


Figure 9.19: Postfit Data/MC comparison of distributions of E_T^{miss} , m_T^W , lepton and neutrino p_T , $m_{l\nu jj}$, lepton- ν angular distance in the WZ untag muon channel. The MJ template is obtained from the pre-MJ-fit.

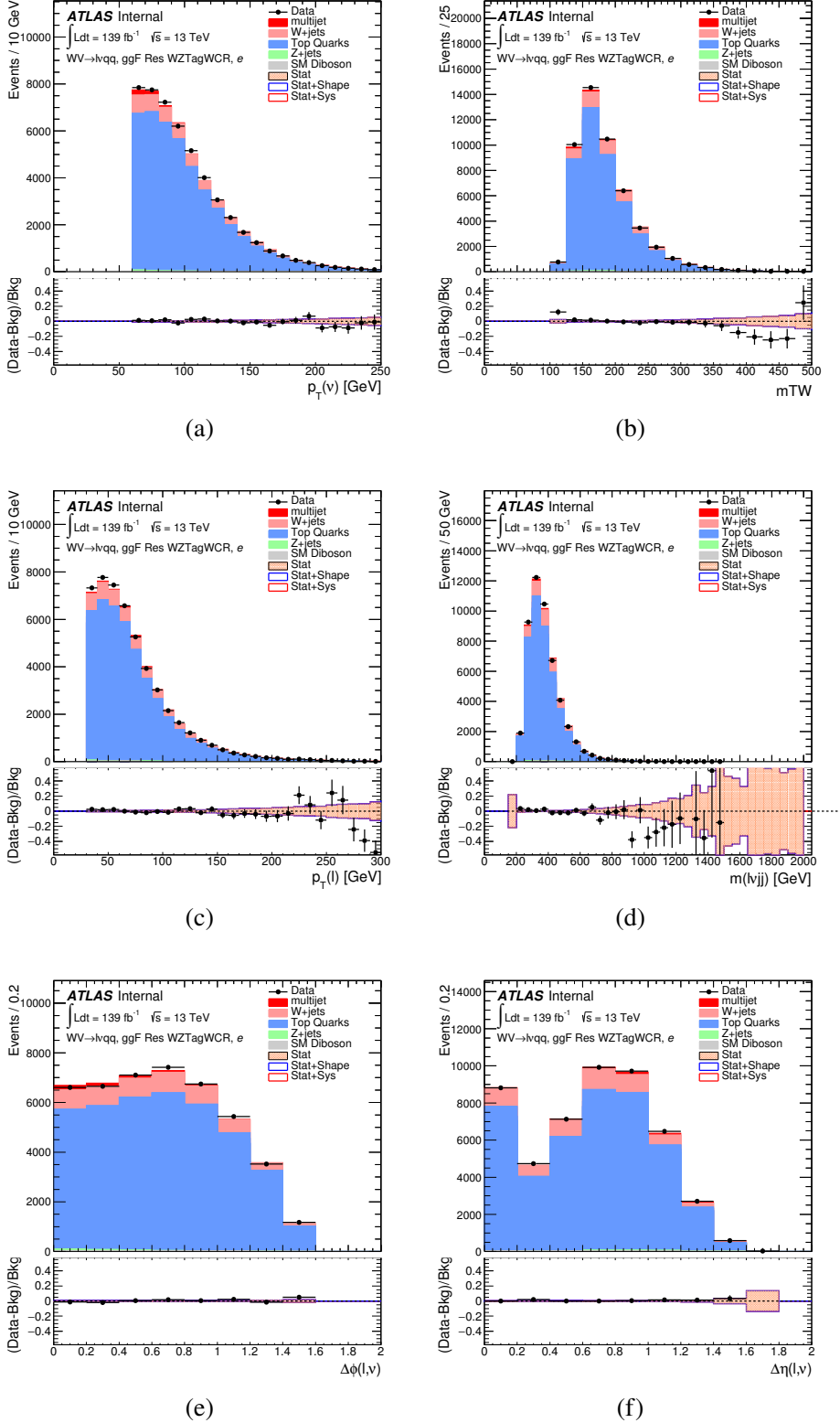


Figure 9.20: Postfit Data/MC comparison of distributions of E_T^{miss} , m_T^W , lepton and neutrino p_T , $m_{l\nu jj}$, lepton- ν angular distance in the WZ untag electron channel. The MJ template is obtained from the pre-MJ-fit.

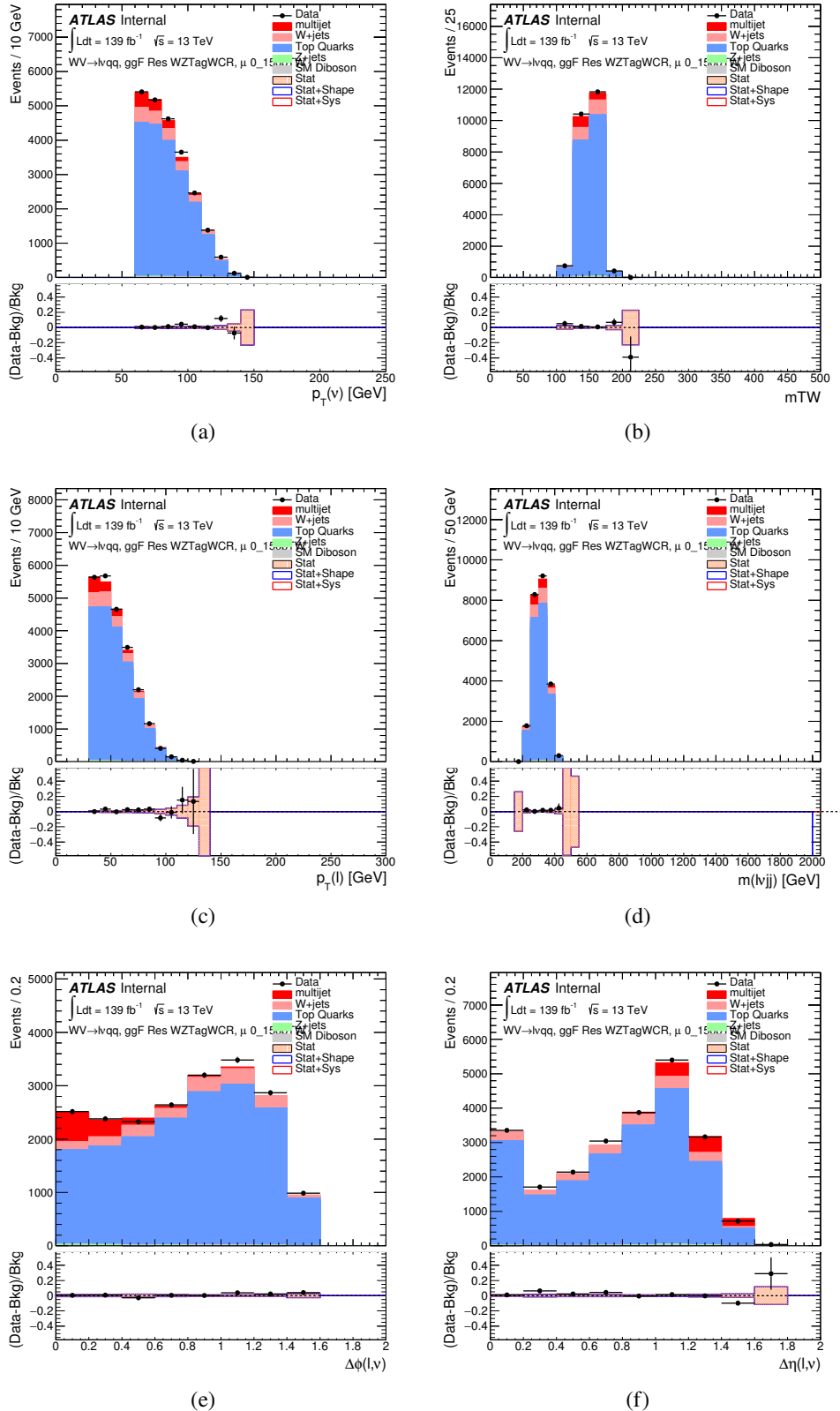


Figure 9.21: Postfit Data/MC comparison of distributions of E_T^{miss} , m_T^W , lepton and neutrino p_T , $m_{l\nu jj}$, lepton- ν angular distance in the WZ untag muon channel. The MJ template is obtained from the pre-MJ-fit.

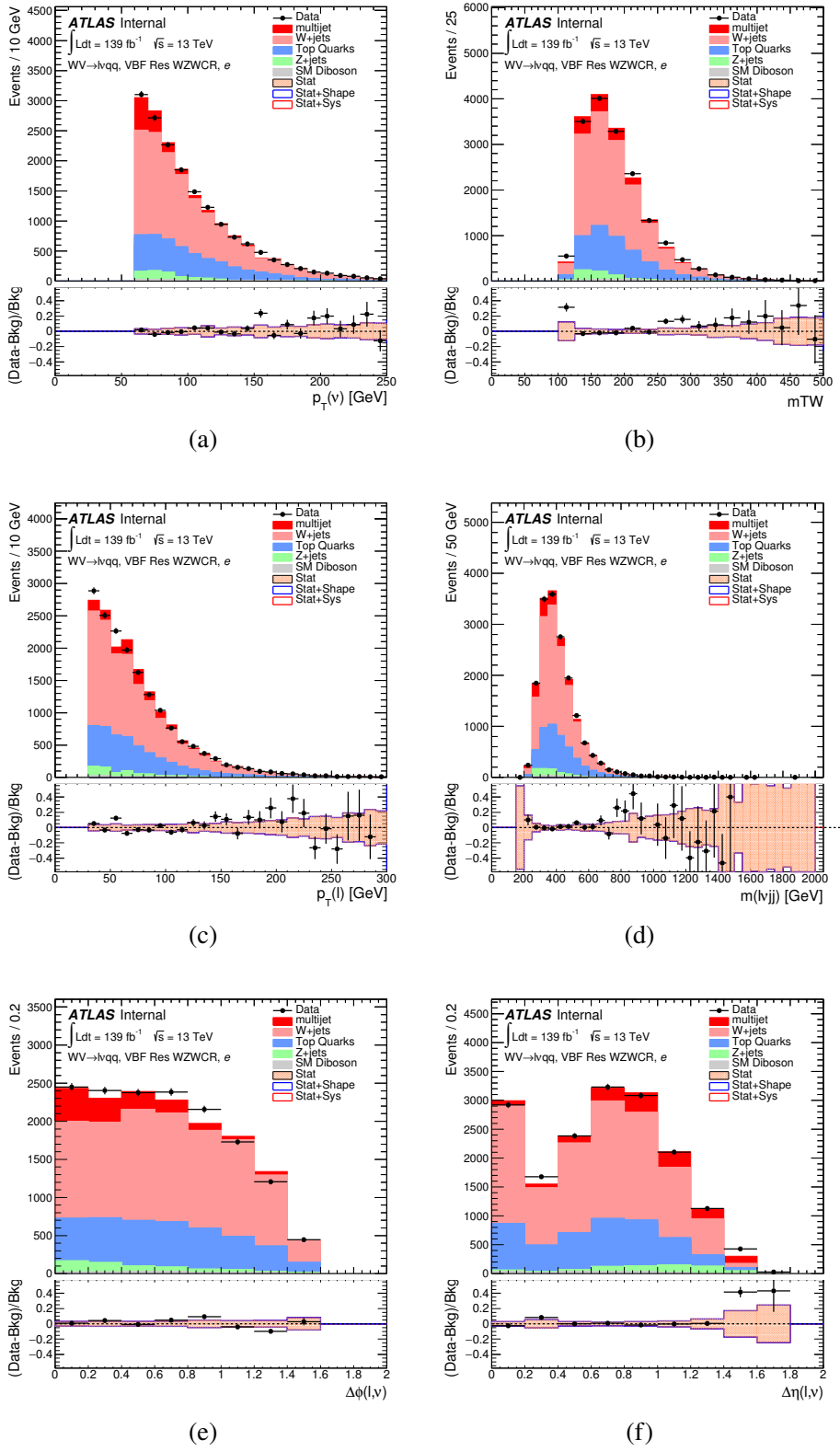


Figure 9.22: Postfit Data/MC comparison of distributions of E_T^{miss} , m_T^W , lepton and neutrino p_T , $m_{l\nu jj}$, lepton- ν angular distance in the VBF WW electron channel. The MJ template is obtained from the pre-MJ-fit.

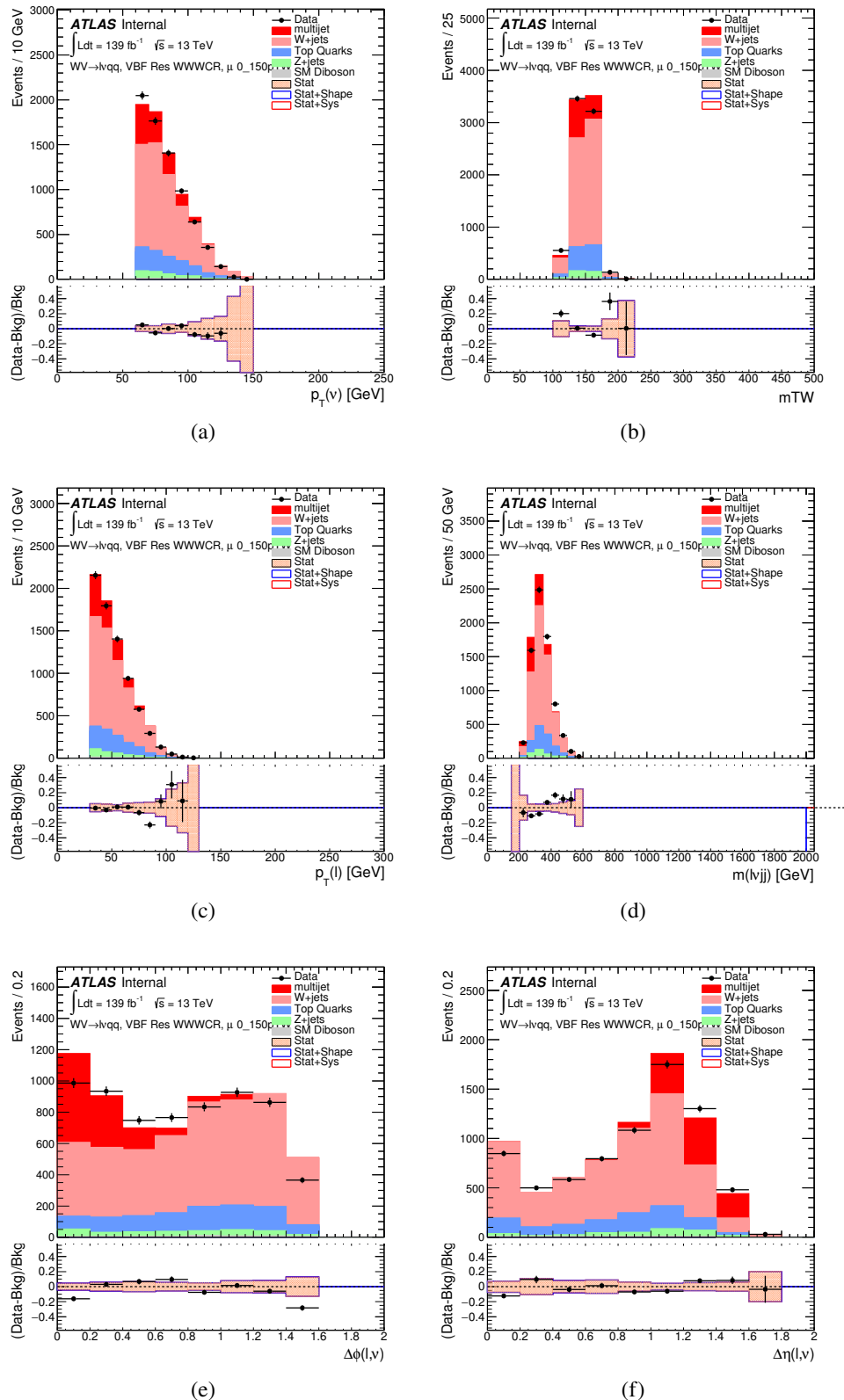


Figure 9.23: Postfit Data/MC comparison of distributions of E_T^{miss} , m_T^W , lepton and neutrino p_T , $m_{\ell\nu jj}$, lepton- ν angular distance in the VBF WW muon channel. The MJ template is obtained from the pre-MJ-fit.

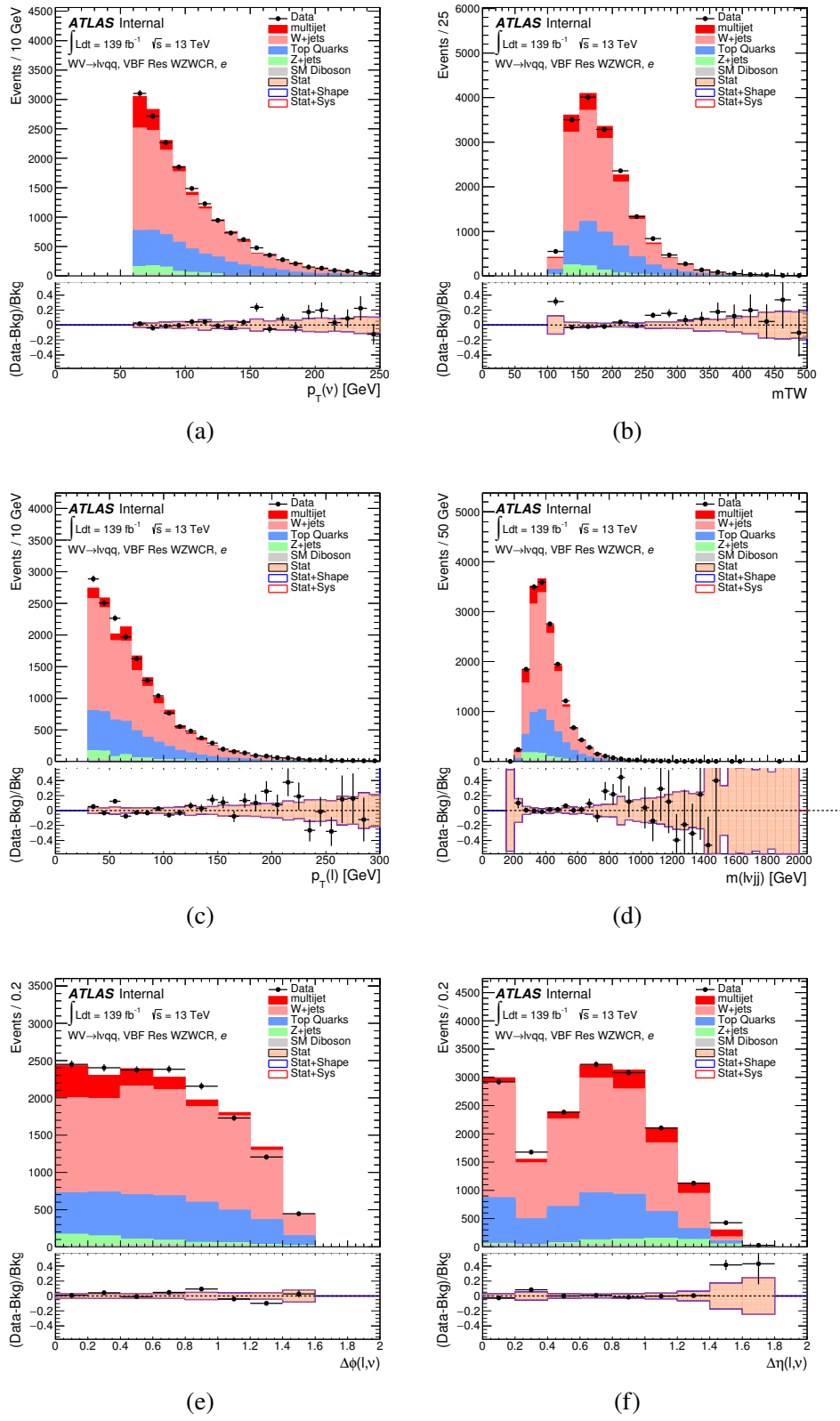


Figure 9.24: Postfit Data/MC comparison of distributions of E_T^{miss} , m_T^W , lepton and neutrino p_T , $m_{l\nu jj}$, lepton- ν angular distance in the VBF WZ electron channel. The MJ template is obtained from the pre-MJ-fit.

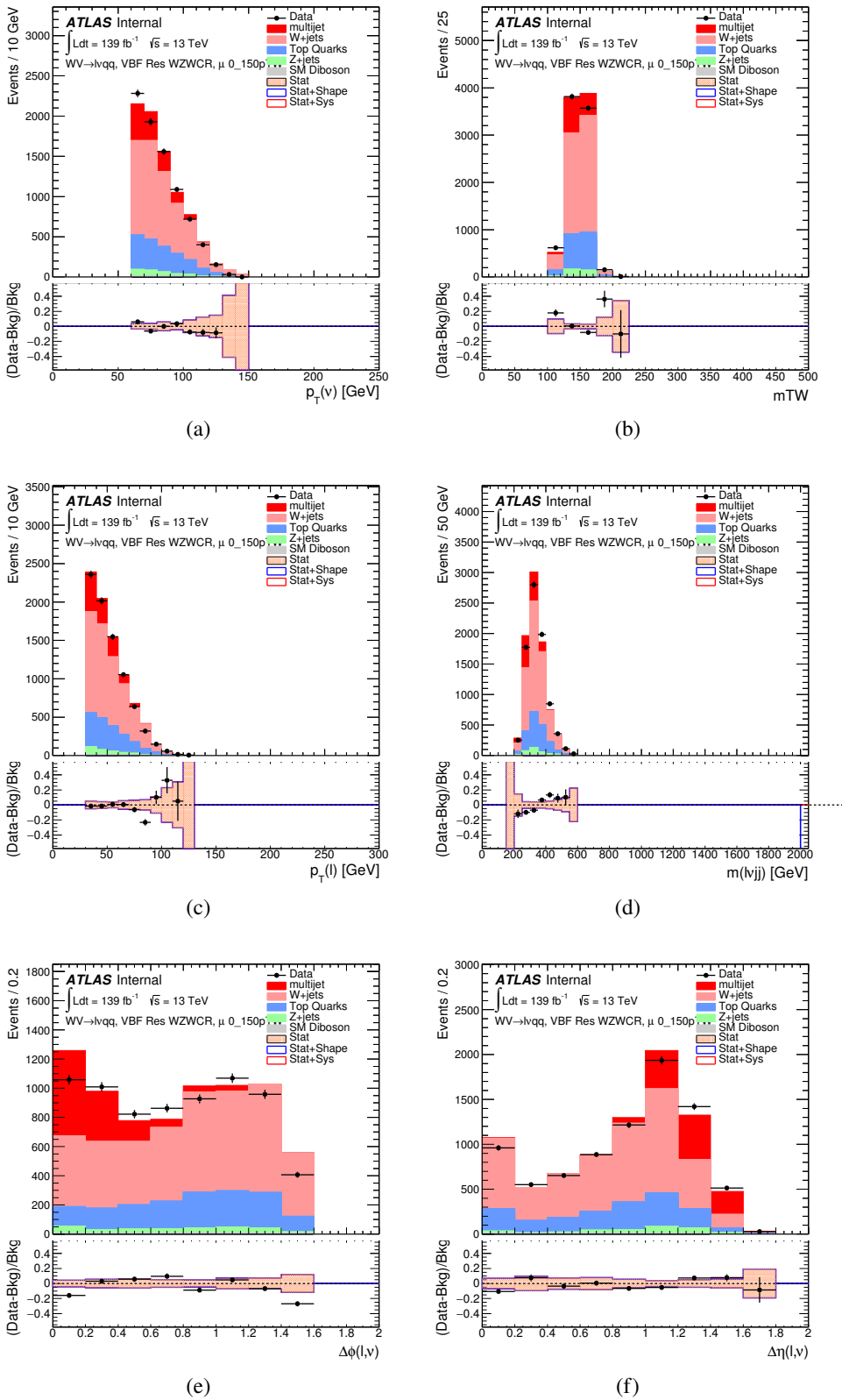


Figure 9.25: Postfit Data/MC comparison of distributions of E_T^{miss} , m_T^W , lepton and neutrino p_T , $m_{l\nu jj}$, lepton- ν angular distance in the VBF WZ muon channel. The MJ template is obtained from the pre-MJ-fit.

Full Run 2
ggF Res WWWCR

Sample	Yield	R.U.	SF
Top&W	645040 ± 1971.68	0.31%	0.998
Z&VV	24075.9		fixed
MJ_el	24156.3 ± 1224.62	5.06%	3.973
MJ_mu	35528.5 ± 923.94	2.60%	9.019

ggF Res WZ01bWCR

Sample	Yield	R.U.	SF
Top&W	644690 ± 1981.4	0.31%	0.997
Z&VV	24075.9		fixed
MJ_el	24366.5 ± 1232.69	5.05%	3.874
MJ_mu	35528.5 ± 921.27	2.58%	8.746

ggF Res WZ2bWCR

Sample	Yield	R.U.	SF
Top&W	71236.5 ± 688.74	0.97%	1.031
Z&VV	518.5		fixed
MJ_el	595.63 ± 449.34	75.44%	0.094
MJ_mu	1196.9 ± 222.13	18.56%	0.294

VBF Res WWWCR

Sample	Yield	R.U.	SF
Top&W	19032.3 ± 364.43	1.91%	0.928
Z&VV	1091.63		fixed
MJ_el	1425.73 ± 214.42	15.03%	0.235
MJ_mu	1281.36 ± 157.21	11.83%	0.314

VBF Res WZWCR

Sample	Yield	R.U.	SF
Top&W	21341.8 ± 392.21	1.84%	0.942
Z&VV	1111.75		fixed
MJ_el	1413.76 ± 230.36	16.29%	0.225
MJ_mu	1281.36 ± 157.21	12.27%	0.314

Table 9.5: Fit validation result in WCRs for 2015+16 data. The fit is done in various WCRs, in order to obtain the corresponding scale factors for MJ templates: ggF resolved WCR for the $WW \rightarrow lvqq$ selection, ggF resolved untagged WCR for the $WZ \rightarrow lvqq$ selection, ggF resolved tagged WCR for the $WZ \rightarrow lvqq$ selection, VBF resolved WCR for the $WW \rightarrow lvqq$ selection, and VBF resolved WCR for the $WZ \rightarrow lvqq$ selection. Post-fit event yields for electroweak processes and MJ contributions are shown. The SF column shows the corresponding normalization scale factors for electroweak processes from the fit. R.U. stands for relative uncertainty.

1056 **Chapter 10**

1057 **Systematic Uncertainties**

1058 This section describes the sources of systematic uncertainties considered in
1059 this analysis. These uncertainties are divided into three categories: experimental
1060 uncertainties, background modeling uncertainties, and theoretical uncertainties on
1061 signal processes. In the statistical analysis each systematic uncertainty is treated
1062 as a nuisance parameter estimated on the m_{VV} distribution.

1063 **10.1 Experimental Systematics**

1064 The uncertainty on the integrated luminosity of the dataset used is 1.7% and
1065 a systematic in the final fit. This uncertainty was calculated using $x - y$ beam
1066 separation scans [ref P55].

1067 An additional source of systematic uncertainty is assigned to the pileup mod-
1068eling in MC samples. This ensures simulated detector response and particle re-
1069construction conditions are as similar as possible. The distribution of the average
1070 number of interactions per bunch crossing applied to simulation is called the μ pro-
1071file. The pileup modeling uncertainty is accounted for by re-weighting simulated
1072events so the average number of interactions per bunch crossing varies within its

1073 uncertainty due to systematics from vertex reconstruction [ref ATL-COM-SOFT-
1074 2015-119]. The associated re-weighting factors are propagated through the entire
1075 analysis chain to construct a systematic uncertainty on m_{VV} .

1076 The single-lepton and E_T^{miss} triggers used are not fully efficient, so scale factors
1077 are applied to simulation to more accurately model the data. These scale factors
1078 are given by the ratio of the distribution of offline objects before trigger selection
1079 and after trigger selection. The associated uncertainty on these scale factors are
1080 used in the final fit.

1081 Uncertainties on small-R jet energy scale and resolution are measured in-situ
1082 by calculating the response between data and simulation. This analysis uses a
1083 reduced set of JES and JER uncertainties (totaling 30 and 8 systematics, re-
1084 spectively). These reduced sets of systematics are calculated using a principal
1085 component analysis, yield largely uncorrelated independent systematics. These
1086 uncertainties on JES and JER account for the dependence on p_T , η , μ , flavor re-
1087 sponse and global sequential corrections. Systematic uncertainties associated with
1088 b -tagging are also considered. These systematics are evaluated as uncertainties on
1089 the scale factor which account for the difference in b -tagging efficiencies in data
1090 and MC, and the flavor dependence (between b, c, and light jets).

1091 The uncertainty on the p_T scale of the large-R jets is determined by comparing
1092 the jet's p_T^{calo} to p_T^{track} in di-jet simulation and data. In addition to this uncertain-
1093 ties from tracking, modeling (Pythia vs Herwig), and statistical constraints are
1094 also calculated. The large-R jet p_T resolution is given by smearing the jet p_T with
1095 a Gaussian with a 2% width.

1096 The W/Z tagging efficiency SF is estimated by comparing the tagging effi-
1097 ciency in simulation with that in data for four regions of the W/Z tagger (D_2 fail,
1098 m_J fail; D_2 pass, m_J fail; D_2 fail, m_J pass; D_2 pass, m_J pass). (Additionally,

1099 separate scale factors are determined for events with large-R jets from W bosons
 1100 and top backgrounds.) A simultaneous template fit is used to fit the signal jets
 1101 (jets initiated by W/Z bosons or top quarks) and background jets (all other jets
 1102 from the simulated backgrounds) to the data in the four regions. using the m_J
 1103 distributions. The SF for a given region is then given by:

$$SF = \frac{\epsilon_{data} = \frac{N_{fitted-signals}^{region}}{N_{all-regions}^{fitted-signals}}}{\epsilon_{MC} = \frac{N_{signal}^{region}}{N_{signal}^{all-regions}}} \quad (10.1)$$

1104 The effects of experimental and theoretical uncertainties on the efficiency scale
 1105 factor are determined by taking the ratio of efficiencies in data and simulation.
 1106 By taking this ratio the uncertainties not arising for jet mass and D_2 cancel.

1107 Lepton identification, reconstruction, isolation systematic uncertainties are de-
 1108 termined by reconstructing the Z mass peak with a tag and probe method. The
 1109 lepton energy and momentum scales are also measured with the Z mass peak.

1110 As E_T^{miss} is calculated using all the physics objects in the event, all those objects
 1111 associated errors result in an uncertainty on E_T^{miss} . Additionally, the unassociated
 1112 tracks used to construct E_T^{miss} contribute to the uncertainty on E_T^{miss} .

1113 10.2 Theory Systematics

1114 Theoretical uncertainties for signal and background processes arise from un-
 1115 certainties in the parameters used in Monte Carlo simulation. In particular for
 1116 the $t\bar{t}$, $W/Z+jets$, diboson backgrounds and signal samples, the QCD scale, PDF,
 1117 generator and hadronization uncertainties were evaluated. To assess the QCD
 1118 scale uncertainty the renormalization and factorization scales were scaled up and
 1119 down by a factor of two at the event generation stage of sample production. Un-

certainties due to the choice of the parton distribution functions were evaluated by re-weighting samples from the nominal PDF to a set of error PDFs which account for the uncertainty of the fits used to produce the PDF set. In addition to this, samples are re-weighted to different PDF sets to account for the arbitrariness of the PDF choice. The difference between the m_{WV} distributions using different event generators is assessed by comparing samples generated with different generators. Similarly, the uncertainty in hadronization models is accounted for by comparing samples created using different hadronization models (e.g. $t\bar{t}$ Powheg is compared to AMC@NLO, $W + jets$ compares Sherpa and MadGraph+Pythia samples). Figures 10.2 - 10.8 show the impact of these uncertainties on the $t\bar{t}$ and $W/Z + jets$ backgrounds. Additionally, contributions to the diboson background for the VBF analysis were found to be small and were accounted for by including a 5(10)% systematic in the diboson normalization in the final fit.

The normalization of the $t\bar{t}$ and $W+jets$ processes impact the multijet template shape. The impact of these normalizations was assessed by including a shape systematic on the multijet background from varying the $t\bar{t}$ and $W+jets$ normalization factors.

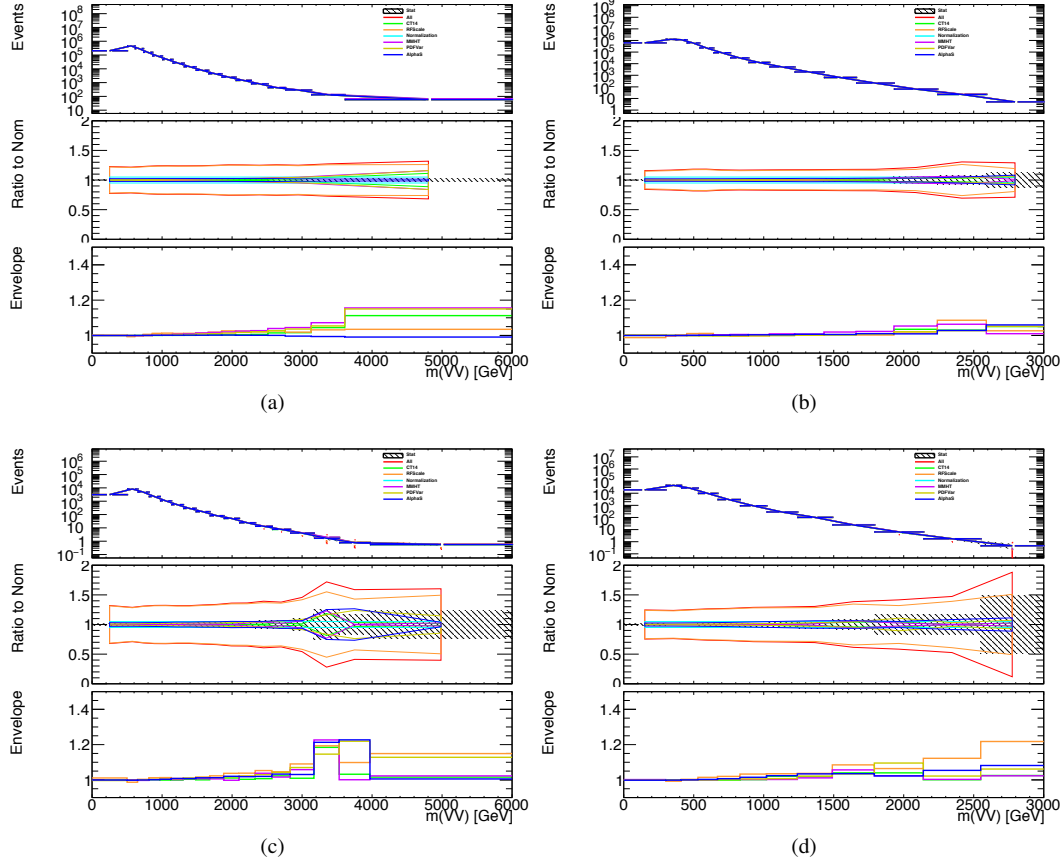


Figure 10.1: The $W/Z + \text{jet}$ systematics for the a) Merged ggF, b) Resolved ggF, c) Merged VBF, and d) Resolved VBF regions. The top subplot shows the nominal and variation distributions/bands, the middle shows the ratio of the two, and the final shows just the shape of the envelope (the final uncertainty).

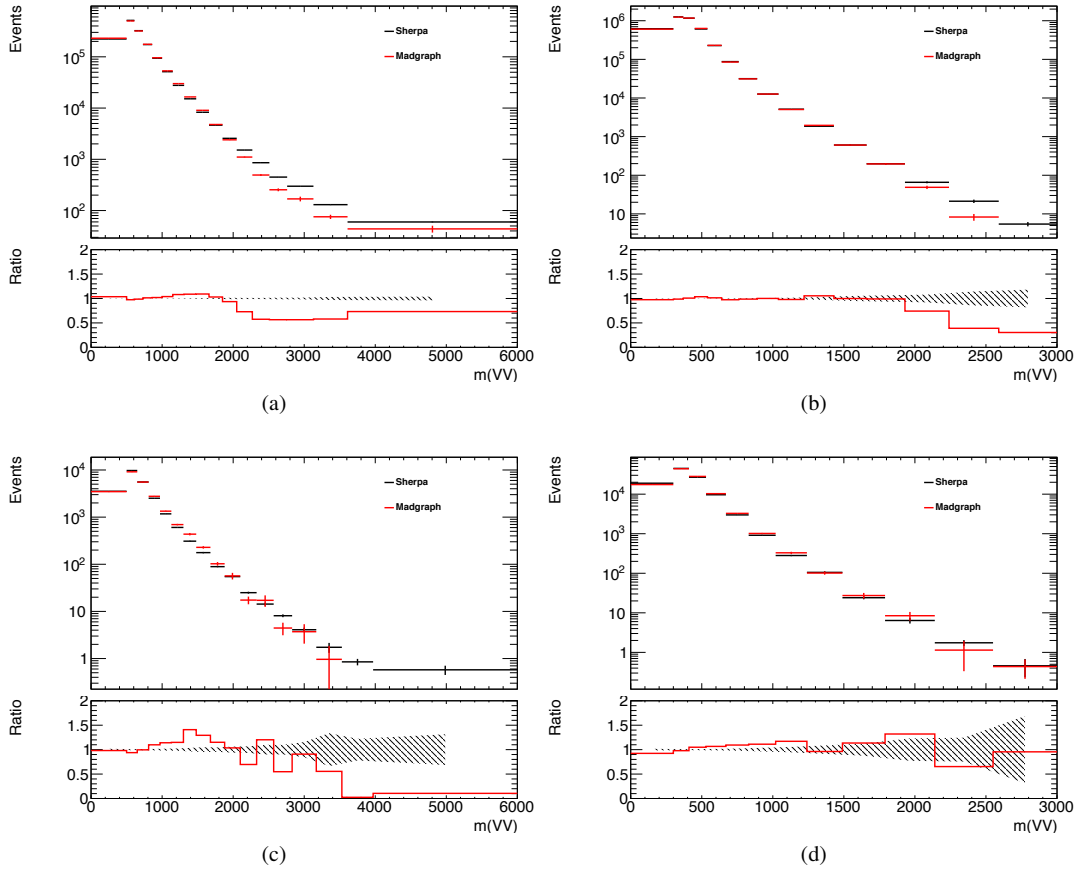


Figure 10.2: The two-point generator comparison between Sherpa and MadGraph for the $W/Z + \text{jet}$ samples in the a) Merged ggF, b) Resolved ggF, c) Merged VBF, and d) Resolved VBF regions. The normalization of the Madgraph sample is set to the Sherpa value to consider only shape effects. The bottom inset shows the ratio of the two.

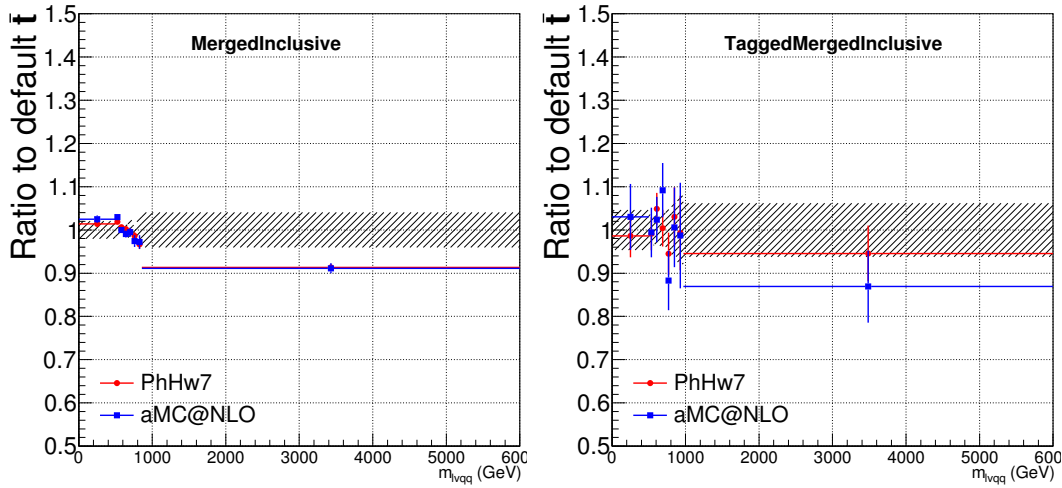


Figure 10.3: Ratio between the variations of generator (red) and hadronization (blue) variations for the Merged regime for $t\bar{t}$ sample.

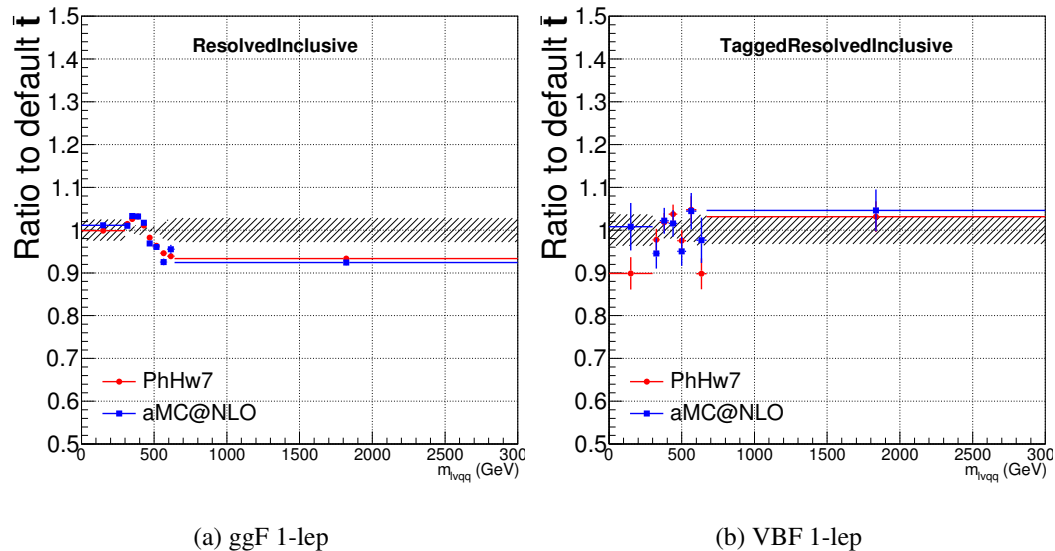


Figure 10.4: Ratio between the variations of generator (red) and hadronization (blue) variations for the Resolved regime for $t\bar{t}$ sample.

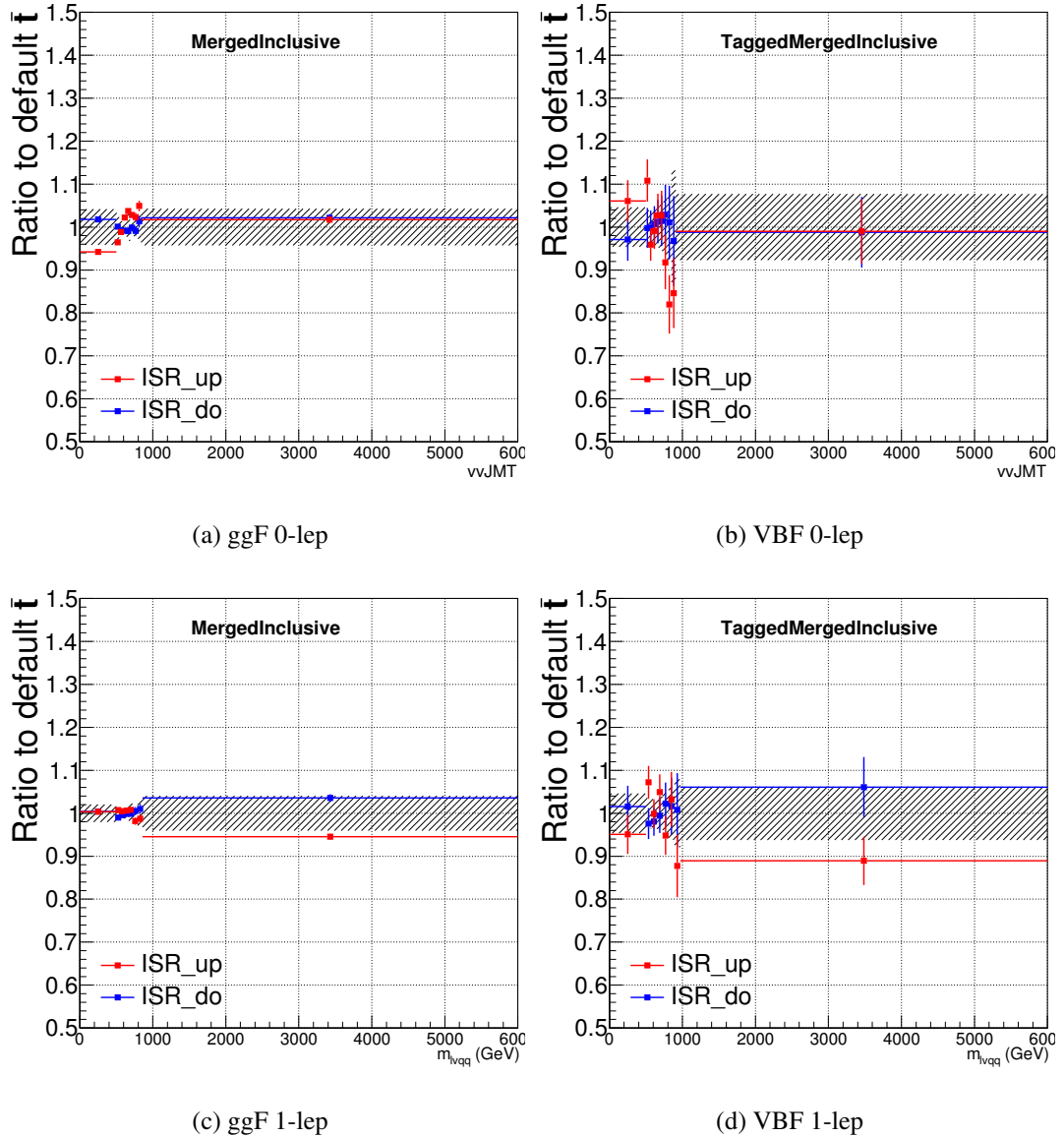


Figure 10.5: Ratio between the variations of ISR up (red) and down (blue) variations for the Merged regime for $t\bar{t}$ sample.

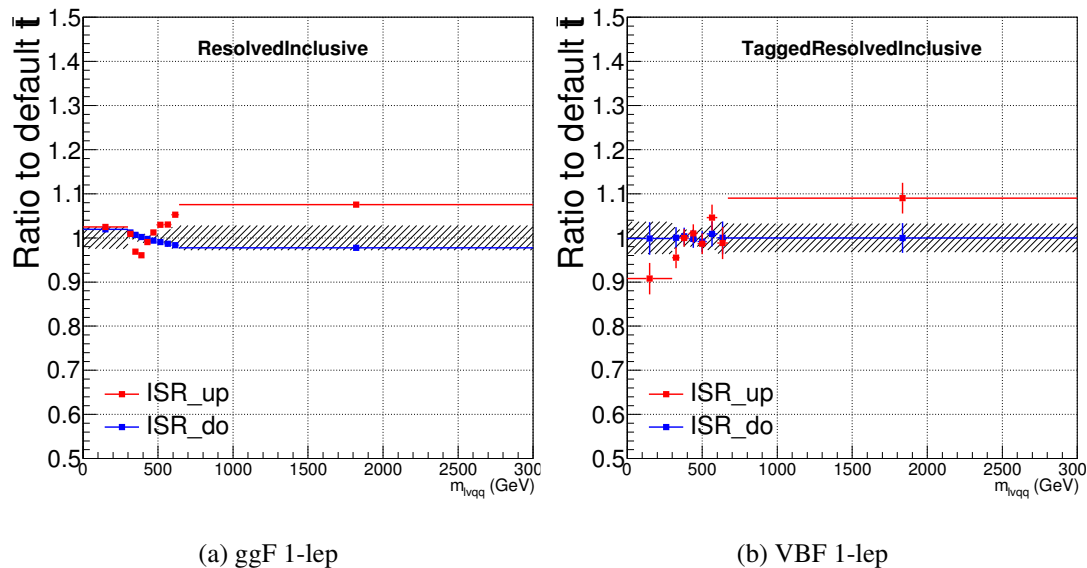


Figure 10.6: Ratio between the variations of ISR up (red) and down (blue) variations for the Resolved regime for $t\bar{t}$ sample.

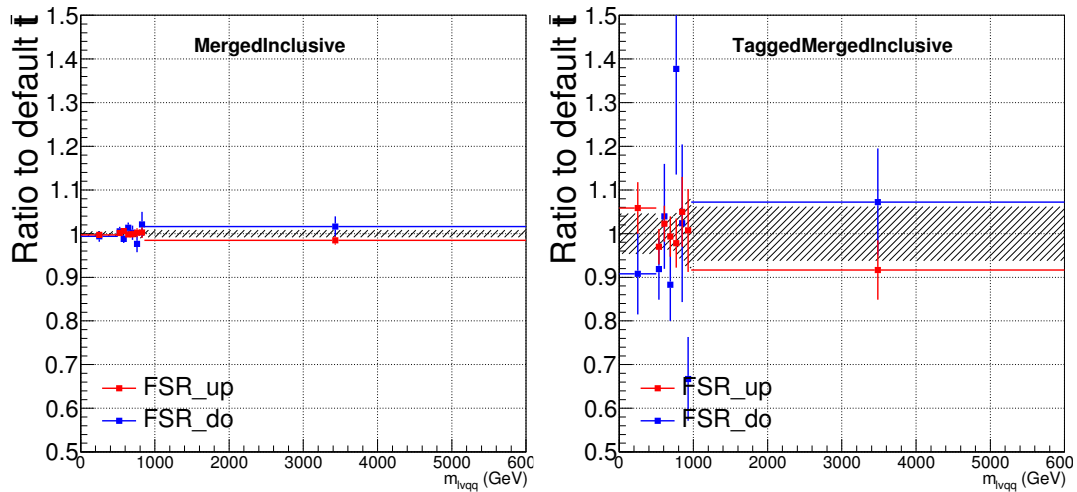


Figure 10.7: Ratio between the variations of FSR up (red) and down (blue) variations for the Merged regime for $t\bar{t}$ sample.

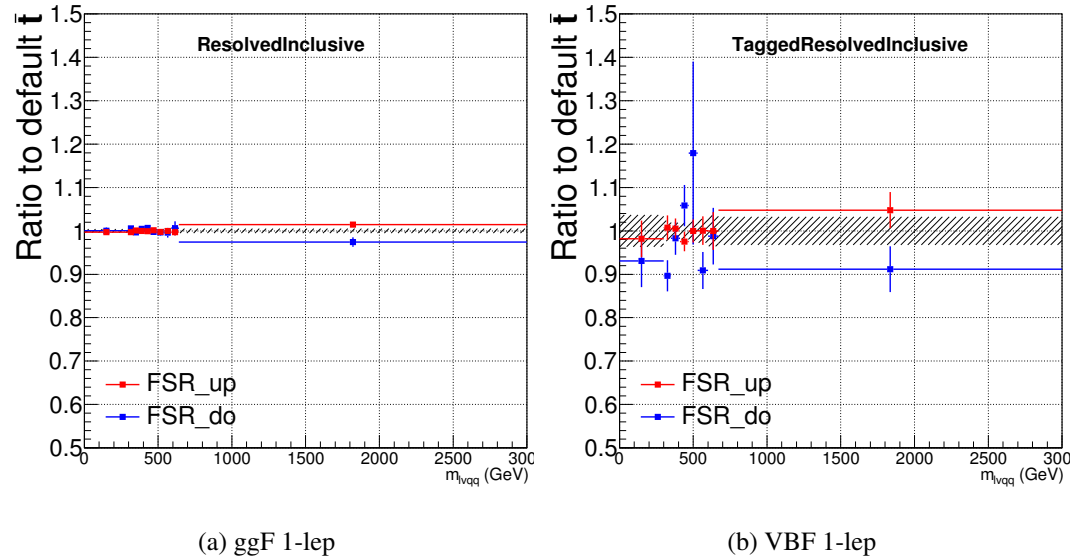


Figure 10.8: Ratio between the variations of FSR up (red) and down (blue) variations for the Resolved regime for $t\bar{t}$ sample.

₁₁₃₇ **Chapter 11**

₁₁₃₈ **Statistical Analysis**

₁₁₃₉ To determine the compatibility of the data collected with the proposed reso-
₁₁₄₀ nances a statistical procedure based on a likelihood function is used. A discovery
₁₁₄₁ test is used to measure the compatibility of the observed data with the back-
₁₁₄₂ ground only hypothesis. If the observed data is sufficiently incompatible with the
₁₁₄₃ background only hypothesis, this could indicate a discovery. In the absence of
₁₁₄₄ discovery, upper limits on the signal strength parameter, μ , are assessed using the
₁₁₄₅ CLs method.

₁₁₄₆ **11.1 Likelihood Function Definition**

₁₁₄₇ The likelihood function is product of Poisson probabilities for all analysis bins
₁₁₄₈ and systematic constraints:

$$\mathcal{L}(\mu, \boldsymbol{\theta}) = \prod_c \prod_i \frac{(\mu s_{ci}(\boldsymbol{\theta}) + b_{ci}(\boldsymbol{\theta}))^{n_{ci}}}{n_{ci}!} e^{-(\mu s_{ci}(\boldsymbol{\theta}) + b_{ci}(\boldsymbol{\theta}))} \prod_k (\theta'_k | \theta_k) \quad (11.1)$$

₁₁₄₉ Here c are the analysis channels considered and i runs over all the $m_{\ell\nu qq}$ bins

1150 used in the fit. The signal strength parameter, μ , multiplies the expected signal
1151 yield in each analysis bin, s_{ci} . The background content for channel c and bin i is
1152 given by b_{ci} . The dependence of signal and background predictions on system-
1153 atic uncertainties is described by the aforementioned set of nuisance parameters
1154 $\boldsymbol{\theta}$, which are parameterized by Gaussian or log-normal priors denoted here as
1155 θ_k . Statistical uncertainties of the simulated bin contents are also included as
1156 systematic uncertainties. Most systematics are correlated among all the analysis
1157 regions and considered to be independent from each other. The validity of this
1158 assumption is checked by evaluating the covariance of nuisance parameters.

1159 11.2 Fit Configuration

1160 The binning of $m_{\ell\nu qq}$ in signal regions for likelihood fit is determined by the
1161 statistical uncertainty of signal mass width. For each signal mass point, the signal
1162 mass resolution is given by the fitted Gaussian width of the $m_{\ell\nu qq}$. The fitted
1163 signal widths are then fit to a line to give a parameterized signal mass width, as
1164 shown in Figures 11.1 and 11.2. Bin widths are set first to this parameterized
1165 signal mass resolution. Then if the statistical uncertainty of the data or simulated
1166 background is more than 50%, bins are merged until the statistical uncertainty is
1167 less than 50%. All control regions contain only a single bin.

1168 For this analysis, each signal model is fit in the Merged and Resolved chan-
1169 nels for the relevant signal production mode simultaneously. The $W + \text{jets}$ and $t\bar{t}$
1170 normalizations are given by the best fit values in the overall fit and these fitted
1171 normalizations are then applied to those backgrounds in the SRs.

1172 Systematics may be affected by low statistics, leading to unsmooth m_{VV} dis-
1173 tributions with unphysically large fluctuations. This can lead to artificial pulls
1174 and constraints in the fit. To remove such issues a multi-step smoothing pro-

1175 cedure is applied to all systematic variation distributions in all regions. First,
1176 distributions are rebinned until the statistical error per bin is at least 5%. Next
1177 all local extrema are identified. The bins around smallest extrema are iteratively
1178 merged until only four local extrema remain. Then distributions are rebinned so
1179 that statistical uncertainties in each bin are $< 5\%$.

1180 For some systematics, up and down variations may be in the same direction
1181 with respect to the nominal distributions. This causes the variations to not cover
1182 the nominal choice, and the interpretation of the confidence interval is skewed as
1183 the nominal distribution should be bracketed by the up and down variations. This
1184 asymmetry may also lead to unconstrained systematics in the fit. To handle such
1185 asymmetric systematics, if the up and down variation for a given systematic are in
1186 the same direction for at least three m_{VV} bins the variation is averaged for those
1187 bins. The averaging procedure replaces bin-by-bin the up and down variation bins
1188 by $b_{\pm}^{new} = b_{nom} \pm \frac{|b_+ - b_-|}{2}$, where b_{nom} is the nominal bin content and b_{\pm} are the
1189 original up and down variation bin content. The same procedure is also applied to
1190 any variations where the integral of the difference between the up/down variation
1191 and the nominal distribution is twice that of the other down/up variation, further
1192 ensuring variations are symmetric around the nominal distribution.

1193 Finally, systematics that have a negligible effect on the m_{VV} distribution are
1194 not considered in the fit. Shape systematics where no bin in the variational dis-
1195 tribution deviates more than 1% from the nominal distribution (after normalizing
1196 all histograms to the nominal) are not included in the fit. Also, statistical bin
1197 uncertainties $< 1\%$ are ignored.

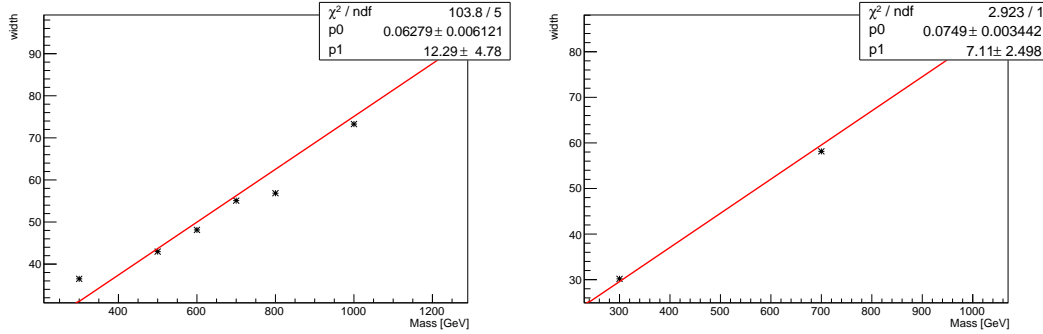


Figure 11.1: The HVT signal mass resolution as a function of mass fit with a straight line in the Resolved ggF region (left) and VBF (right) region.

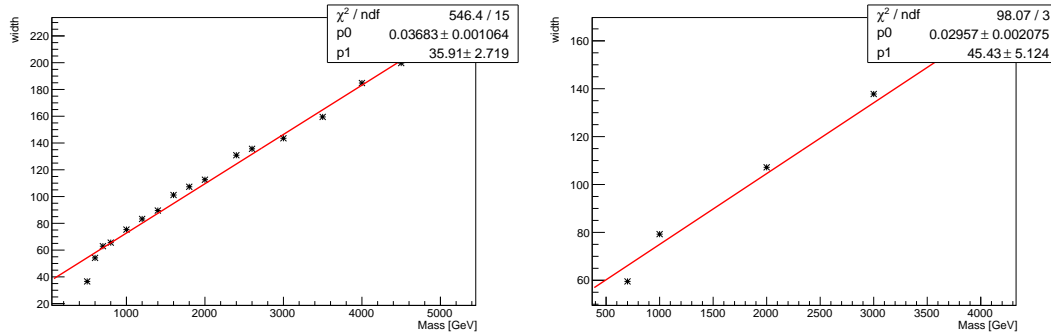


Figure 11.2: The HVT signal mass resolution as a function of mass fit with a straight line in the Merged ggF region (left) and VBF (right) region.

1198 11.3 Best Fit μ

1199 The best fit signal strength parameter is denoted by $\hat{\mu}$ and calculated by
 1200 maximizing the likelihood function with respect to all systematics and μ . The
 1201 corresponding set of systematics that maximize the likelihood are given by $\hat{\mu}$.
 1202 The first term in the likelihood is maximized when the expected number of signal
 1203 and background events is equal to the number of events in data ($n_{ci} = \mu s_{ci} +$
 1204 b_{ci}). Thus, by maximizing the likelihood, the fit determines values of μ and θ
 1205 that give the best agreement between expected and measured event yields. The

1206 second term in the likelihood is a penalty term which decreases the likelihood
1207 when systematics are shifted from their nominal values. This prevents the fit
1208 from profiling systematics in unphysical ways to maximize the likelihood. The
1209 uncertainty on μ is calculated by varying μ up and down until the natural log of
1210 the likelihood function shifts by one-half.

1211 11.4 Discovery Test

1212 To determine if the observed dataset is consistent with tested signal model a
1213 likelihood ratio is constructed:

$$\lambda(\mu) = \frac{\mathcal{L}(\mu, \hat{\theta}_\mu)}{\mathcal{L}(\hat{\mu}, \hat{\theta})} \quad (11.2)$$

1214 The denominator in this equation is the maximized value of \mathcal{L} over all system-
1215 atics and μ . The numerator is the maximized likelihood over all systematics for
1216 a given μ value, where the maximized systematics are given by $\hat{\mu}_\mu$. To test for
1217 the existence of signal the observed dataset the null hypothesis (H_0) is defined as
1218 the background only hypothesis and the alternate hypothesis includes signal and
1219 background (H_1). This test quantifies the compatibility of observed data with
1220 H_0 by calculating a p-value representing the probability of observing data as dis-
1221 crepant or more than the observed data under the H_0 . The test statistic used to
1222 calculate this p-value is given by (r_0):

$$r_0 = \begin{cases} -2 \ln \lambda(0), \hat{\mu} > 0 \\ +2 \ln \lambda(0), \hat{\mu} < 0 \end{cases} \quad (11.3)$$

1223 The expected distribution of the the test statistic under H_0 ($f(r_0|0)$) is used to
1224 calculate the p-value:

$$p_0 = \int_{r_0, obs}^{\infty} f(r_0 | 0) dr_0 \quad (11.4)$$

1225 Small p-values indicate the observed data is poorly described by H_0 . This
 1226 equivalent Z-score of a given p-value is usually used to further quantify the agree-
 1227 ment between the observed data and H_0 . The Z-score is given by the number of
 1228 standard deviations away from the mean of a Gaussian distribution, the integral
 1229 of the upper tail of the distribution would equal the p-value. Mathematically:

$$Z = \Phi^{-1}(1 - p_0) \quad (11.5)$$

1230 where Φ is the Gaussian cumulative distribution function. The statistical
 1231 significance of these tests are expressed as the Z -score. In particle physics, 3σ is
 1232 considered evidence for new phenomena and 5σ is the threshold for discovery.

1233 11.5 Exclusion Limits

1234 In the absence of discovery, upper limits on the signal strength, μ are set using
 1235 the CLs method [cite P60]. The test statistic for this test, q_μ , is constructed as:

$$\tilde{\lambda}_\mu = \begin{cases} \frac{\mathcal{L}(\mu, \hat{\theta}_\mu)}{\mathcal{L}(\hat{\mu}, \hat{\theta})}, \hat{\mu} > 0 \\ \frac{\mathcal{L}(\mu, \hat{\theta}_\mu)}{\mathcal{L}(0, \hat{\theta}_0)}, \hat{\mu} < 0 \end{cases} \quad (11.6)$$

$$\tilde{q}_\mu = \begin{cases} -2 \ln \tilde{\lambda}(\mu), \hat{\mu} < \mu \\ +2 \ln \tilde{\lambda}(\mu), \hat{\mu} > \mu \end{cases} \quad (11.7)$$

1236 As defined, larger values of q_μ correspond to increasing incompatibility between
 1237 the observed data and the background + signal hypothesis. The observed value
 1238 of the test statistic, $q_{\mu, obs}$, is then compared to its expected distribution, f , to

1239 calculate p-values to assess the likelihood of the background+signal hypothesis.

1240 Using these distributions, CL_s values are computed as:

$$CL_{s+b} = \int_{q_{\mu,obs}}^{\infty} f(q_{\mu}|\mu) dq_{\mu} \quad (11.8)$$

1241

$$CL_b = \int_{q_0^{obs}}^{\infty} f(q_{\mu}|\mu = 0) dq_{\mu} \quad (11.9)$$

1242

$$CL_s = \frac{CL_{s+b}}{CL_b} \quad (11.10)$$

1243 CL_{s+b} is the p-value for the signal + background hypothesis and CL_b is the
1244 p-value for the background only hypothesis. The CL_s value is interpreted as
1245 the probability to observe the background + signal hypothesis normalized to the
1246 probability of background-only hypothesis. Normalizing by CL_b prevents setting
1247 artificially strong exclusion limits due to downward fluctuations in data.

1248 For a given signal hypothesis, μ values are scanned simultaneously over all
1249 m_{WV} bins to find the μ value that yields $CL_s=0.05$, meaning the likelihood of
1250 finding data more incompatible with the signal+background hypothesis (relative
1251 to the background only hypothesis) is 5%. The 95% upper limit on the cross
1252 section is then calculated as the product of the μ value found, branching ratio,
1253 and theory cross section.

Part V

1254

Results

1255

126

1256 **Chapter 12**

1257 **Statistical Interpretation**

1258 **12.1 Discovery Tests**

1259 To test for the existence of signal in the observed dataset, the discovery tests
1260 discussed earlier are used to calculate p-values as a function of resonance mass.
1261 The results of these tests are shown in Figures 12.1 - 12.5. Across the different
1262 DY signals the largest excesses are $\sim 2.2\sigma$ at 600 GeV and 1.8σ at 2 TeV. The
1263 largest excesses for VBF signals are $< 2.5\sigma$ at for 1 TeV resonances. As these
1264 deviations do not constitute discoveries, upper limits on μ are calculated.

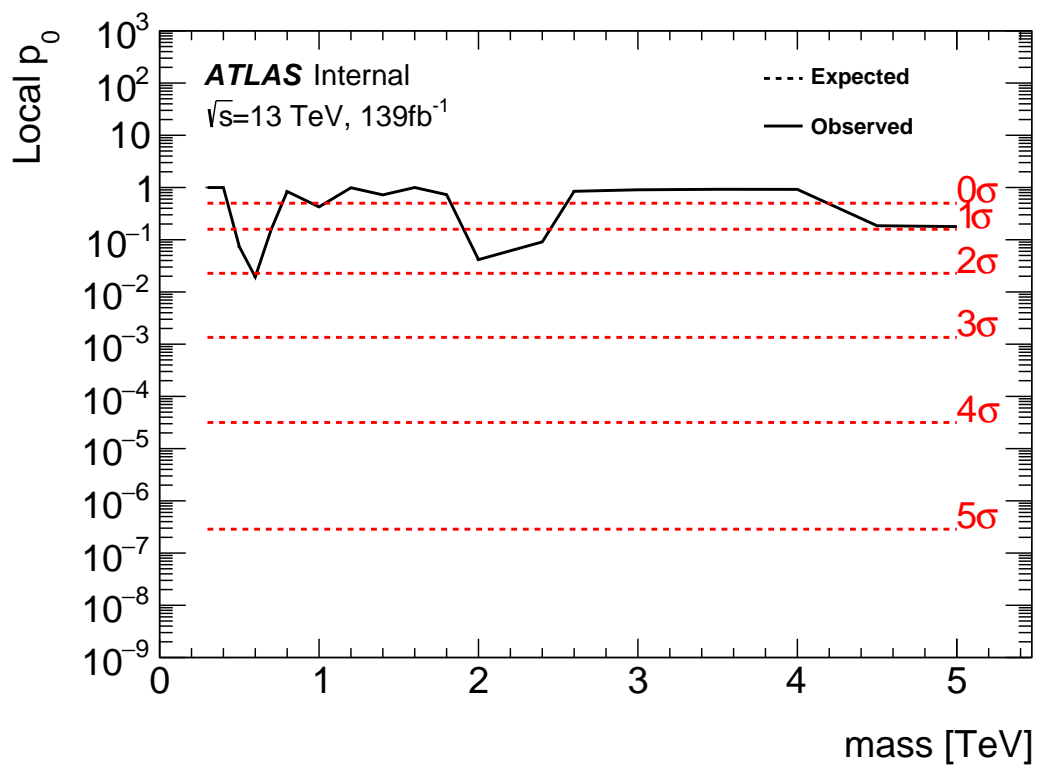


Figure 12.1: These plots show the measured p_0 value as a function of resonance mass for HVT Z' DY production.

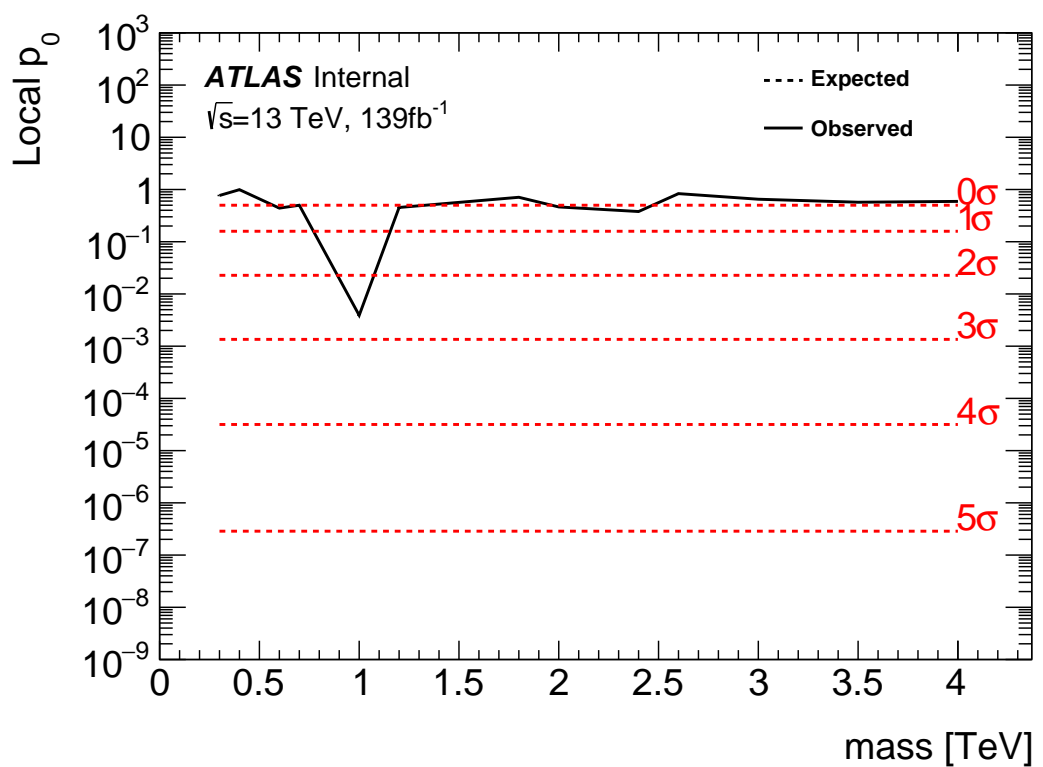


Figure 12.2: These plots show the measured p_0 value as a function of resonance mass for HVT Z' VBF production.

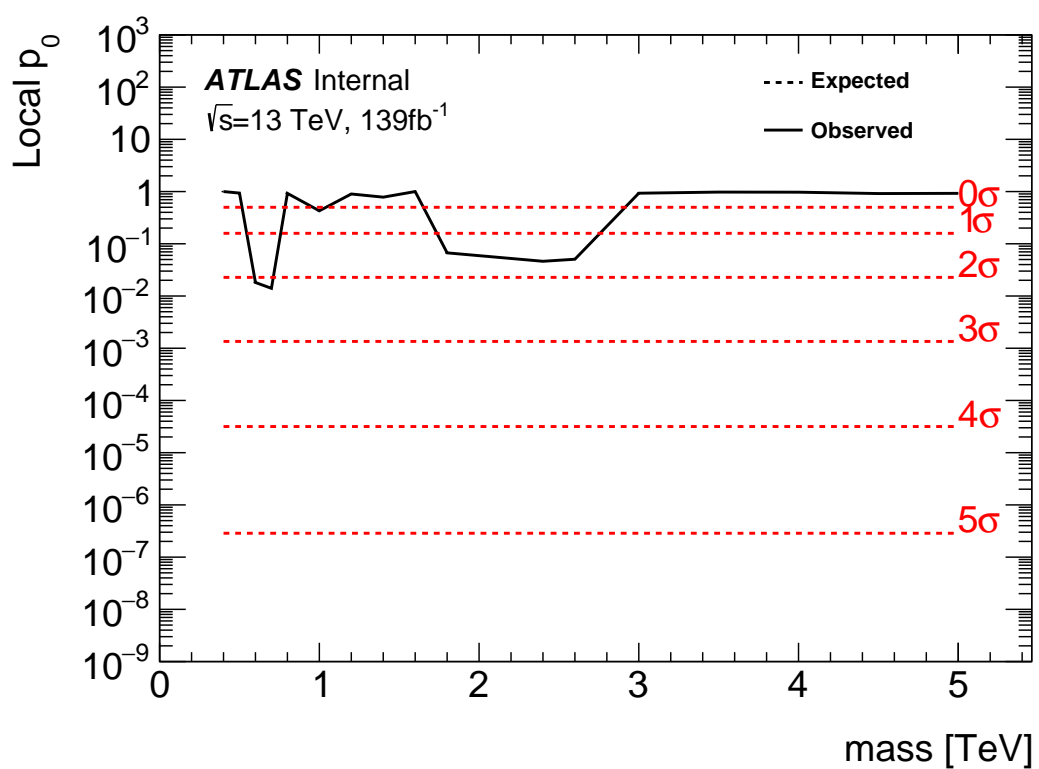


Figure 12.3: These plots show the measured p_0 value as a function of resonance mass for HVT W' DY production.

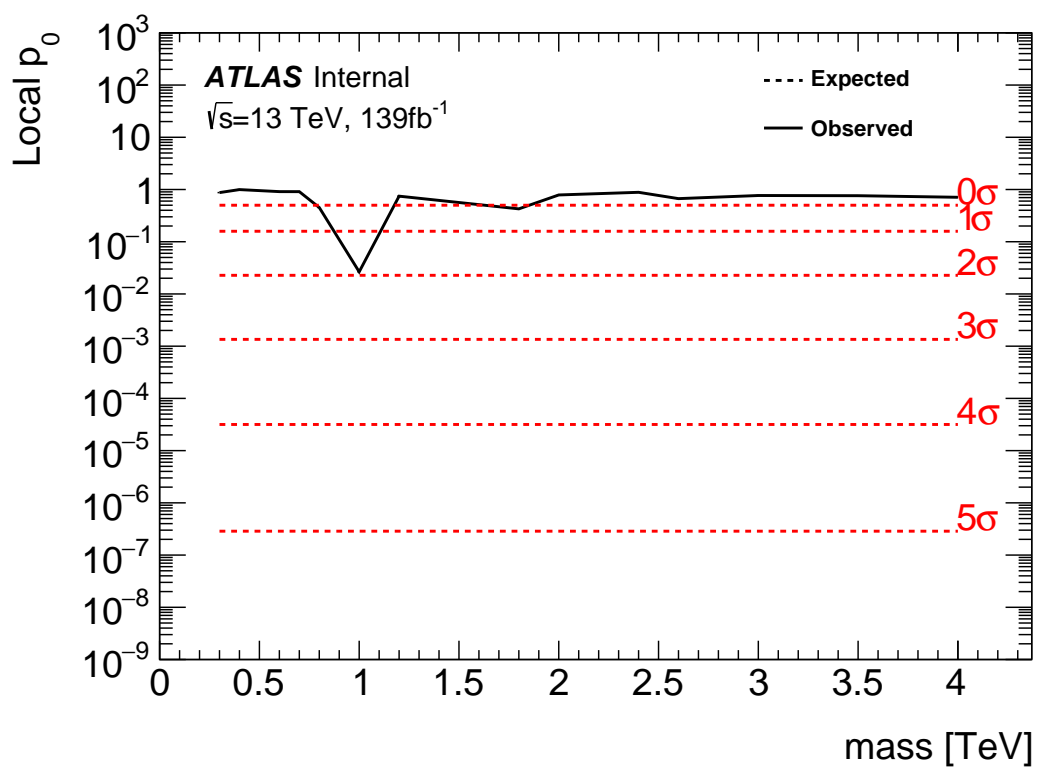


Figure 12.4: These plots show the measured p_0 value as a function of resonance mass for HVT W' VBF production.

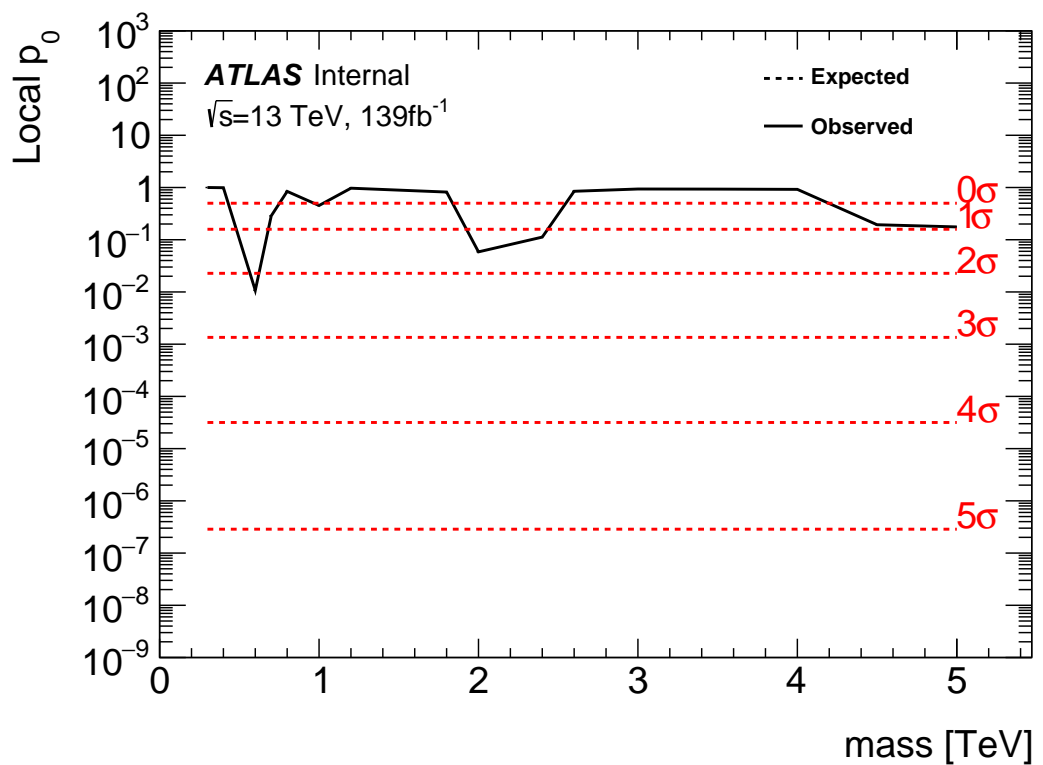


Figure 12.5: These plots show the measured p_0 value as a function of resonance mass for the RS Graviton DY production.

1265 12.2 Systematic Profiling and Correlations

1266 The ranked systematics and their fitted values are shown for the different anal-
 1267 ysis regions in Figure 12.6 - 12.8. Note that background normalizations for $W+jets$
 1268 and $t\bar{t}$ are left free to float in the fit. This means the nominal normalization val-
 1269 ues are at one and the uncertainties are not plotted in the ranked plots. Overall,
 1270 systematics are not pulled outside their uncertainties, especially for highly ranked
 1271 nuisance parameters.

1272 The correlation between systematics are shown in Figures ???. Correlations
 1273 between background normalization are expected. The remaining systematic cor-
 1274 relations are not very strong or unexpected.

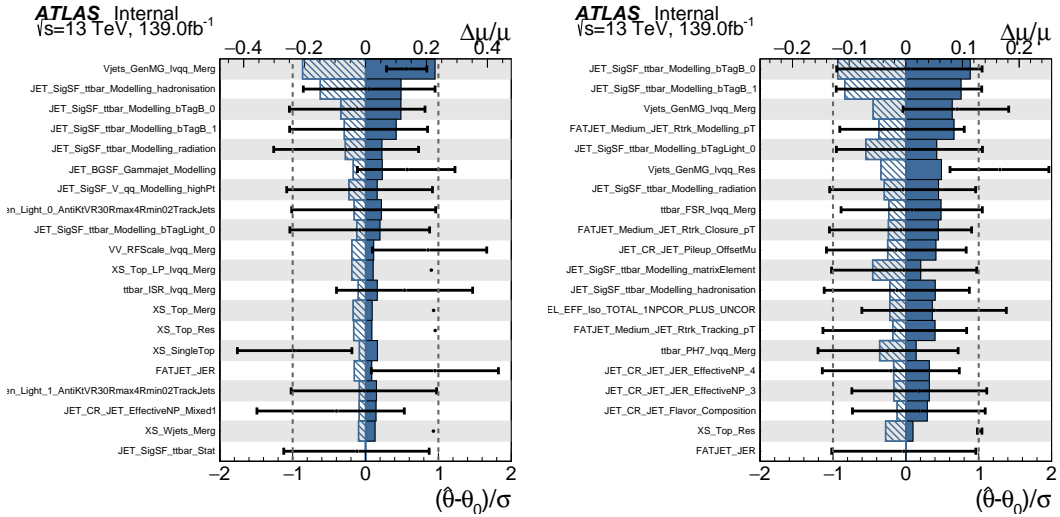


Figure 12.6: Ranked systematics and their fitted values for WW DY (right) and VBF (left) selections.

1274

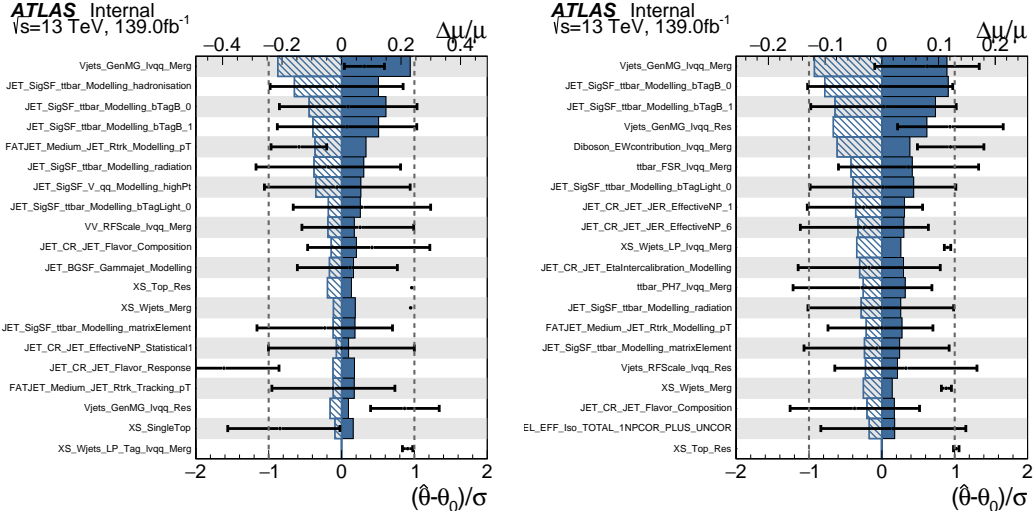


Figure 12.7: Ranked systematics and their fitted values for WZ DY (right) and VBF (left) selections.

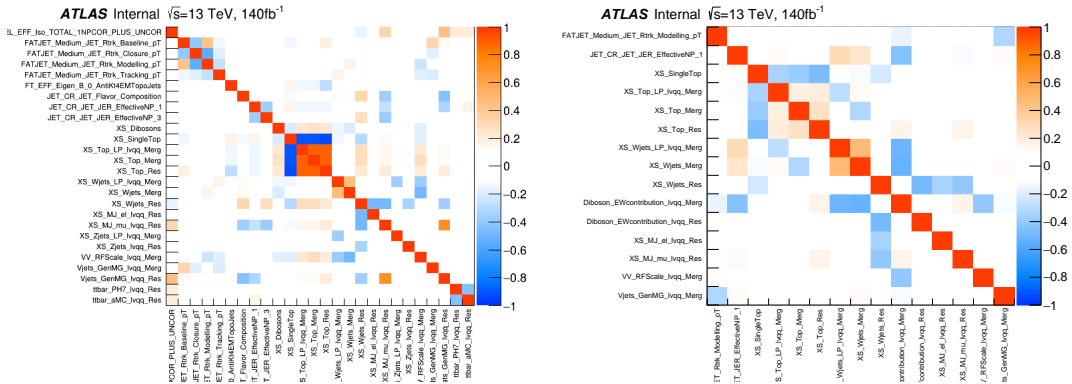


Figure 12.8: Correlations between systematics for WW DY (right) and VBF (left) selections.

12.3 Expected and Measured Yields

The yield tables for the four analysis regions are shown in Tables ?? - ?? . The fitted background normalizations are shown in Tables ??-?? . The control region $m_{\ell\nu qq}$ distributions are shown in Figures 12.9 - 12.12. The signal region $m_{\ell\nu qq}$ distributions are shown in Figures 12.13 - ?? .

	HP WCR	LP WCR	Resolved WCR
Electron Multi-jet	-	-	16507.83 ± 2314.87
Muon Multi-jet	-	-	19977.12 ± 2816.06
Diboson	1833.41 ± 177.78	3323.93 ± 320.92	9147.67 ± 961.63
Single-top	2160.62 ± 402.34	3551.09 ± 660.00	20058.36 ± 3817.26
$t\bar{t}$	15518.86 ± 338.22	24069.54 ± 453.15	138866.23 ± 1989.71
$W+jets$	40141.57 ± 357.79	88113.06 ± 487.87	673200.38 ± 4120.53
$Z+jets$	778.83 ± 78.93	1765.54 ± 179.10	16570.50 ± 1672.71
Total	60433.29 ± 664.92	120823.16 ± 1006.99	894328.12 ± 7247.12
Data	60264.00	120852.00	895362.00
	HP TCR	LP TCR	Resolved TCR
Electron Multi-jet	-	-	-
Muon Multi-jet	-	-	-
Diboson	421.11 ± 37.98	550.44 ± 53.10	996.87 ± 119.63
Single-top	4691.44 ± 846.11	3466.26 ± 631.03	16848.71 ± 3258.26
$t\bar{t}$	38945.18 ± 848.77	33836.95 ± 637.04	224226.14 ± 3212.76
$W+jets$	2258.34 ± 20.13	6564.78 ± 36.35	23466.41 ± 143.63
$Z+jets$	66.35 ± 6.72	213.26 ± 21.63	846.66 ± 85.47
Total	46382.43 ± 1199.25	44631.70 ± 899.23	266384.78 ± 4580.43
Data	46354.00	44629.00	266443.00
	WW SR	LP SR	Resolved 1-lepton SR
Electron Multi-jet	-	-	10788.40 ± 1512.85
Muon Multi-jet	-	-	15759.50 ± 2221.53
Diboson	4990.30 ± 376.50	3901.07 ± 313.22	16971.29 ± 1523.77
Single-top	3117.71 ± 565.07	2176.46 ± 400.52	20422.85 ± 3731.94
$t\bar{t}$	13785.77 ± 302.14	11005.12 ± 207.41	126965.25 ± 1819.66
$W+jets$	24718.56 ± 223.72	60080.66 ± 333.12	444133.56 ± 2719.02
$Z+jets$	478.18 ± 48.46	1226.69 ± 124.44	11686.32 ± 1179.69
Total	47090.52 ± 777.65	78389.98 ± 654.22	646727.19 ± 5963.98
Data	47330.00	78380.00	645610.00

Table 12.1: Expected and Measured for DY WW $W+jets$, $t\bar{t}$ control regions and signal regions.

	HP Untagged WCR	LP Untagged WCR	Resolved Untagged WCR
Electron Multi-jet	-	-	15080.03 ± 2277.99
Muon Multi-jet	-	-	27347.10 ± 2950.07
Diboson	1508.48 ± 154.20	2758.24 ± 284.50	9038.55 ± 728.69
Single-top	1756.59 ± 306.69	2913.18 ± 515.93	20511.74 ± 3523.47
$t\bar{t}$	13134.00 ± 238.30	21815.37 ± 334.98	140157.77 ± 2636.96
$W+jets$	40654.84 ± 333.65	87657.76 ± 501.96	665909.12 ± 4420.62
$Z+jets$	768.72 ± 77.97	1759.87 ± 178.96	16512.46 ± 1673.23
Total	57822.63 ± 540.40	116904.42 ± 862.16	894556.75 ± 7492.20
Data	57699.00	117306.00	895362.00
	HP Tagged WCR	LP Tagged WCR	Resolved Tagged WCR
Electron Multi-jet	-	-	384.58 ± 57.11
Muon Multi-jet	-	-	602.93 ± 190.12
Diboson	30.22 ± 4.69	48.95 ± 7.16	264.64 ± 28.24
Single-top	308.44 ± 56.19	371.59 ± 69.43	5752.39 ± 1029.97
$t\bar{t}$	1683.82 ± 48.73	2041.48 ± 70.00	58431.49 ± 614.30
$W+jets$	583.55 ± 75.37	1109.45 ± 85.78	11891.68 ± 903.01
$Z+jets$	13.19 ± 1.34	23.06 ± 2.34	324.74 ± 32.85
Total	2619.22 ± 106.00	3594.53 ± 130.90	77652.45 ± 1514.89
Data	2565.00	3546.00	77973.00
	HP Untagged TCR	LP Untagged TCR	Resolved Untagged TCR
Electron Multi-jet	-	-	-
Muon Multi-jet	-	-	-
Diboson	289.45 ± 28.45	346.78 ± 35.85	650.85 ± 65.56
Single-top	3107.99 ± 538.03	2250.64 ± 385.41	9606.87 ± 1698.22
$t\bar{t}$	30992.40 ± 562.33	26954.21 ± 413.89	91893.59 ± 1728.91
$W+jets$	2236.29 ± 18.35	4874.03 ± 27.91	16122.97 ± 107.03
$Z+jets$	71.54 ± 7.26	155.50 ± 15.81	577.71 ± 58.54
Total	36697.66 ± 779.03	34581.16 ± 567.59	118851.98 ± 2427.40
Data	36677.00	34573.00	118928.00
	HP Tagged TCR	LP Tagged TCR	Resolved Tagged TCR
Electron Multi-jet	-	-	-
Muon Multi-jet	-	-	-
Diboson	9.72 ± 1.13	8.75 ± 1.16	34.06 ± 4.98
Single-top	105.87 ± 20.65	119.66 ± 22.68	656.89 ± 132.96
$t\bar{t}$	1904.75 ± 50.61	1483.86 ± 47.05	17965.33 ± 188.87
$W+jets$	32.36 ± 4.28	85.74 ± 6.96	489.01 ± 37.13
$Z+jets$	1.27 ± 0.13	1.93 ± 0.20	19.14 ± 1.94
Total	2053.98 ± 54.84	1699.93 ± 52.70	19164.43 ± 234.01
Data	2047.00	1708.00	19143.00

Table 12.2: Expected and Measured for DY WZ $W+jets$, $t\bar{t}$ tag and untag control regions.

	HP Untagged SR	LP Untagged SR	Resolved Untagged SR
Electron Multi-jet	-	-	7782.17 ± 1175.56
Muon Multi-jet	-	-	17004.81 ± 1834.40
Diboson	3041.17 ± 273.77	2266.35 ± 212.79	14724.12 ± 1224.31
Single-top	2123.28 ± 373.83	1379.35 ± 240.92	18336.88 ± 3082.47
$t\bar{t}$	11678.86 ± 213.63	8906.34 ± 136.88	112669.24 ± 2122.46
$W+jets$	22741.32 ± 191.47	41726.76 ± 240.56	342934.00 ± 2280.21
$Z+jets$	442.03 ± 44.84	849.79 ± 86.42	9271.83 ± 939.52
Total	40026.65 ± 546.81	55128.59 ± 432.90	522723.03 ± 5131.71
Data	40193.00	54735.00	521813.00
	HP Tagged SR	LP Tagged SR	Resolved Tagged SR
Electron Multi-jet	-	-	199.22 ± 29.58
Muon Multi-jet	-	-	393.43 ± 124.06
Diboson	102.58 ± 11.59	65.44 ± 8.05	624.07 ± 58.10
Single-top	178.21 ± 33.62	155.53 ± 28.95	3470.39 ± 617.48
$t\bar{t}$	1017.93 ± 31.95	706.76 ± 26.20	38189.30 ± 401.91
$W+jets$	325.58 ± 41.62	575.36 ± 43.29	6161.96 ± 467.71
$Z+jets$	7.81 ± 0.80	11.62 ± 1.19	183.36 ± 18.55
Total	1632.11 ± 63.39	1514.70 ± 58.86	49221.74 ± 884.06
Data	1699.00	1559.00	48919.00

Table 12.3: Expected and Measured for DY WZ $W+jets$, $t\bar{t}$ tag and untag signal regions.

	HP WCR	LP WCR	Resolved WCR
Electron Multi-jet	-	-	898.48 ± 137.82
Muon Multi-jet	-	-	601.46 ± 182.74
Diboson	107.45 ± 45.20	166.87 ± 68.11	292.10 ± 235.29
Single-top	78.19 ± 18.22	132.71 ± 31.93	879.82 ± 216.89
$t\bar{t}$	400.71 ± 28.35	569.70 ± 48.88	5067.51 ± 155.69
$W+jets$	864.49 ± 63.44	1940.80 ± 89.41	18563.70 ± 408.99
$Z+jets$	19.51 ± 2.00	46.63 ± 4.77	795.20 ± 80.89
Total	1470.35 ± 84.89	2856.71 ± 126.74	27098.28 ± 594.01
Data	1495.00	2898.00	27120.00
	HP TCR	LP TCR	Resolved TCR
Electron Multi-jet	-	-	-
Muon Multi-jet	-	-	-
Diboson	14.95 ± 6.61	27.57 ± 14.12	24.33 ± 20.32
Single-top	68.31 ± 16.17	58.93 ± 13.56	278.60 ± 73.04
$t\bar{t}$	496.60 ± 31.72	401.23 ± 32.13	3834.49 ± 104.60
$W+jets$	50.68 ± 4.19	144.02 ± 7.86	450.01 ± 11.87
$Z+jets$	1.32 ± 0.14	5.35 ± 0.55	29.96 ± 3.07
Total	631.87 ± 36.45	637.10 ± 38.44	4617.39 ± 129.77
Data	636.00	634.00	4615.00
	HP SR	LP SR	Resolved SR
Electron Multi-jet	-	-	596.34 ± 91.52
Muon Multi-jet	-	-	481.01 ± 144.48
Diboson	148.84 ± 48.64	181.42 ± 67.30	395.52 ± 318.06
Single-top	79.49 ± 19.80	56.82 ± 14.89	782.07 ± 190.79
$t\bar{t}$	338.42 ± 24.14	236.80 ± 20.88	4261.70 ± 138.98
$W+jets$	501.13 ± 39.36	1347.76 ± 64.50	11445.73 ± 291.49
$Z+jets$	9.25 ± 0.95	28.77 ± 2.95	567.66 ± 57.94
Total	1077.13 ± 69.93	1851.57 ± 96.73	18530.03 ± 523.88
Data	1096.00	1846.00	18530.00

Table 12.4: Expected and Measured for VBF WW $W+jets$, $t\bar{t}$ control regions and signal regions.

	HP WCR	LP WCR	Resolved WCR
Electron Multi-jet	-	-	870.00 ± 132.75
Muon Multi-jet	-	-	618.45 ± 196.90
Diboson	92.92 ± 41.77	145.90 ± 64.26	228.62 ± 114.62
Single-top	71.13 ± 16.29	118.82 ± 27.98	1209.87 ± 281.64
$t\bar{t}$	427.80 ± 29.72	509.19 ± 46.57	6860.87 ± 254.83
$W+jets$	871.68 ± 64.22	2020.67 ± 93.54	19088.50 ± 442.10
$Z+jets$	19.58 ± 2.01	47.39 ± 4.85	800.19 ± 82.02
Total	1483.11 ± 83.79	2841.97 ± 125.92	29676.50 ± 644.96
Data	1495.00	2898.00	29755.00
	HP TCR	LP TCR	Resolved TCR
Electron Multi-jet	-	-	-
Muon Multi-jet	-	-	-
Diboson	10.12 ± 4.51	12.73 ± 6.55	14.23 ± 7.49
Single-top	51.57 ± 12.31	35.07 ± 8.17	169.21 ± 44.54
$t\bar{t}$	470.06 ± 28.97	298.99 ± 25.28	2414.75 ± 75.42
$W+jets$	49.64 ± 4.17	109.69 ± 6.16	378.22 ± 12.05
$Z+jets$	1.28 ± 0.13	4.81 ± 0.50	17.62 ± 1.83
Total	582.67 ± 32.07	461.30 ± 28.05	2994.03 ± 88.75
Data	584.00	459.00	3001.00
	HP SR	LP SR	Resolved SR
Electron Multi-jet	-	-	444.65 ± 67.99
Muon Multi-jet	-	-	397.29 ± 125.59
Diboson	109.66 ± 44.13	112.28 ± 46.45	265.75 ± 139.43
Single-top	63.16 ± 15.20	48.02 ± 11.56	872.16 ± 205.00
$t\bar{t}$	348.95 ± 24.34	190.68 ± 17.75	5134.25 ± 193.57
$W+jets$	467.21 ± 37.12	973.73 ± 47.91	10226.83 ± 254.67
$Z+jets$	8.15 ± 0.84	23.62 ± 2.43	558.48 ± 57.25
Total	997.13 ± 64.42	1348.33 ± 70.06	17899.41 ± 432.98
Data	1018.00	1313.00	17826.00

Table 12.5: Expected and Measured for VBF WZ $W+jets$, $t\bar{t}$ control regions and signal regions.

Background	Fitted Normalization
XS_Top_LP_lvqq_Merg_binned	$0.905^{+0.0166}_{-0.0166}$
XS_Top_Merg	$0.936^{+0.0199}_{-0.0199}$
XS_Top_Res	$0.957^{+0.0134}_{-0.0134}$
XS_Wjets_LP_lvqq_Merg_binned	$0.884^{+0.00489}_{-0.00489}$
XS_Wjets_Merg	$0.931^{+0.00831}_{-0.00831}$
XS_Wjets_Res	$1.03^{+0.00628}_{-0.00628}$

Table 12.6: Fitted background normalizations for $t\bar{t}$ and $W+jets$ backgrounds for the DY WW analysis region.

Background	Fitted Normalization
XS_Top_LP_Tag_lvqq_Merg_binned	$0.973^{+0.0333}_{-0.0333}$
XS_Top_LP_lvqq_Merg_binned	$0.894^{+0.0135}_{-0.0135}$
XS_Top_Merg	$0.893^{+0.016}_{-0.016}$
XS_Top_Res	$0.965^{+0.0179}_{-0.0179}$
XS_Top_Tag_lvqq_Merg_binned	$0.954^{+0.0276}_{-0.0276}$
XS_Top_Tag_lvqq_Res_binned	$0.999^{+0.0105}_{-0.0105}$
XS_Wjets_LP_Tag_lvqq_Merg_binned	$0.912^{+0.0703}_{-0.0703}$
XS_Wjets_LP_lvqq_Merg_binned	$0.876^{+0.00502}_{-0.00502}$
XS_Wjets_Merg	$0.948^{+0.00779}_{-0.00779}$
XS_Wjets_Res	$1.01^{+0.00673}_{-0.00673}$
XS_Wjets_Tag_lvqq_Merg_binned	$0.906^{+0.117}_{-0.117}$
XS_Wjets_Tag_lvqq_Res_binned	$1.2^{+0.0904}_{-0.0904}$

Table 12.7: Fitted background normalizations for $t\bar{t}$ and $W+jets$ backgrounds for the DY WZ analysis region.

Background	Fitted Normalization
XS_Top_LP_lvqq_Merg_binned	$0.79^{+0.0673}_{-0.0673}$
XS_Top_Merg	$0.888^{+0.061}_{-0.061}$
XS_Top_Res	$1.01^{+0.0311}_{-0.0311}$
XS_Wjets_LP_lvqq_Merg_binned	$0.88^{+0.0423}_{-0.0423}$
XS_Wjets_Merg	$0.881^{+0.0677}_{-0.0677}$
XS_Wjets_Res	$0.932^{+0.0202}_{-0.0202}$

Table 12.8: Fitted background normalizations for $t\bar{t}$ and $W+jets$ backgrounds for the VBF WW analysis region.

Background	Fitted Normalization
XS_Top_LP_lvqq_Merg_binned	$0.708^{+0.064}_{-0.064}$
XS_Top_Merg	$0.958^{+0.0644}_{-0.0644}$
XS_Top_Res	$1.02^{+0.038}_{-0.038}$
XS_Wjets_LP_lvqq_Merg_binned	$0.9^{+0.0438}_{-0.0438}$
XS_Wjets_Merg	$0.883^{+0.0685}_{-0.0685}$
XS_Wjets_Res	$0.945^{+0.0219}_{-0.0219}$

Table 12.9: Fitted background normalizations for $t\bar{t}$ and $W+jets$ backgrounds for the VBF WZ analysis region.

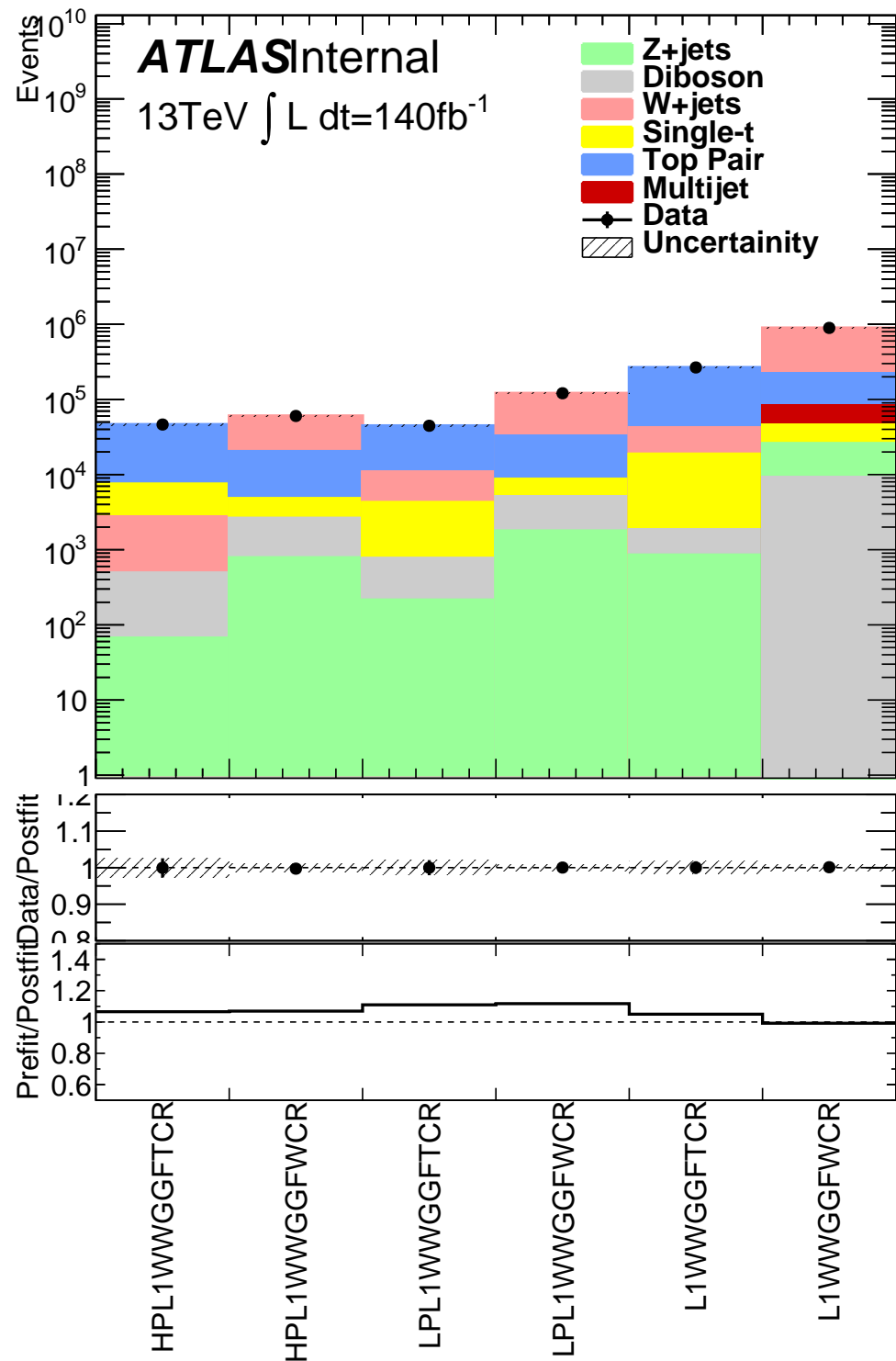


Figure 12.9: This figure shows the distribution of $m_{\ell\nu qq}$ in the DY WW control regions.

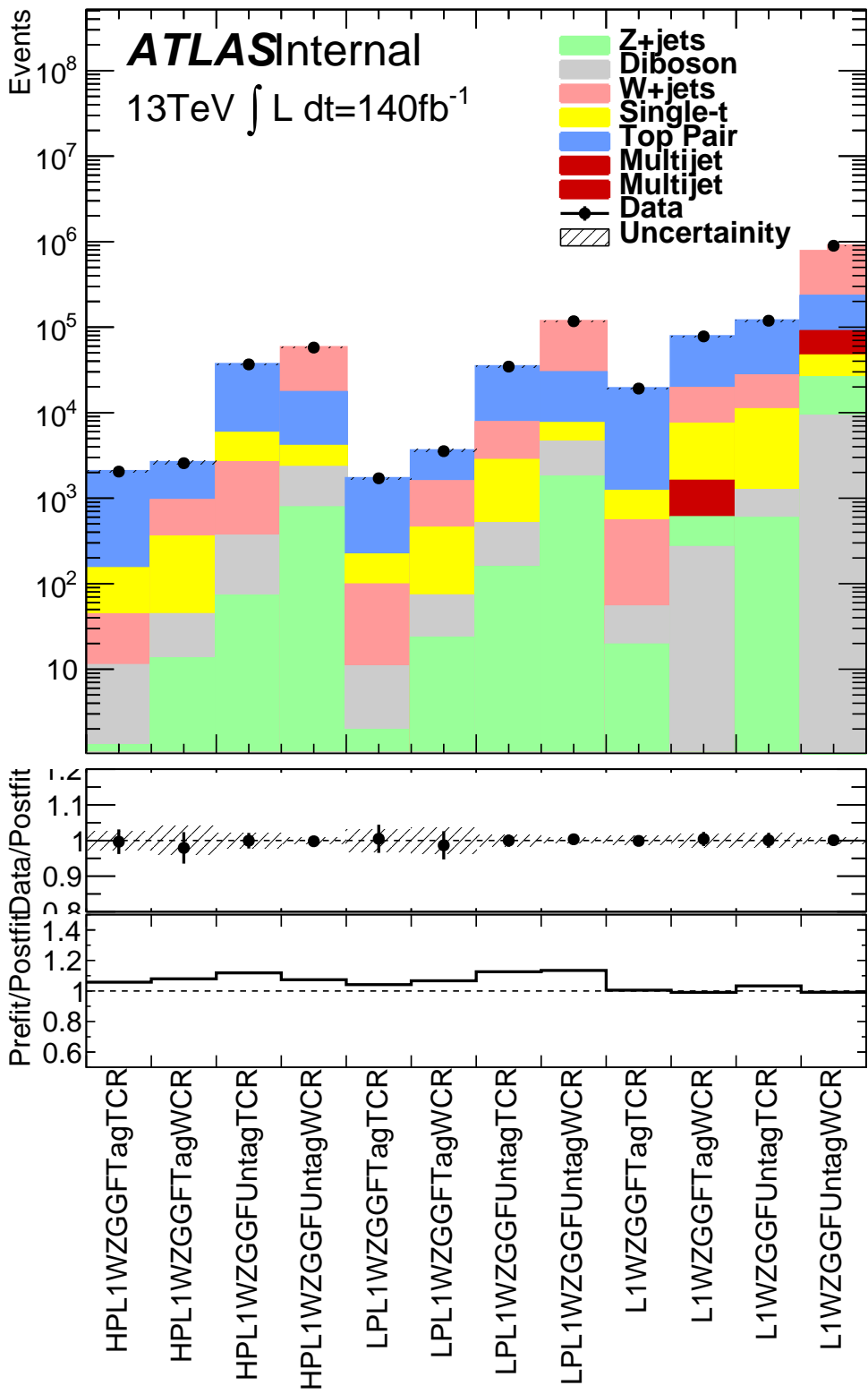


Figure 12.10: This figure shows the distribution of $m_{\ell\nu qq}$ in the DY WZ control regions.

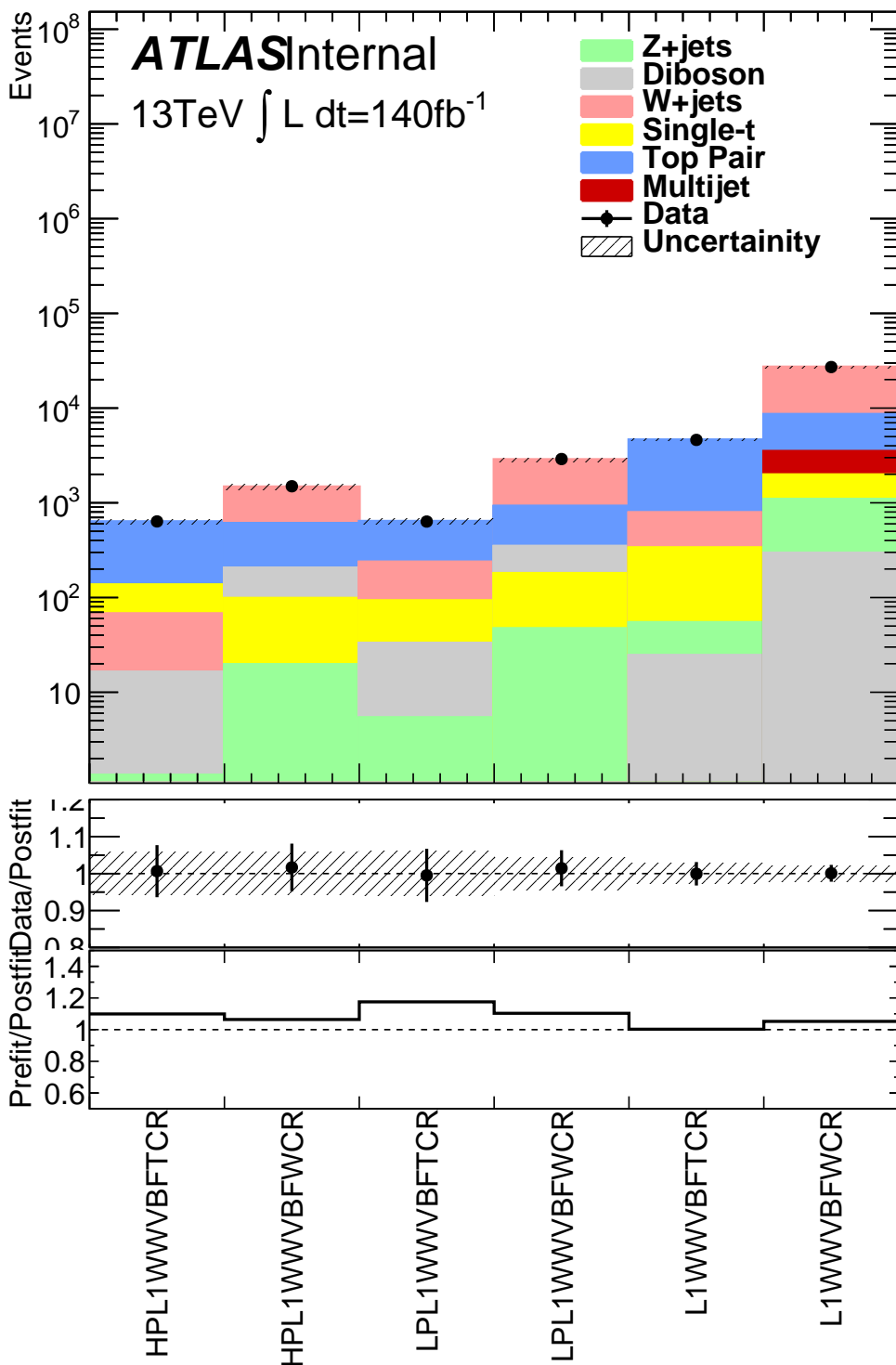


Figure 12.11: This figure shows the distribution of $m_{\ell\nu qq}$ in the VBF WW control regions.

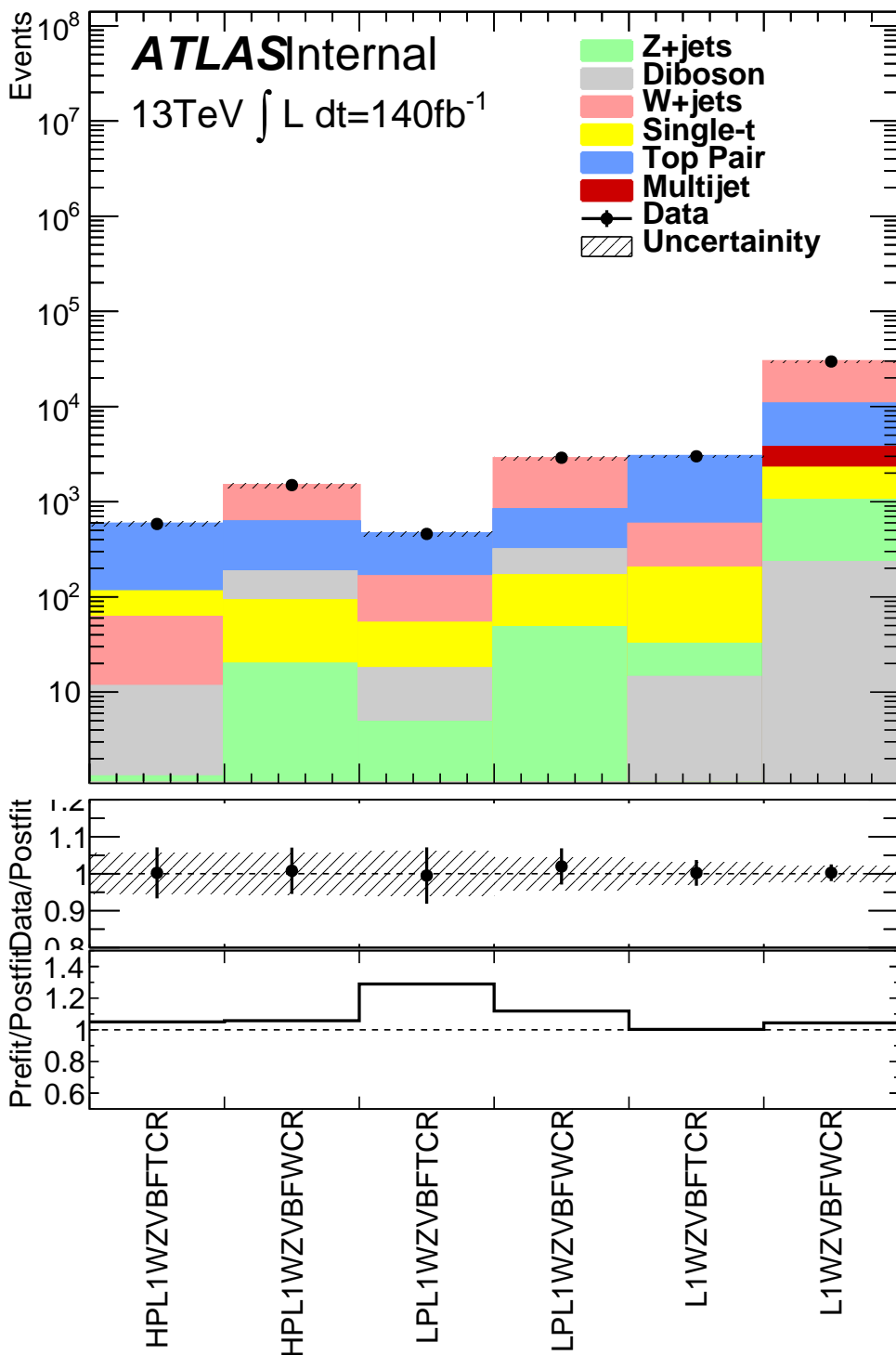


Figure 12.12: This figure shows the distribution of $m_{\ell\nu qq}$ in the VBF WZ control regions.

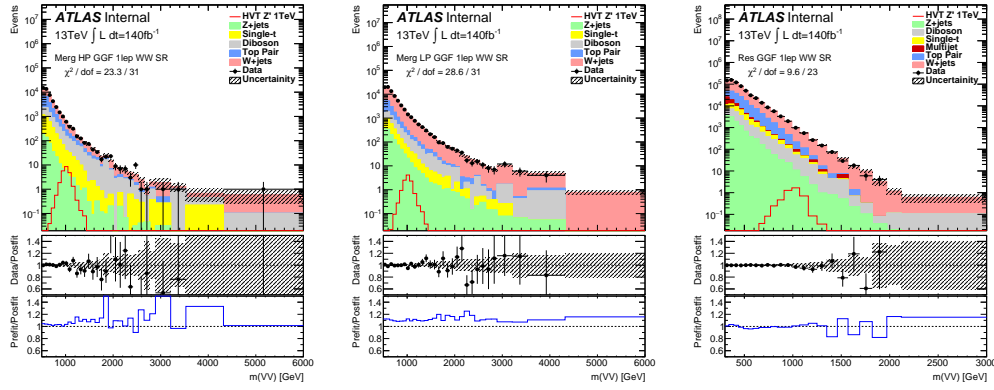


Figure 12.13: This figure shows the distribution of $m_{\ell\nu qq}$ in the GGF WW signal regions.

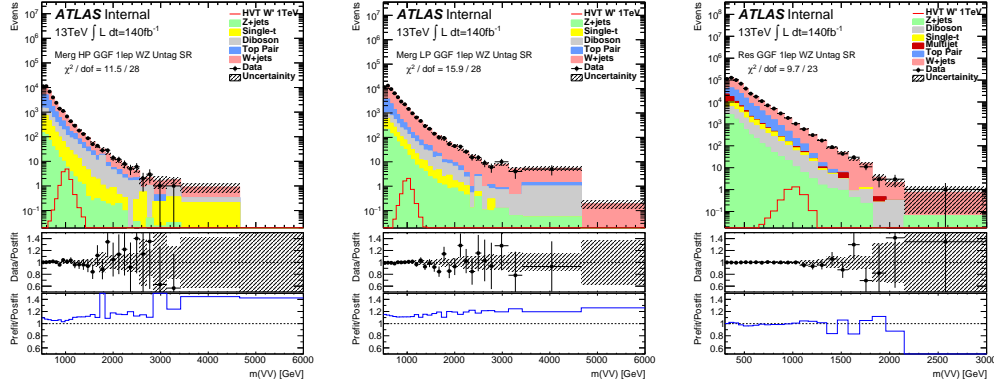


Figure 12.14: This figure shows the distribution of $m_{\ell\nu qq}$ in the GGF WZ Untag signal regions.

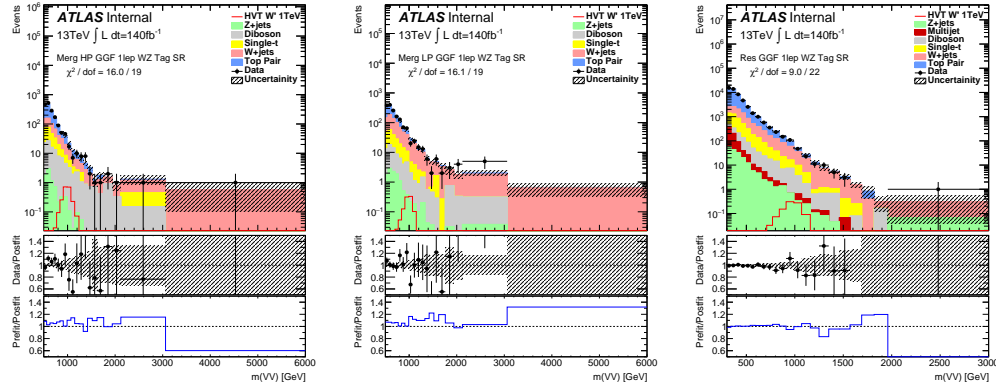


Figure 12.15: This figure shows the distribution of $m_{\ell\nu qq}$ in the GGF WZ Tag signal regions.

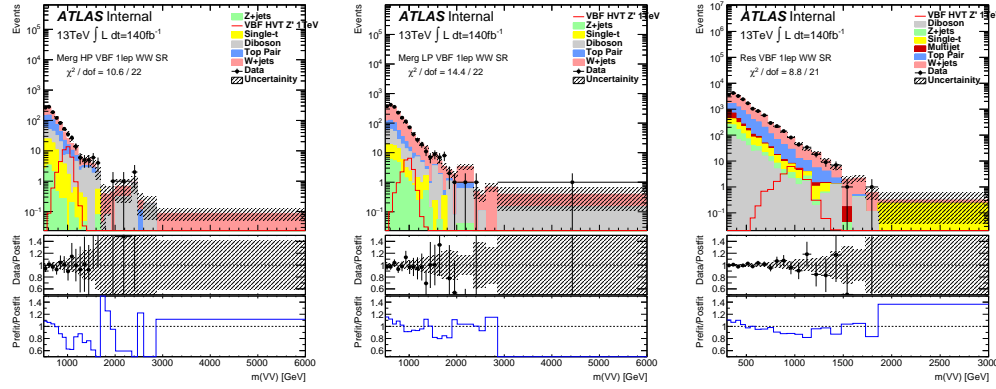


Figure 12.16: This figure shows the distribution of $m_{\ell\nu qq}$ in the VBF WZ Tag signal regions.

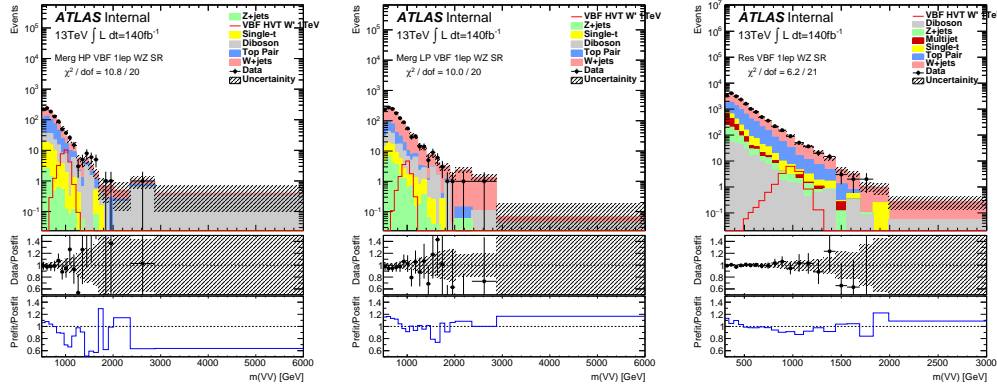


Figure 12.17: This figure shows the distribution of $m_{\ell\nu qq}$ in the VBF WZ Tag signal regions.

12.4 Limits

Using the exclusion limits tests discussed previously, exclusion limits are set on μ and consequently cross-sections for different signal models. Exclusion limits for the models considered are shown in Figure 12.18 - 12.20. These limits exclude HVT Model A $W' < 3.4$ TeV and $Z' < 3.3$ TeV and Model B $W' < 3.7$ TeV and $Z' < 3.7$ TeV. Randall Sundrum Gravitons are excluded for masses below 1.6 TeV .

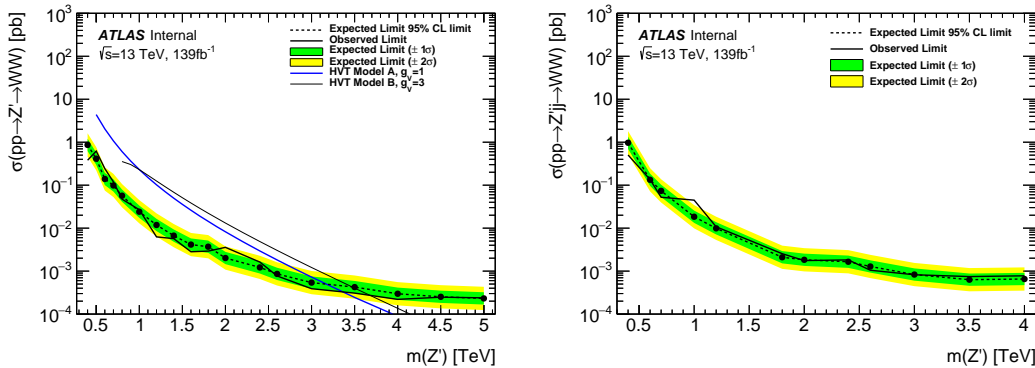


Figure 12.18: This figure shows theory, expected and observed limits for HVT W' DY (left) and VBF (right) production.

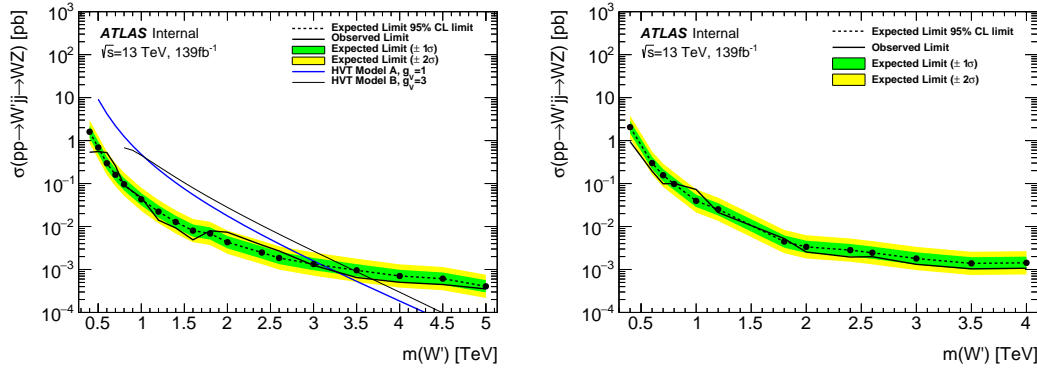


Figure 12.19: This figure shows theory, expected and observed limits for HVT Z' DY (left) and VBF (right) production.

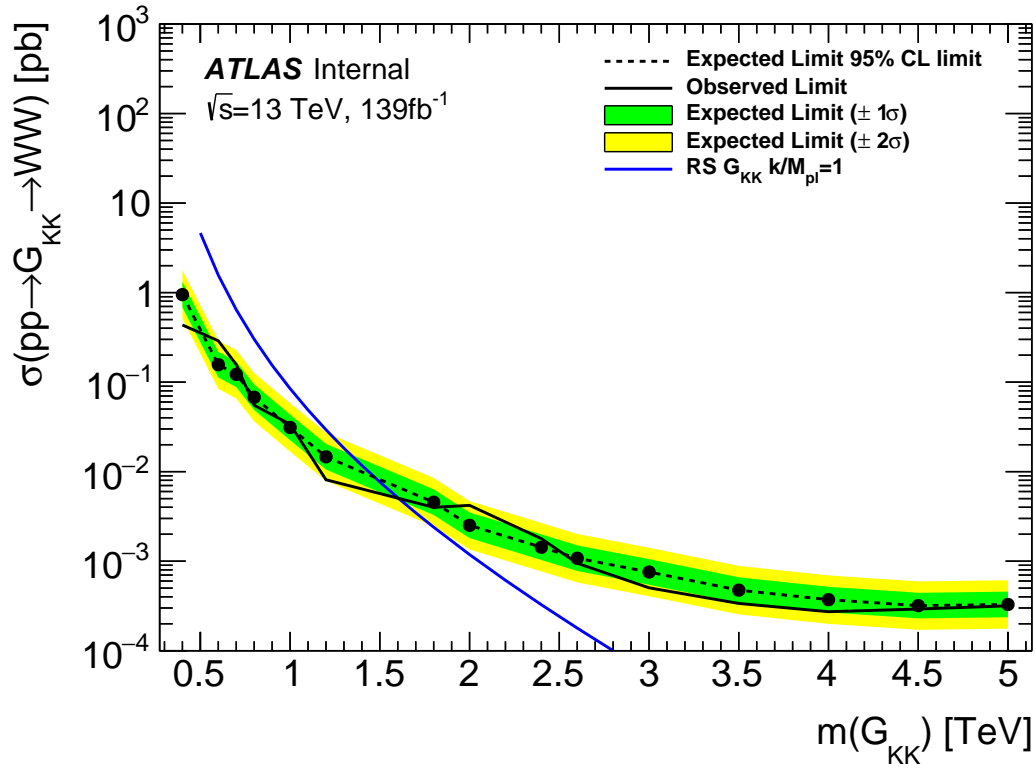


Figure 12.20: This figure shows theory, expected and observed limits for RS Gravitons via DY production.

Part VI

1286

Quark and Gluon Tagging

1287

₁₂₈₈ **Chapter 13**

₁₂₈₉ **Prospects**

₁₂₉₀ For the resolved analysis, signal jets are quark enriched and background jets are
₁₂₉₁ gluon dominated. By classifying jets in the event as quark or gluon initiated, less
₁₂₉₂ background would contaminate the signal region. Figure 13.1 shows the PDGID
₁₂₉₃ for the truth parton matched to the jet (meaning the highest energy parton in
₁₂₉₄ the jet catchment area) in events passing the resolved signal region selections.
₁₂₉₅ PDGID = -1 corresponds to pileup jets, $0 < \text{PDGID} < 6$ correspond to quarks
₁₂₉₆ and $\text{PDGID} = 21$ corresponds to gluons. From this Figure, it is evident that a
₁₂₉₇ notable fraction of the background that contaminates the signal region contains
₁₂₉₈ gluon jets, especially for the sub-leading jet.

₁₂₉₉ As gluons jets have more constituents and therefore more tracks (n_{trk}), the
₁₃₀₀ background jets have more tracks than the signal jets. This is shown in Fig-
₁₃₀₁ ure 13.2. Therefore, by cutting on the number of tracks in a jet, quark and gluon
₁₃₀₂ jets may be distinguished (i.e. jets with less than a given number of tracks are
₁₃₀₃ classified as a quark, otherwise the jet is classified as a gluon.) Moreover, as the
₁₃₀₄ momentum of the jet increases the number of tracks also increases logarithmically
₁₃₀₅ [Cite nachman thesis Natasha]. Therefore by applying a cut on the number of
₁₃₀₆ tracks that scales with the $\ln(p_T)$ is more powerful than a threshold cut on the

1307 number of tracks. Figure 13.3-Figure 13.6 show normalized heat maps of $\ln(p_T)$
1308 vs the number of reconstructed tracks for the background and a 300 GeV Z' signal.
1309 In these plots it is evident that the number of tracks in the background jets grows
1310 more quickly with $\ln(p_T)$ than for the signal jets. This is expected given that the
1311 signal is quark dominated and the background is gluon dominated.

1312 In Figure 13.8 is the ROC Curve for quark gluon tagging with cut on the
1313 number of tracks in a jet that depends on $\ln(p_T)$. The sum of the backgrounds in
1314 the signal region were used for this curve. Here the quark tagging efficiency is the
1315 ratio of quarks tagged as quarks to the total number of quarks in the signal region.
1316 The gluon rejection is calculated as the reciprocal of the gluon tagging efficiency.
1317 Choosing a 90% efficient working point with a rejection of 1.4 corresponds to a
1318 slope of 4 and intercept of -5. Tagging both jets in this analysis would yield an
1319 efficiency of $90\%^{n_{jets}}$. Focusing on the background in Figure 13.9, this cut helps
1320 minimize gluon contamination in the signal region. Also, from these heat maps it
1321 is obvious that the number of tracks in gluon jets grows more quickly than those
1322 in quark jets.

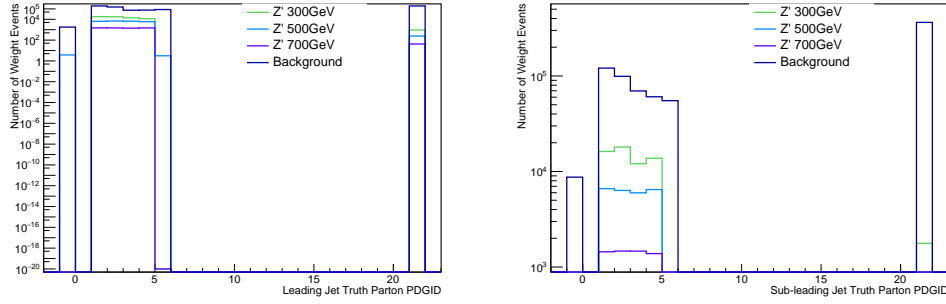


Figure 13.1: PDGID of the truth-level parton matched to the small-R jets passing the Resolved GGF WW Signal Region selections for the (a) Leading (b) Sub-Leading jets . These distributions are shown for 300, 500, and 700GeV Z' signals and the background.

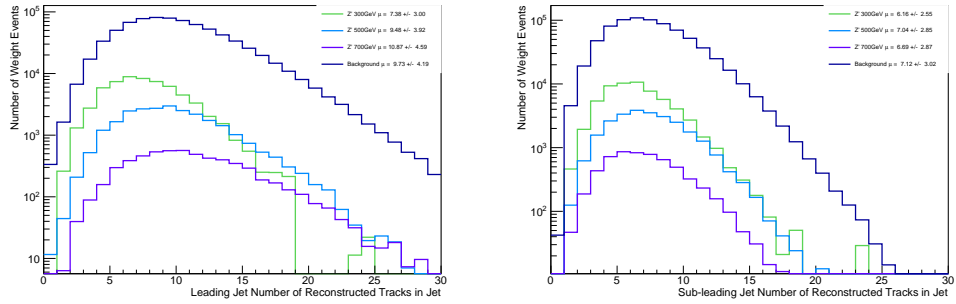


Figure 13.2: The number of tracks in small-R jets in events passing the Resolved GGF WW Signal Region selections for the (a) Leading (b) Sub-Leading jets. These distributions are shown for 300, 500, and 700GeV Z' signals and the background.

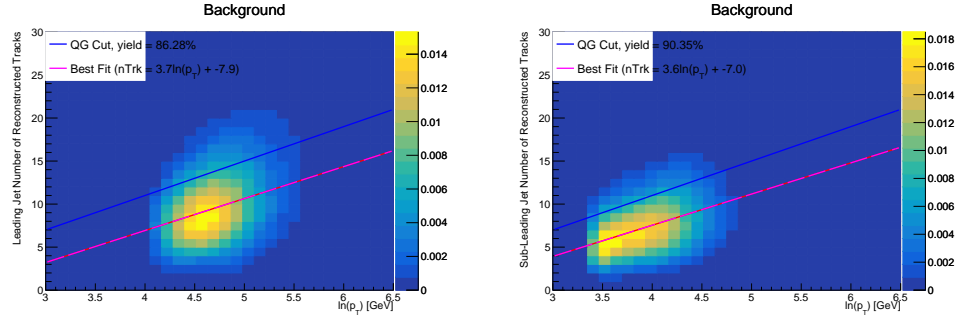


Figure 13.3: The number of tracks in background small-R jets in events passing the Resolved GGF WW Signal region selection vs. $\ln(p_T)$ for (a)Leading (b) Sub-Leading jets. The best fit line for the distribution is also shown, as well as the percentage of jets that pass a cut of number of tracks $< 4 \times \ln(p_T) - 5$. Note the number of total entries in these plots has been normalized to one.

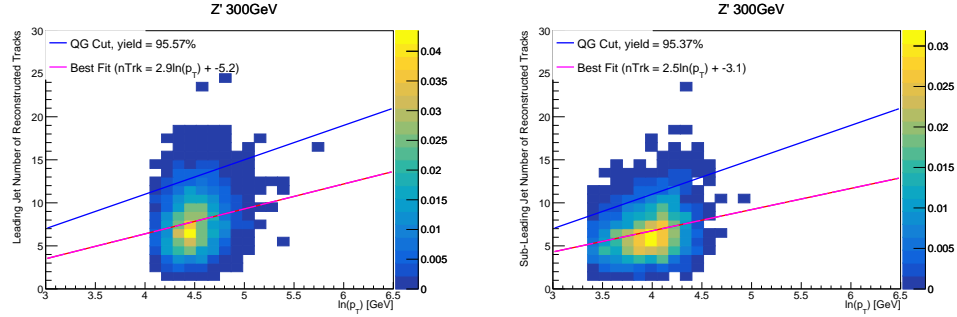


Figure 13.4: The number of tracks in small-R jets in 300GeV Z' events passing the Resolved GGF WW Signal region selection vs. $\ln(p_T)$ for (a)Leading (b) Sub-Leading jets. The best fit line for the distribution is also shown, as well as the percentage of jets that pass a cut of number of tracks $< 4 \times \ln(p_T) - 5$. Note the number of total entries in these plots has been normalized to one.

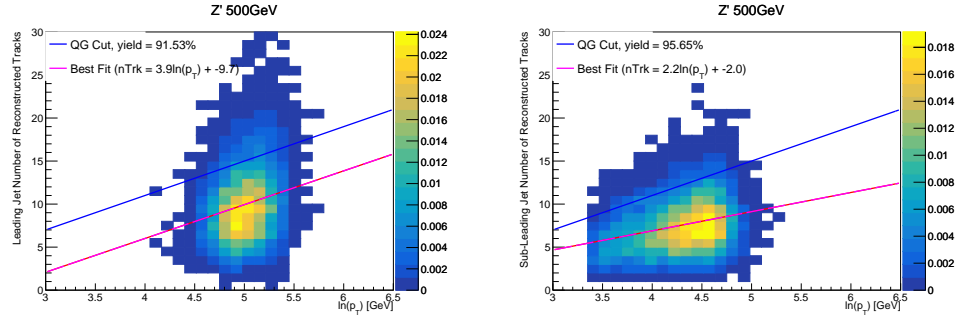


Figure 13.5: The number of tracks in small-R jets in 500GeV Z' events passing the Resolved GGF WW Signal region selection vs. $\ln(p_T)$ for (a)Leading (b) Sub-Leading jets. The best fit line for the distribution is also shown, as well as the percentage of jets that pass a cut of number of tracks $< 4 \times \ln(p_T) - 5$. Note the number of total entries in these plots has been normalized to one.

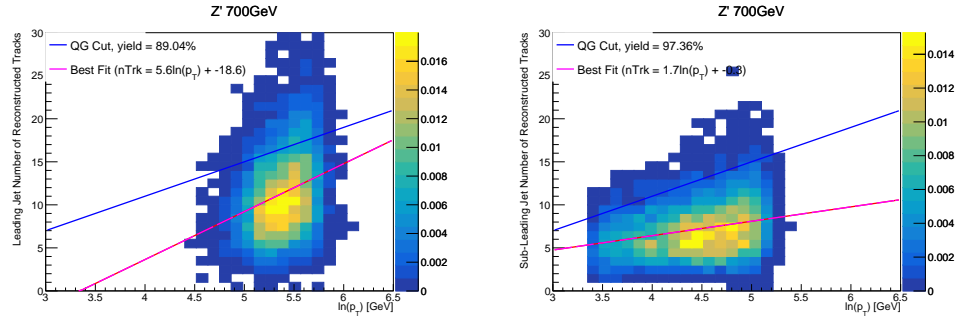


Figure 13.6: The number of tracks in small-R jets in 700GeV Z' events passing the Resolved GGF WW Signal region selection vs. $\ln(p_T)$ for (a)Leading (b) Sub-Leading jets. The best fit line for the distribution is also shown, as well as the percentage of jets that pass a cut of number of tracks $< 4 \times \ln(p_T) - 5$. Note the number of total entries in these plots has been normalized to one.

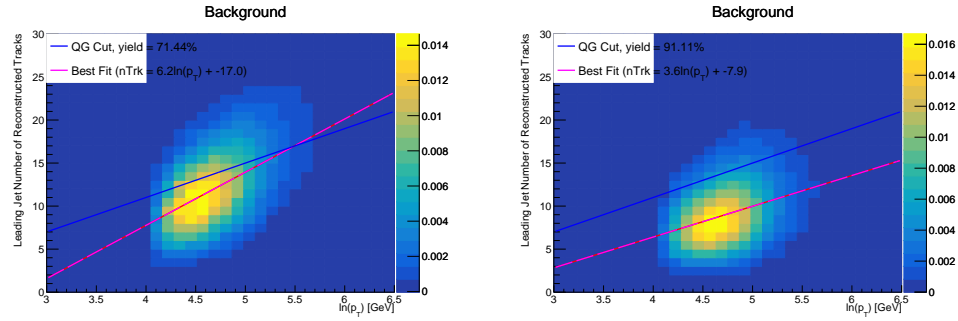


Figure 13.7: The number of tracks in leading small-R jets in background events passing the Resolved GGF WW Signal region selection vs. $\ln(p_T)$ for (a)Gluons (b) Quarks jets. The best fit line for the distribution is also shown, as well as the percentage of jets that pass a cut of number of tracks $< 4 \times \ln(p_T) - 5$.Note the number of total entries in these plots has been normalized to one.

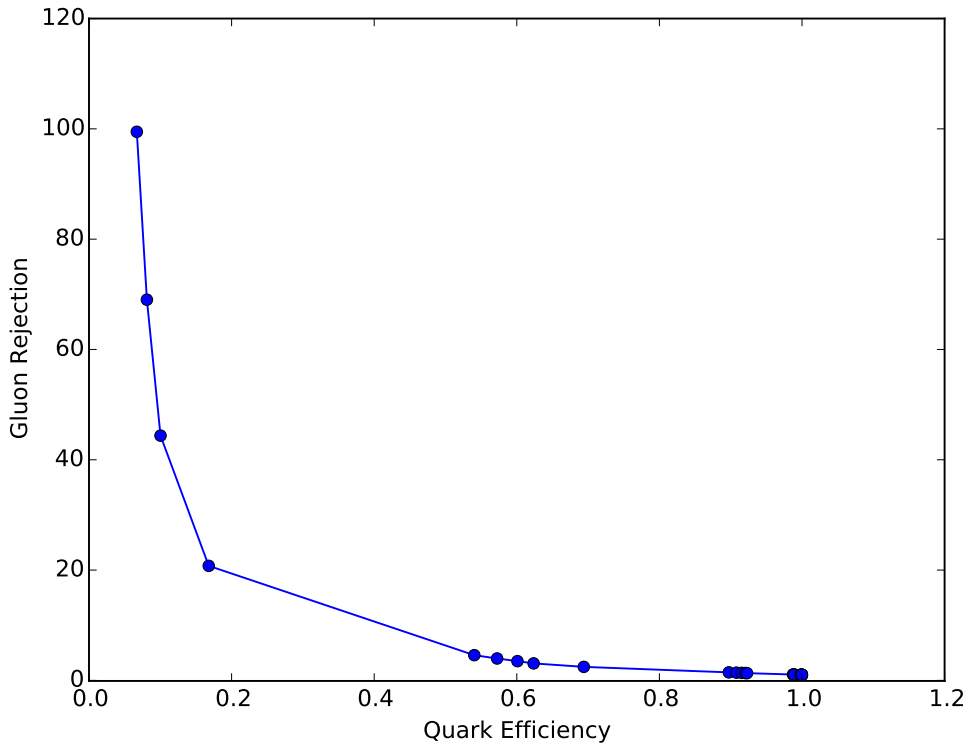


Figure 13.8: ROC Curve for Quark and Gluon Tagging with a cut on the number of tracks that depends on the $\ln(p_T)$.

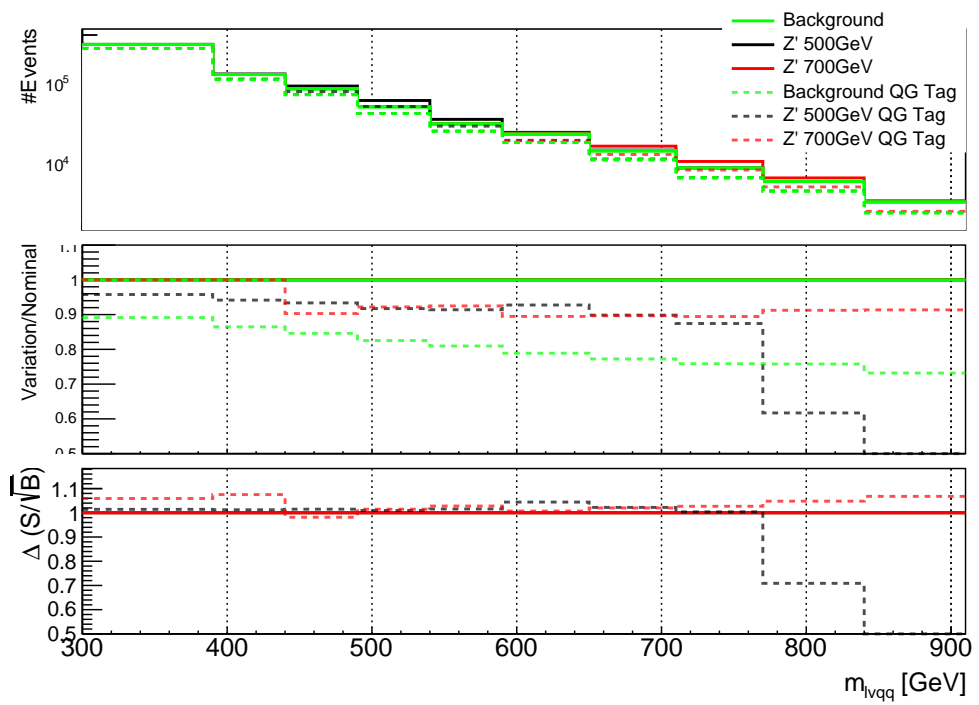


Figure 13.9: The top panel shows the distribution of m_{lvqq} with and without quark gluon tagging. The middle panel shows the ratio of the signals and backgrounds with and without quark gluon tagging. The bottom panel shows the change in S/\sqrt{B} with quark gluon tagging.

₁₃₂₃ **Chapter 14**

₁₃₂₄ **n_{trk} Calibration**

₁₃₂₅ As tagger based on nTrk cuts on the number of tracks in jets, a quantity that
₁₃₂₆ is not known with infinite precision, means that relevant systematic uncertainties
₁₃₂₇ must be evaluated. The sources of uncertainty in n_{trk} may be split into modeling
₁₃₂₈ and experimental uncertainties.

₁₃₂₉ Modeling uncertainties are obtained by assessing PDF and ME uncertainties
₁₃₃₀ on the number of charged particles in particle-level jets in dijet events. The
₁₃₃₁ number of charged particles as a function of jet p_T is calculated using an Iterative
₁₃₃₂ Bayesian (IB) technique [cite paper].

₁₃₃₃ This measurement ([8]) uses the ATLAS 2012 pp collision dataset, correspond-
₁₃₃₄ ing to $20.3/\text{fb}$ at center-of-mass energy $\sqrt{s} = 8\text{TeV}$. The number of charged con-
₁₃₃₅ stituents depends on fragmentation modeling and matrix elements, which do not
₁₃₃₆ depend on s . For this reason, it is safe to use these uncertainties for $\text{sqrt}(s)=13\text{TeV}$.
₁₃₃₇ Monte Carlo (MC) samples are used to determine the response matrix. The MC
₁₃₃₈ sample is a dijet sample generated with Pythia 8.175 using CT10 PDF and AU2
₁₃₃₉ tune. The anti- k_T algorithm is used to cluster jets with a radius parameter R
₁₃₄₀ $= 0.4$. Jets are required to have $|\eta| < 2.1$. Tracks in jets are required to have
₁₃₄₁ $p_T > 500\text{MeV}$, $|\eta| < 2.5$, track-fit $\chi^2 < 3.0$ and originate from the primary ver-

tex. Matching tracks to jets is accomplished using ghost-association [cite]. In this technique, jets are re-clustered with the track collection augmented with "ghost" versions of tracks. These "ghosts" tracks have the same direction as their parent track, but infinitesimal track p_T . This insures meta-jet properties (e.g. η , p_T , etc) are unchanged. A track is matched to a jet if it's ghost version remains in the jet after re-clustering. Further details of the data, object, and event selection may be found in [cite 35].

To select dijet topologies events are required to have at least two jets with $p_T > 50GeV$ that are relatively well-balanced ($p_T^{lead}/p_T^{sub-lead} < 1.5$).

In the IB technique, the prior distribution and number of iterations are the inputs [cite Bayesian paper]. The IB response matrix connects number of charged particles to the number of tracks in jets determined using the simulated samples. This response matrix is used to unfold data to extract the n_c . Before applying the response matrix a fake factor is applied. This accounts for jets that pass detector level selections, but not particle level selections. Following this, the IB method iteratively applies the response matrix using the nominal Pythia 8.175 sample as a prior. The number of IB iterations is chosen to minimize unfolding bias and statistical fluctuations. For this measurement four iterations was found to be optimal by minimizing the unfolding bias from pseudodata simulated with Herwig++ with a prior from Pythia 8 AU2. Finally, the inefficiency factor is applied to account for events passing particle level selection but not detector level, yielding the unfolded nCharged distribution.

This process is prone to three main sources of bias: response matrix, correction factor, and unfolding procedure uncertainties. The response matrix is sensitive to experimental uncertainties impacting jet track reconstruction and calorimeter jet p_T . Correction factors are also sensitive to experimental uncertainties (e.g. JES)

1368 as such uncertainties modify detector level acceptance. Sensitivity to particle
 1369 level acceptance is calculated by comparing Pythia and Herwig. Finally, the bias
 1370 from the IB prior choice is determined by reweighting the particle-level spectrum,
 1371 so the simulated detector level spectrum more closely matches the uncorrected
 1372 data. Unfolding this modified detector-level simulation and comparing it to the re-
 1373 weighted particle-level spectrum indicates bias from the prior distribution choice.

1374 A summary of all the systematic uncertainties associated with this unfolding
 1375 may be found in [ref paper]. Total uncertainties are < 7% for the number of
 1376 charged particles in jets. The unfolded distribution of the nCharged in jets from
 1377 data are further analyzed to extract the quark and gluon nCharged distributions.
 1378 In dijet events, the jet with a larger η is more energetic and therefore more likely
 1379 to be a quark. This is due to the quarks in protons generally having a larger
 1380 fraction of the total momentum of the proton constituents. The more central jet
 1381 is more likely to be a gluon-initiated jet. This correlation between jet η and flavor
 1382 may then be used to extract nCharged in p_T bins using:

$$\langle n_c^f \rangle = f_q^f \langle n_c^q \rangle + f_g^f \langle n_c^g \rangle \quad (14.1)$$

1383

$$\langle n_c^c \rangle = f_q^c \langle n_c^q \rangle + f_g^c \langle n_c^g \rangle \quad (14.2)$$

1384 In this equation the f and c subscripts denote the more forward and central
 1385 jets, respectively. The q and g subscripts denote quark and gluon. The fraction
 1386 of more forward jets that are say gluons is denoted by f_g^f . The other relevant jet
 1387 fractions are denoted with the same naming scheme. Finally, $\langle n_c \rangle$ is the average
 1388 number of charged particles in a jet in a given p_T bin. To show that Eq. (??) may
 1389 be used to extract quark and gluon n_c distributions the extracted distributions
 1390 are compared to n_c distributions determined using the jet flavor in simulation.
 1391 Figure [add figure natasha] shows that the extracted and true distributions differ

1392 by < 1% over the p_T range probed for this study. Moreover, this implies that n_c
1393 depends only on the flavor of the initiating parton and jet p_T .

1394 These extracted distributions are prone to PDF and ME biases. The bias from
1395 the choice of the CT10 PDF for the Pythia sample is accounted for by comparing
1396 quark/gluon fractions for the nominal CT10 sample with its eigenvector variations.
1397 Comparing the quark/gluon fractions from Pythia 8 and Herwig++ quantify the
1398 uncertainty from the ME calculation. These uncertainties are added in quadra-
1399 ture with the unfolding uncertainty to give the total modelling uncertainty on
1400 the extracted n_c distribution. This is shown in Figure 15.2.

1401 To apply these uncertainties in n_c distributions in data, per-jet event weights
1402 are associated with each uncertainty according to:

$$w_i(n_c) = \frac{P(n_c | n_c > \pm \sigma_{n_c}^i)}{P(n_c | n_c >)} \quad (14.3)$$

1403 In Eq. (??), i denotes the uncertainty considered, P is the Poisson probability,
1404 and $\sigma_{n_c}^i$ represents the average impact of the uncertainty on n_c .

1405 The previous uncertainties described accounted for modeling uncertainty as-
1406 sociated with the number of charged particles in a jet. However, n_c is not a
1407 measurable quantity. Instead the number of tracks in a jet is measured, which is
1408 a proxy for n_c . Therefore the uncertainties associated with the measurement of
1409 nTracks must also be considered ([10]). These uncertainties were calculated using
1410 a Pythia 8 dijet sample with NNPDF 23 and Run 2 data. Track reconstruction
1411 efficiency and fake rates are the dominant sources of nTrack uncertainties.

1412 The track reconstruction efficiency is affected by the uncertainty of the de-
1413 scription of the ID material in simulation and the modeling of charged-particle
1414 interactions with this material. These uncertainties are accounted for by varying
1415 the ID material by 5-25% (dependent on the region of the detector considered).

1416 The difference in the tracking efficiency between the nominal and varied simula-
1417 tion give the uncertainty on the track reconstruction efficiency. Another important
1418 source of track reconstruction inefficiency arises in the core of jets. The high den-
1419 sity of tracks in the jet cores can cause ID clusters to merge. The fraction of lost
1420 tracks due to merging is given by the fraction of tracks that have a charge of two
1421 minimum ionizing particles. This quantity is compared between data and simu-
1422 lation resulting in an uncertainty of 0.4% on tracks with $\Delta R < 0.1$. Combining
1423 these effects gives a total uncertainty as a function of p_T and η that is generally
1424 $< 2\%$ [references figure 44 from [10]).

1425 Fake tracks are the other dominant source of nTrk uncertainty. Fake tracks
1426 are tracks that cannot be associated to a single particle. Often these tracks are a
1427 result of random combinations of hits from charged particles that overlap in space.
1428 In dense environments, such as the core of jets or high-pileup environments, fake
1429 tracks are more likely. Fake tracks are estimated with a 'control region method'
1430 which is briefly summarized here [[9]]. By applying a series of track selections
1431 to enrich the fraction of fake tracks (e.g. $|d_0| > 0.1$, track $\chi^2 > 1.4$, etc) in
1432 simulation, templates for fake track parameters are calculated. These templates
1433 are then fit to data to determine the fraction of fake tracks. On average the fake
1434 rate is found to be 30% (independent of p_T and η).

1435 To assess the impact of these two detector level uncertainties, tracks are ran-
1436 domly dropped according to the rates described above. Reconstruction and fake
1437 uncertainties both lower the number of tracks, hence these uncertainties are one-
1438 sided. By dropping tracks in this way a varied nTrk distribution is calculated for
1439 both uncertainties. The associated per-jet event weights are then calculated in
1440 the same way as the modeling weights as:

$$w_i(n_c) = \frac{P(n_{trk} | < n_{trk} > \pm \sigma_{n_{trk}}^i)}{P(n_{trk} | < n_{trk} >)} \quad (14.4)$$

1441 Adding the modeling and detector level uncertainties in quadrature gives the
 1442 overall nTrack uncertainty. The effects of the individual uncertainties on the nTrk
 1443 distributions can be seen in Fig 15.4. Fig 15.3 shows the m_{lvqq} and nTrk distri-
 1444 butions for the W and Top control regions before likelihood fitting. In these plots
 1445 the nTrk uncertainties improve agreement between data and MC. The remaining
 1446 differences are likely covered by likelihood fitting and improving the analysis itself.

1447 **Chapter 15**

1448 **Application**

1449 Using the 90% WP of the n_{trk} tagger improves S/\sqrt{B} is $\sim 3\%$ as shown in
1450 Figure 13.9. Although, n_{trk} is the single most powerful discriminating variable
1451 for quark and gluon jets, the addition of other jet variables would improve the
1452 classification efficiency. Figure 15.1 shows the possible improvement of 10%
1453 in jet classification using the truth label of the jets to classify jets. This type of
1454 improvement is possible by using variables such as jet width, and energy correlata-
1455 tors. Figure [add BDT figure/use 1612.01551.pdf] shows for a 90% quark tagging
1456 efficiency for a 100 GeV jet, a BDT improve the gluon rejection by 0.4. Once this
1457 tagger is calibrated it would improve the analysis sensitivity of this channel.

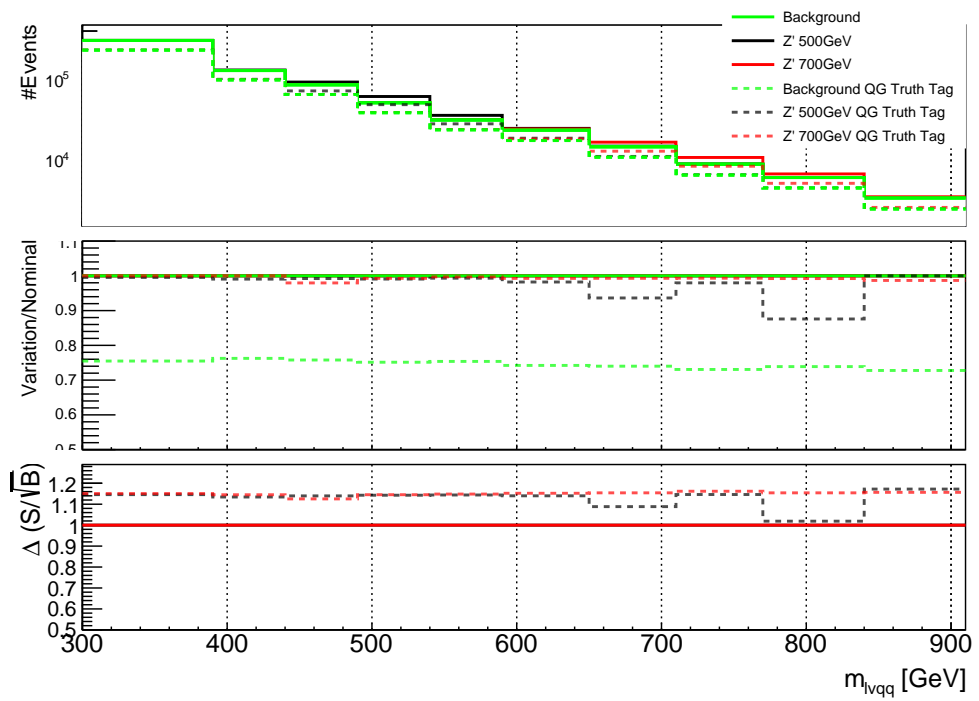


Figure 15.1: The top panel shows the distribution of m_{lvqq} with and without requiring jets to be true quarks. The middle panel shows the ratio of the signals and backgrounds with and without requiring jets to be true quarks. The bottom panel shows the change in S/\sqrt{B} when requiring jets to be true quarks..

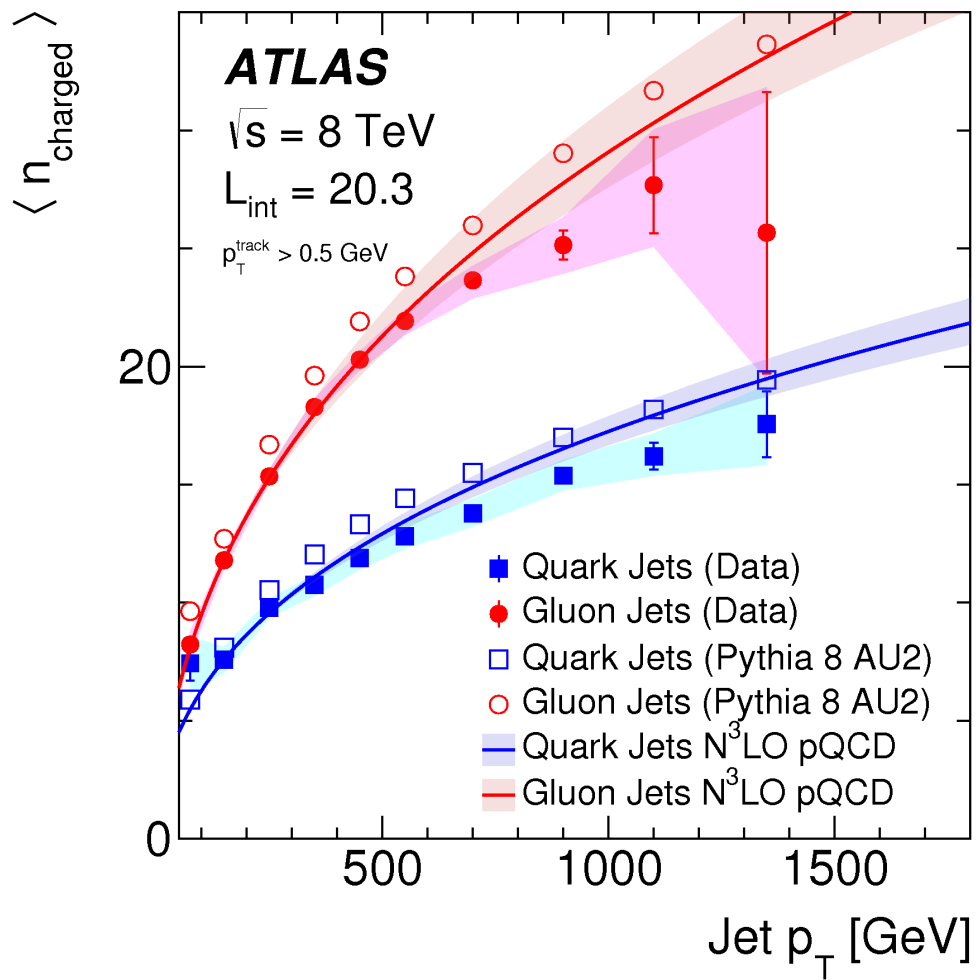


Figure 15.2: Unfolded and extracted n_C qg dstbs..

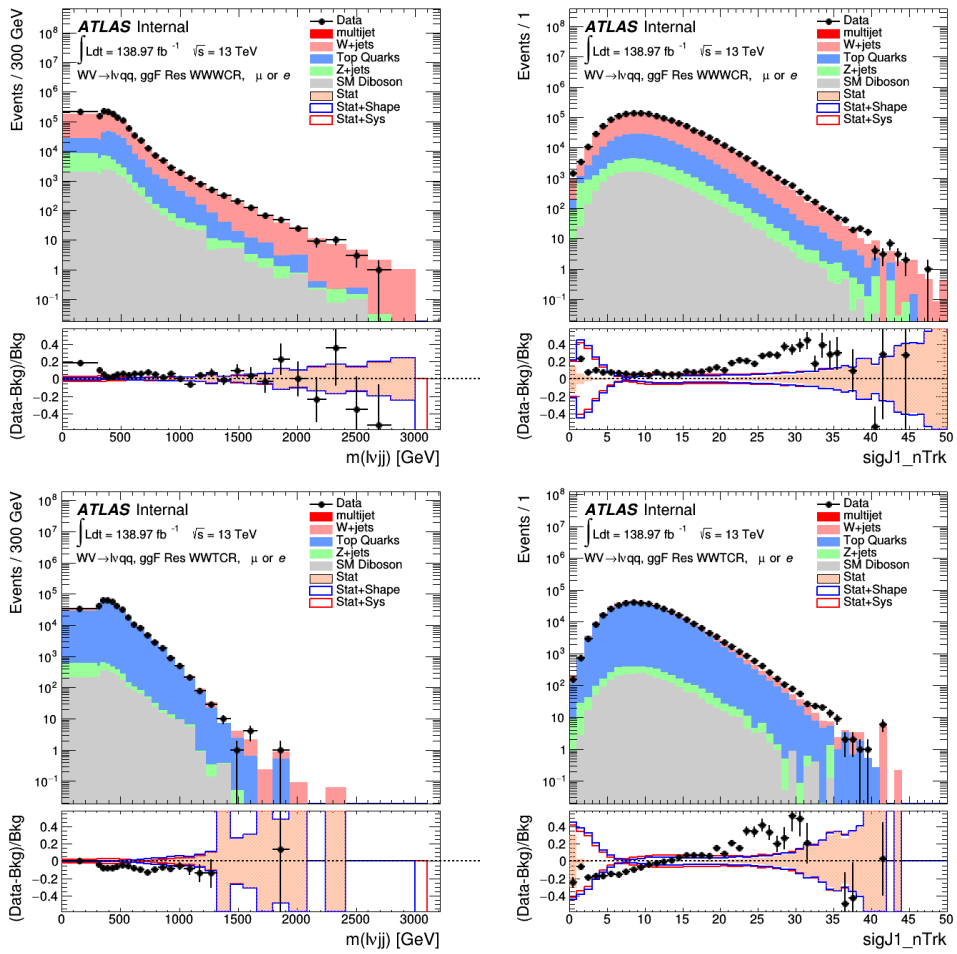


Figure 15.3: PDGID of the truth-level parton matched to the small-R jets passing the Resolved GGF WW Signal Region selections for the (a) Leading (b) Sub-Leading jets . These distributions are shown for 300, 500, and 700GeV Z' signals and the background.

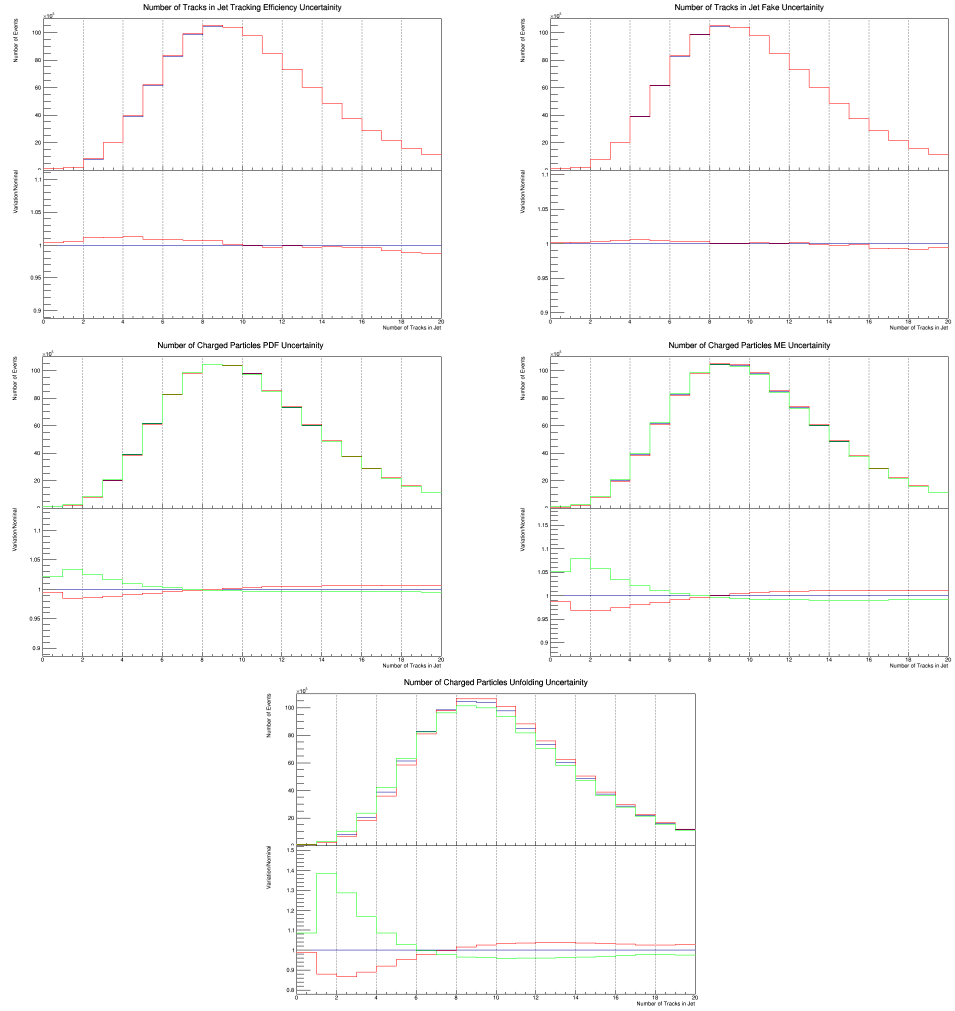


Figure 15.4: These figures show the impact of the uncertainties on the number of tracks in the leading jet in the sum of the background sample in the Resolved GGF WW SR (a) tracking efficiency (b) fake (c) PDF (d) ME (e) unfolding uncertainties.

Part VII

1458

Conclusion

1459

1460 **Chapter 16**

1461 **Conclusions**

1462 A search for WW and WZ diboson resonance production in $\ell\nu qq$ final states
1463 was performed using 139fb^{-1} of pp collision data collected at a center-of-mass
1464 energy of $\sqrt{s} = 13\text{TeV}$ by that ATLAS detector at the LHC between 2015 and
1465 2018. No excess of events above the background-only expectation was observed.
1466 The largest local excess is approximately 2.7σ , which is not significant. Limits
1467 on the production cross section are obtained for the HVT W' and Z' and RS
1468 Gravitons. Signal masses below 3.4 (3.7) TeV are excluded for HVT W' Model
1469 A(B). Signal masses below 3.3 (3.7) TeV are excluded for HVT Z' Model A(B).
1470 Randall Sundrum Gravitons are excluded for masses below 1.6 TeV. Going forward,
1471 improving the classification of jets in events would improve analysis sensitivity.
1472 To distinguish quark from gluon jets a jet tagger based on the number of tracks in
1473 jets is studied in the context of this search. Finally, the calibration of the number
1474 of tracks in jets is discussed.

Bibliography

- [1] Lecture notes particle physics ii.
- [2] Kaustubh Agashe, Hooman Davoudiasl, Gilad Perez, and Amarjit Soni. Warped Gravitons at the LHC and Beyond. *Phys. Rev.*, D76:036006, 2007.
- [3] G. Altarelli and G. Parisi. Asymptotic freedom in parton language. *Nuclear Physics B*, 126(2):298 – 318, 1977.
- [4] ATLAS Collaboration. Atlas muon reconstruction performance in lhc run 2.
- [5] ATLAS Collaboration. Summary plots from the atlas standard model physics group.
- [6] ATLAS Collaboration. Tagging and suppression of pileup jets with the atlas detector.
- [7] ATLAS Collaboration. Jet energy scale measurements and their systematic uncertainties in proton–proton collisions at $\sqrt{s} = 13$ tev with the atlas detector. arXiv: 1703.09665 [hep-ex].
- [8] ATLAS Collaboration. Measurement of the charged-particle multiplicity inside jets from $s=\sqrt{8}$ tev pp collisions with the atlas detector. arXiv:1602.00988 [hep-ex].
- [9] ATLAS Collaboration. Performance of the atlas track reconstruction algorithms in dense environments in lhc run 2. arXiv:1704.07983 [hep-ex].
- [10] ATLAS Collaboration. Properties of jet fragmentation using charged particles measured with the atlas detector in pp collisions at $\sqrt{s} = 13$ tev. arXiv:1906.09254 [hep-ex].
- [11] Alex Dias and V. Pleitez. Grand unification and proton stability near the peccei-quinn scale. *Physical Review D*, 70, 07 2004.
- [12] Stefan Höche, Frank Krauss, Marek Schönherr, and Frank Siegert. Qcd matrix elements + parton showers. the nlo case. *Journal of High Energy Physics*, 2013(4), Apr 2013.

- 1502 [13] Diederik P. Kingma and Jimmy Ba. Adam: A method for stochastic opti-
1503 mization, 2014.
- 1504 [14] David Krohn, Jesse Thaler, and Lian-Tao Wang. Jets with variable r . *Journal*
1505 *of High Energy Physics*, 2009(06):059–059, Jun 2009.
- 1506 [15] Gregory Soyez Matteo Cacciari, Gavin P. Salam. The anti- k_T jet clustering
1507 algorithm. arXiv:0802.1189 [hep-ph].
- 1508 [16] Duccio Pappadopulo, Andrea Thamm, Riccardo Torre, and Andrea Wulzer.
1509 Heavy vector triplets: bridging theory and data. *Journal of High Energy*
1510 *Physics*, 2014(9), Sep 2014.
- 1511 [17] Antonio Pich. The Standard Model of Electroweak Interactions. In *Proceed-
1512 ings, High-energy Physics. Proceedings, 18th European School (ESHEP 2010):
1513 Raseborg, Finland, June 20 - July 3, 2010*, pages 1–50, 2012. [,1(2012)].
- 1514 [18] Lisa Randall and Raman Sundrum. A Large mass hierarchy from a small
1515 extra dimension. *Phys. Rev. Lett.*, 83:3370–3373, 1999.
- 1516 [19] Sebastian Raschka. Model evaluation, model selection, and algorithm selec-
1517 tion in machine learning, 2018.
- 1518 [20] Tania Robens and Tim Stefaniak. Lhc benchmark scenarios for the real higgs
1519 singlet extension of the standard model. *The European Physical Journal C*,
1520 76(5), May 2016.
- 1521 [21] Alex Sherstinsky. Fundamentals of recurrent neural network (RNN) and long
1522 short-term memory (LSTM) network. *CoRR*, abs/1808.03314, 2018.
- 1523 [22] Muhammed Ali Sit and Ibrahim Demir. Decentralized flood forecasting using
1524 deep neural networks. Jun 2019.
- 1525 [23] Wojciech Zaremba, Ilya Sutskever, and Oriol Vinyals. Recurrent neural net-
1526 work regularization, 2014.